Degradation mechanism of AlInGaP light emitting diodes during PMMA encapsulation and operation

Dem Department Physik
der Universität Paderborn
zur Erlangung des akademischen Grades eines
Doktors der Naturwissenschaften
genehmigte

Dissertation

von

Stephan Preuß

Paderborn, November 2007

Contents

List of Figures

List of abbreviations

AL	Active Layer
AS	Absorbing Substrate
CF	Confinement Layers
CL	Cladding Layer
DBR	Distributed Bragg Reflector
DH	Double Heterostructure
EL	Electroluminescence
EP	Edged Plane
FEM	Finite Element Method
FWHM	Full Width at Half Maximum
LED	Light Emitting Diode
LCL	Lower Confinement Layer
μ-EL	Micro Electro Luminescence
MQW	Multi Quantum Well
PMMA	Polymethylmethacrylate
QW	Quantum Well
SEM	Scanning Electron Microscopy
SIMS	Secondary Ion Mass Spectroscopy
ToF	Time of Flight
TS	Transparent Substrate
UCL	Upper Confinement Layer

List of symbols

A	junction area	(m^2)
A_0	intensity of spectra model function	
A_n	numerical aperture	
α	half aperture angle	
α, β	Varshni parameters	
α, β	capture rates	
C_x	diffusion material concentration	(cm^2)
c_v	specific heat capacity	(J/gK)
D	diffusion coefficient	(cm^2s^{-1})
d	diameter	(m)
E	Energy	(eV)
e	elementary charge	(C)
$E_g(T)$	energy gap	(eV)
$E_{g\,0}$	Energy gap at 0 K	(eV)
ε_0	vacuum dielectric permittivity	$(AsV^{-1}m^{-1})$
ε_r	relative dielectric permittivity	
Φ	luminous flux	(lm)
h	Plancks constant	(Js)
η_t	electroluminescence efficiency	
η_B	internal quantum efficiency	
η_{inj}	current injection efficiency	
η_{oc}	outcoupling efficiency	
I	current	(A)
I_{degra}	degradation current	(A)
I_{meas}	measurement current	(A)
I_s	saturation current	(A)
I_e	electron diffusion current	(A)
I_h	hole diffusion current	(A)
φ	polarization angle	(°)

k	Boltzmann constant	(JK^{-1})
L_x	diffusion length	(m)
L	light output	
L_{QW}	width of the quantum well	(nm)
λ	wavelength	(nm)
m	magnification	
$N_{n,d}$	density of non radiative traps	(cm^2)
n, p	carrier concentration	(cm^{-3})
n	refraction index	
ν	frequency	(Hz)
P	power	(W)
q	charge	(C)
θ	diffusion time	(s)
R	resistance	(Ω)
R_s	serial resistance	(Ω)
R_{diff}	differential resistance	(Ω)
r	relative efficiency	
σ_{nr}	capture cross section	(m^2)
t	time	(s)
T	temperature	(K)
T_j	junction temperature	(K)
τ_x	carrier lifetime	(s)
V	voltage	(V)
v_{th}	thermal electron velocity	(m/s)
W_n	width of the depletion zone in the n-type region	(m)
W_p	width of the depletion zone in the p-type region	(m)
W_D	width of the depletion zone	(m)
w_D	diffusion distance	(m)

1 Introduction

Fast progress in the development of new semiconductor materials and an enhanced development of established material systems during recent years have led to new high brightness light emitting diodes (LEDs) [1], [2]. Today, millions of those LEDs are manufactured weekly for a manifold applications. Transformation from light sources with rather low light output used as indicators in many applications to devices able to illuminate rooms is under progress. But not only for ambient lighting, LEDs are promising light sources with a wide field of applications, also car manufacturers have discovered these new solid-state light sources [3]. Efficiency improvement of about 50% for monochromatic light, point light sources for new designs and fast switching times are some benefits unachievable with conventional light bulbs.

Both, the increase of internal quantum efficiency as well as the improvement of light out-coupling leads, from a physical point of view, to an increase in efficiency. Improved light extraction from the LED devices is reached by changing the geometry of the semiconductor material in a way that more photons can pass the interface between the semiconductor and the encapsulation material. This means, less photons are totally reflected at the interface and absorbed in the substrate. In [4] the light out-coupling efficiency from a cubic-shaped device is denoted with η_{ext}=25%. By changing the geometry to a truncated cone with a backside metal mirror the out-coupling efficiency increases to η_{ext}=60%. The limited reflectivity of metal mirrors, which is in the range of R=90%, can be enhanced by using distributed Bragg reflectors (DBRs). In addition to their high reflectivity which can exceed R=99.9% [5], DBRs can be epitaxially overgrown by optically active layers like quantum wells. Further enhancement of light out-coupling can be achieved by surface structuring. In [6] the extraction efficiency enhancement of a LED is denoted by a factor of 4.4 using a photonic crystal.

The improvement of internal quantum efficiency is reached by the invention of quantum wells and multi quantum well LEDs [7]. These structures confine both types of carriers in a narrow range, which leads to a large overlap of the carrier wave functions. This increases the probability of recombination and the creation of photons.

To avoid electron diffusion from the n-type to the p-type contact, diffusion blocking layers are inserted. Due to their large band gap they stop electron diffusion after the multi quantum well (MQW) region.
In order to extend the range of the LED applications further, it is useful to incorporate the semiconductor LED chip directly into total reflection optics. Direct encapsulation by an injection molding tool is a useful way to control the optical geometry to produce the required radiation pattern and also to protect the semiconductor against environmental influences.

In collaboration with the Hella automotive lighting manufacturing company, we developed and tested the influence of the injection moulding encapsulation process on AlInGaP LEDs.
We used LEDs manufactured at Lumileds Lighting with an emission wavelength of λ=630nm and a power input of about P=50mW. Directly dispensing the chips onto a web and using a copper frame, we combined four LED chips to form a module of 32mm length, 9mm height and 8mm thickness. The copper frame integrates the electrical connections and acts as a heat sink to conduct the heat out of the semiconductor chip to the environment. Die bonding glues the anode of each LED chip to the frame, and wire bonding with 25µm diameter gold wires connects the cathode to the frame. An Arburg 380 injection moulding machine encapsulates the frame with polymethylmethacrylate (PMMA) instead of standard resin and forms the four parabolic-shaped optics with the semiconductor light sources inside. The PMMA gives much more flexibility than standard optical resin concerning the shapes achievable, as well as accelerates faster processing because of its quick hardening characteristic.
A disadvantage of injection molding encapsulation is the thermal treatment of the LED chips during this encapsulation process. One known reason for degradation in semiconductor materials is temperature-induced diffusion of impurities and lattice defects. For this reason, specific knowledge of the thermal load of semiconductor materials during an injection molding process is required. We developed a method to investigate the thermal load of the LED chips during the encapsulation process. We also show that thermal degradation during encapsulation is negligible and has no effect on the lifetime of the LED. The mechanical treatment during the encapsulation process is also investigated and different chip contact methods are tested with reference to their application possibilities.
Accelerated degradation experiments on PMMA encapsulated LEDs are carried out. Optical and electrical parameters during aging are measured. The results are analyzed by means of a diffusion model and a lifetime prediction for nominal power rating is calculated. The lifetime

of PMMA-encapsulated LEDs is predicted to $t=10^5$h using a 5% reduction in the luminous flux as failure criteria.

In chapter 2 we describe the fundamentals of semiconductor devices. The light generation and extraction from the semiconductor is described in detail. The micro electroluminescence set-up is described in chapter 3. We discuss space resolved measurements of the LED chip in chapter 4. Chapter 5 describes the LED aging under high forward current. Positive as well as negative aging effects are observed and discussed in detail. The injection molding of LED clusters is presented in chapter 6. We also compare the characteristics of the non-encapsulated LEDs to the characteristics of the PMMA-encapsulated LEDs. A diffusion model to describe the decrease of luminous efficiency versus degradation time is presented in chapter 7. We determine from accelerated degradation experiments the lifetime of the LEDs under the recommended maximum forward current. Chapter 8 gives a summary of the results.

2 Fundamentals of semiconductor devices

This chapter discusses the basic physics of semiconductors with the focal point on LEDs used in this thesis. Starting with the band structure in solids the functional principle of pn-junctions and multi quantum well LEDs (MQW LEDs) made of AlInGaP are described in detail. Furthermore, the light generation by radiative recombination and the non-radiative recombination is illustrated, followed by an analysis of the emission spectrum. Subsequently the theoretical spectrum is compared to a real spectrum and a modelling function is introduced. Light-out coupling from the solid to the environment is described and it is shown that only a small amount of generated photons can escape to the environment.

2.1 Semiconductors

Due to the Pauli principle, the energy splitting of quantized atomic energy levels leads to quasi-continuous energy bands in crystalline solids. Essentially all the transport and optical properties of a semiconductor are determined by these energy bands. Energy levels have regions with energy values called “not allowed”. This means that an electron can exist in allowed regions which are separated by forbidden band gaps. At T=0K we have the situation that an allowed band is completely filled with electrons while the next allowed band, separated in energy by a gap E_g, is completely empty. At T>0K the highest occupied band is partially filled. When an allowed band is completely filled with electrons, the electrons in the band cannot conduct any current. Therefore in this case the material has an infinite resistance and is called an insulator. The material in which a band is only half full with electrons has a low resistance and is called a conductor. The band which is normally filled with electrons at T=0K in semiconductors is called the valence band, while the upper unfilled band is called the conduction band. At finite temperatures, the occupation of electrons and holes is described by the Fermi distribution function. As the temperature rises, the Fermi distribution function smears and some electrons are emitted from the valence band into the conduction band.

Now the electrons in the conduction band and holes in the valence band can carry current.

The bandedge properties are of particular interest since they dominate the electrical and optical properties. Generally one distinguishes between direct and indirect semiconductors. In direct materials the minimum of the conduction band is at the same point in the reciprocal space as the maximum of the valence band. A direct bandgap ensures excellent optical properties, momentum conversation needs a "vertical k". Figure 2.1 depicts the bandstructure of indiumphosphide (InP). The arrow depicts the transition from the minimum in the conduction band to the maximum in the valence band.

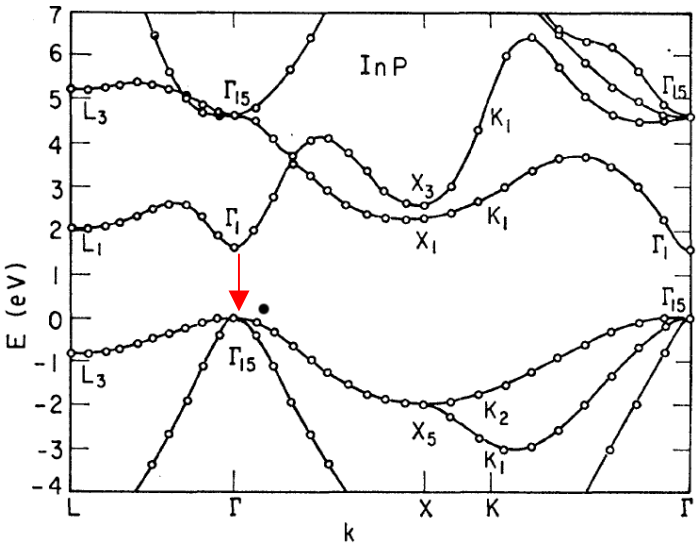

Figure 2.1: Bandstructure of the direct semiconductor InP [8]. The arrow depicts the transition from the conduction band to the valence band.

In a direct semiconductor the maximum of the valence band is below the minimum of the conduction band at the gamma point (Γ). The smallest difference between the conduction band and the valence band is called the energy gap and for InP $E_G^{InP} = (1.4236 \pm 0.0006)eV$ [9].

The most popular indirect semiconductor is silicon (Si). Due to the indirect bandgap Si has very poor optical properties and cannot be used to form LEDs. Also hole transport properties are quite poor as the hole masses are large. However, for electronic devices, silicon is the material of choice, because of its highly reliable processing technology.

An interesting material with respect to optical properties is galliumphosphide (GaP). Material compositions of GaP, indiumphosphide (InP) and aluminiumphosphide (AlP) are commonly used to produce LEDs in the red and amber spectral range. The bandstructure of GaP is shown in Figure 2.2, it can be seen that GaP is an indirect semiconductor material. The

minimum of the conduction band is at the X-Point, the maximum of the valence band at the Γ-Point. The energy gap is $E_{G(X-\Gamma)}^{GaP} = (2.344 \pm 0.006)eV$ [9]. The arrow depicts the transition from the minimum in the conduction band to the maximum in the valence band. To excite an electron from the valence band to the conduction band the energy of E_G is required.

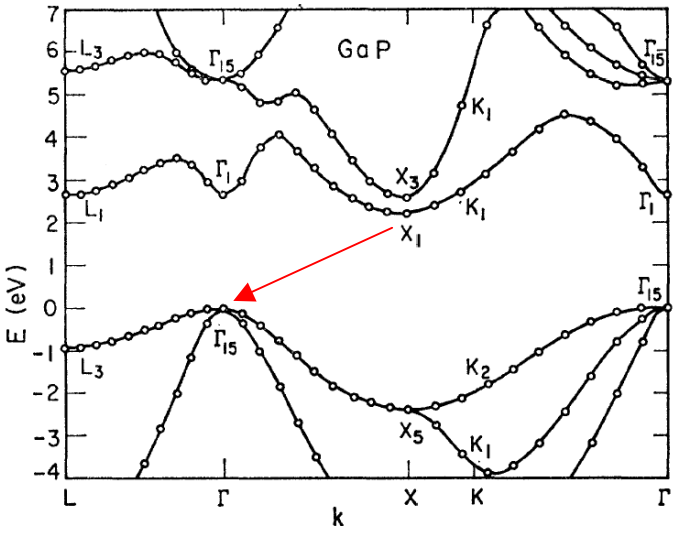

Figure 2.2: Bandstructure of the indirect semiconductor GaP [8]. The arrow depicts the transition from the conduction band to the valence band.

Additionally, the momentum p from a third particle is required due to the non-vertical k. The momentum of a photon is too small, but a phonon can contribute the needed momentum. Therefore a three-particle process is required to excite an electron from Γ_{15} to X_1. The inverse process, a recombination of an electron at X_1 with a hole at Γ_{15}, also needs the momentum of a third particle. These processes are very rare and the internal quantum efficiency would be very low.

The bandstructure of AlP is similar to GaP. AlP like GaP is an indirect semiconductor. The energy Gap is $E_G^{AlP} = (2.51 \pm 0.02)eV$ [9].

The materials GaP, AlP and InP can be alloyed in any composition. Starting from GaP, several Ga-atoms can be replaced by Al-atoms or In-atoms, respectively. The result is the alloy AlInGaP. The properties of this quaternary material system, for example bandgap and lattice constant, are in the limits of the pure materials. Therefore, by varying the composition of the materials, the bandgap and the lattice constant can be tuned. The correlation of the bandgap and the lattice constant is shown in Fig. 2.3. For large InP-content the direct bandgap dominates the alloy. For small InP-content the bandgap of the alloy is indirect. The composition of $(Al_x\ Ga_{1-x})_{0.5}In_{0.5}P$ is lattice-matched to GaAs. Therefore GaAs is a perfect

substrate for AlInGaP LEDs. The red line indicates the spectral range of AlInGaP LEDs lattice-matched on GaAs which covers the purple to green field. This spectral range is equal to a variation in the band gap between 1.89eV and 2.33eV.

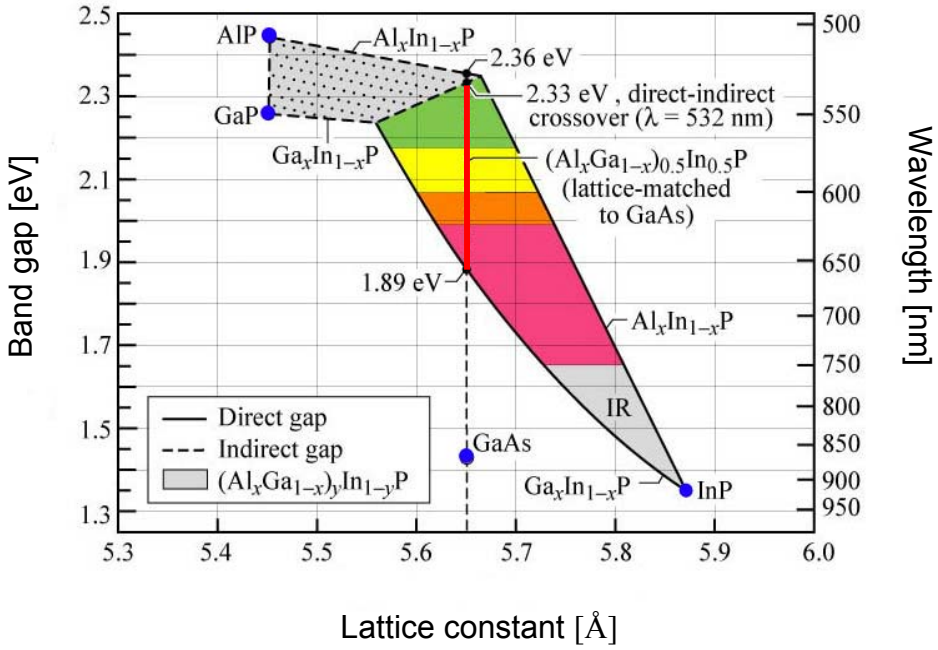

Figure 2.3: Band gap and wavelength of the alloy AlInGaP versus lattice constant. For large In-content the direct bandgap dominates. The red line indicates the spectral range of AlInGaP LEDs lattic- matched on GaAs with a direct bandgap [7].

Because of the small band gap of GaAs, E_g=1.45eV [10], it is non transparent for the emission range of AlInGaP LEDs. This leads to light absorption in the substrate and less efficient devices. These disadvantages could be overcome by removing the substrate after the production process.

2.2 Band structure of p-n junctions

2.2.1. Doping of semiconductors

The density of free carriers that can carry current in pure semiconductors is very low. To increase the free carrier concentration, impurities known as dopants are introduced. The dopants are chosen from the periodic table so that they either have an extra electron in their outer shell in comparison to the host semiconductor, or have one electron less. Absent electrons are called holes and act as a positive quasi-particle.

The resulting dopant is called a donor or acceptor. In chapter 7.4 it is shown that the p-type dopant in the LEDs used during this investigation is magnesium (Mg). The n-type doping is not investigated, but a common material for this application in AlInGaP LEDs is tellurium (Te) [11]. Donors create an energy level in the energy gap near the conduction band edge. Acceptors also create an energy level in the energy gap, but near the valence band edge. In the p-doped area the holes are the majority carriers, the electrons are the minority carriers. In the n-doped area the notation is vice versa.

Non-doped semiconductors are called intrinsic and the Fermi level is in the middle of the band gap. By n-type doping the Fermi level moves towards the conduction band, p-type doping lowers the Fermi-level to the valence band.

Holes and electrons can recombine and photons with the energy difference E_{Ph} are created and radiated. The energy of a photon is given by:

$$E_{Ph} = h\nu = \frac{hc}{n \cdot \lambda} \tag{2.1}$$

with $E_{Ph} \geq E_g$

where h is the Planck's constant, ν is the frequency, λ is the wavelength of the photon, c is the speed of light, and n is the refraction index.

The inverse process is also possible, a photon can be absorbed by the semiconductor and a electron hole pair can be generated. Typical applications are solar cells.

2.2.2. pn-junction

The pn-junction is one of the most important structures in solid state electronics. To fabricate a pn-junction a p-type layer is formed by epitaxial growth. The dopant species is changed and a n-type layer is created directly on the p-type layer. We assume in our analysis that the junction is abrupt. In the absence of any applied bias no current flows and the Fermi level is uniform throughout the structure. The material at both ends of the structure is neutral. In the p-type region, far away from the junction, the density of acceptors exactly balances the density of holes. In the n-type region, far away from the junction, the density of immobile donors exactly balances the free electron density. In the depletion region (W_D) the bands are bent and a field exists which has swept out the mobile carriers leaving behind negatively charged acceptors in the p-region and positively charged donors in the n-region. In the depletion zone, which extends a distance W_p in the p-region and a distance W_n in the n-region, an electric field exists. Any electron or hole is swept away by this field. Thus a drift

current exists which counterbalances the diffusion current which arises because of the difference in electron and hole densities across the junction. Figure 2.4 depicts the band structure of such an unbiased pn-junction. For similar space charge density in the p- and n-regions of the depletion zone we get applying Poisson's law:

$$-\Delta V = \frac{1}{\varepsilon_r \varepsilon_0} \rho \tag{2.2}$$

a quadratical behaviour of the bands, because:

$$E = qV \tag{2.3}$$

where

V is the potential difference, ε_r is the relative permittivity, ε_0 is the electric field constant, q is the charge and ρ is the space carrier density.

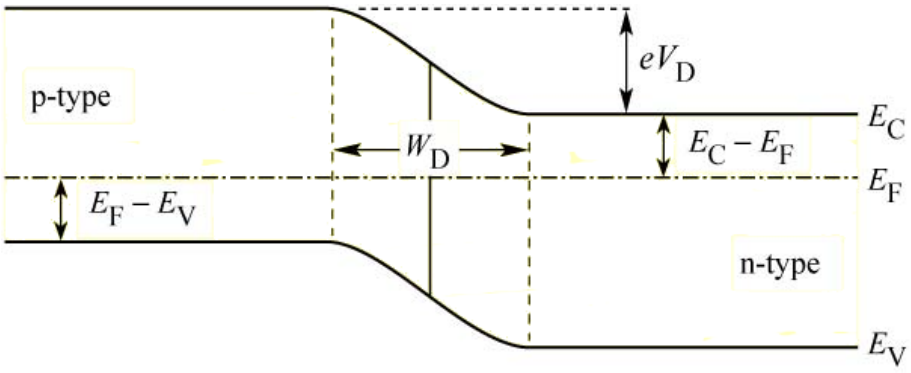

Figure 2.4: Band structure of the p-n junction under zero bias. [7].

In the present of an applied bias the balance between drift and diffusion current will no longer exist and a current flows. One distinguishes between a forward bias and a reversed bias. In forward bias V_f, the p-side is at a positive potential with respect to the n-side. The potential barrier eV_D is reduced by the applied voltage V_f which leads to a reduced electrical field at the junction. Therefore the drift current is also reduced and a diffusion current flows through the device. The current increases exponentially with the applied forward bias. If the applied voltage is equal to the potential barrier eV_D this situation is called "flat band condition" and the applied voltage is called the threshold voltage.

If the bias is applied in the reverse direction, the barrier eV_D increases with increasing V_r and the electric field at the junction increases as well. Thus, in the equilibrium, the increased drift current must be compensated by an increased diffusion current. Therefore the depletion zone

expands in the n- and p-type region. A low reverse current flows through the device which is independent from the applied reverse voltage.

The current flow through a pn-diode has a strongly nonlinear and rectifying behaviour. The current saturates at a value I_0 if a reverse bias is applied. Since the value is quiet small, the diode is essentially non-conducting. If a positive bias is applied the current increases exponentially and the diode becomes strongly conducting. The current density at an abrupt pn-junction is given by [12]:

$$j_{Diff} = j_p + j_n = \left(\frac{eD_p p_{n0}}{L_p} - \frac{eD_n n_{p0}}{L_n} \right) \left[\exp\left(n_{Diff} \frac{e(V - IR_S)}{k_B T} \right) - 1 \right] \tag{2.4}$$

where j_p is the hole current density, j_n is the electron current density, D_p is the diffusion coefficient of the holes, p_{n0} is the hole concentration in thermodynamical equilibrium in the n-region, L_p the diffusion length of the holes, D_n is the diffusion coefficient of the electrons, n_{p0} is the electron concentration in thermodynamical equilibrium in the p-region, L_n the diffusion length of the electrons, and T the temperature. R_s describes the serial resistance of the device and n_{Diff} is the quality factor which theoretically is one.

2.2.3 Double heterostructures and quantum wells

A double heterostructure (DH) consists of the active region in which recombination occurs and two confinement layers cladding the active region. The bandstructure of a double heterostructure LED is shown in Fig. 2.5. The two cladding or confinement layers have a larger bandgap than the active region. If the bandgap difference between the active and the confinement region is ΔE_g, then the band discontinuity occurring in the conduction and valence band follows the relation:

$$E_g^{clad} - E_g^{act} = \Delta E_g = \Delta E_C + \Delta E_V \tag{2.5}$$

Both band discontinuities, ΔE_C and ΔE_V, should be much larger than kT in order to avoid carrier escape from the active region into the confinement regions.

In the case of a homojunction, carriers diffuse to the adjoining side of the junction under forward bias conditions. Minority carriers are distributed over the electron and hole diffusion lengths. In III-V semiconductors, diffusion lengths can be 10µm or even larger. The wide distribution of carriers can be avoided by employing double heterostructures. Carriers are

confined to the active region as long as the barrier heights are much higher than the thermal energy *kT*. Additionally, reabsorption of the generated photon is avoided due to the lower bandgap of the active layer. Nowadays all high efficiency LEDs contain double heterostructure designs.

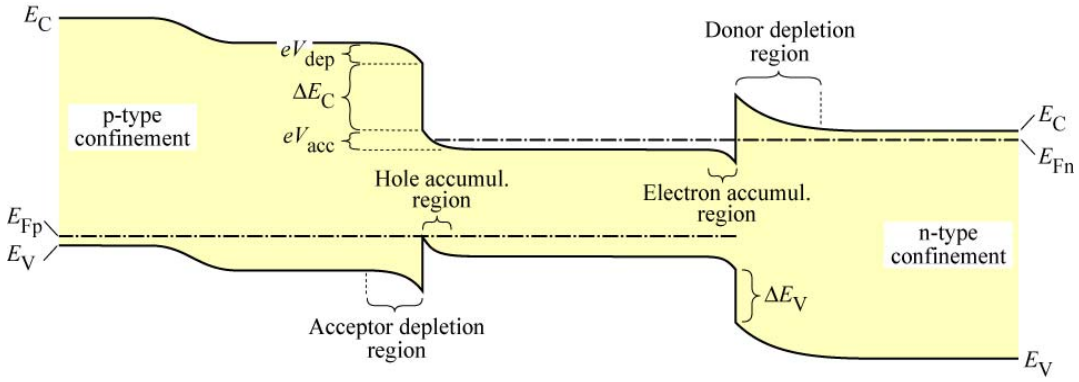

Figure 2.5: Band diagram of a forward-biased double heterostructure. The p-type confinement layer consists of a lightly doped layer close to the active region and a higher doped layer further away from the active layer [7].

When the thickness of the active layer of a DH is reduced to the order of the de Broglie carrier wavelength two dimensional quantization occurs. Quantum well active regions provide additional carrier confinement to the narrow well regions which can further improve the internal quantum efficiency. On the other hand, if a quantum well active region is used, the barriers between the wells will impede the flow of carriers between adjacent wells. Thus the barriers in a multi-quantum well (MQW) region need to be sufficiently transparent (low or thin barriers) in order to allow efficient carrier transport between the wells and to avoid the inhomogeneous distribution of carriers within the active region. In [13] it is described that QW have discrete energy levels which strongly depend on the barrier depth and thickness. Therefore the emission energy of the device can be tuned by changing the geometry of the QW. The wave functions of a captured electron and hole in the QW have a large overlap which leads to a probable recombination.

Figure 2.6 shows the band diagram of a quantum well for the $(Al_xGa_{1-x})_{0.5}In_{0.5}P$ material system, the QW width is denoted by L_{QW}. The energy eigenvalues are designated by E_1 and E_2 for electrons and E_{h1} and E_{h2} for holes.

All LEDs used in these investigations are MQW LEDs. We assume a well thickness and a barrier thickness of about 5nm. In [14] the well width of an AlInGaP LED is 3nm.

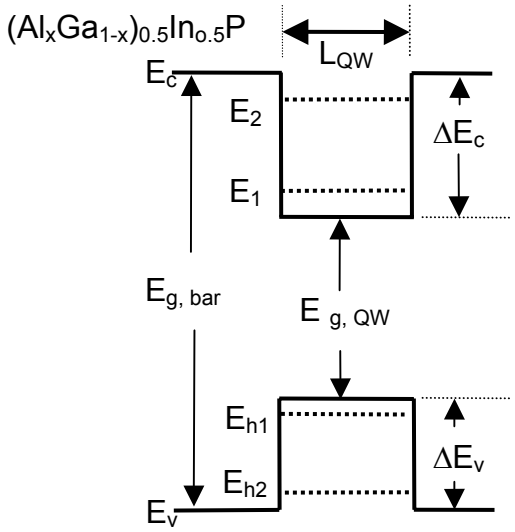

Figure 2.6: Square-well potential of a quantum well structure. The well is formed by decreasing the mole fraction x.

Interband recombination transition (Δn=0) occurs from a bound state in the conduction band e.g. E_1 to a bound sate in the valence band e.g. E_2. The energy of transition is given by:

$$E_t = E_{g,QW} + E_1 + E_{h1} \tag{2.6}$$

Thus the recombination can proceed between two well-defined energy levels in contrast to a bulk semiconductor.

Figure 2.7 depicts the density of states for quantum wells (2D) as well as for bulk material (3D). The step-like density of state is characteristic for a quantum well structure [16]. The half parabola originates from the conduction band edge.

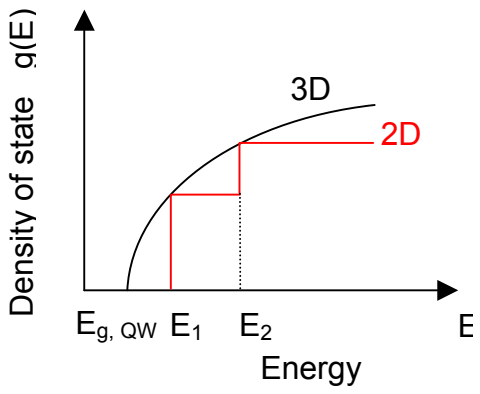

Figure 2.7: Density of state for a quantum well structure (2D) and for bulk material (3D).

2.3 Radiative recombination

Electrons and holes in semiconductors recombine either radiatively, i. e. accompanied by the emission of a photon, or non-radiatively (see chapter 2.6). In LEDs, the former is clearly the preferred process.

Considering a free electron in the conduction band, the probability of an electron recombining with a hole is proportional to the hole concentration. The number of recombination events will also be proportional to the concentration of electrons. Thus the recombination rate is proportional to the product of electron and hole concentrations. Using a proportionality constant, the recombination rate per unit time per unit volume can be written as the well known bimolecular rate equation [7]

$$R = -\frac{dn}{dt} = -\frac{dp}{dt} = Bnp \tag{2.7}$$

where R is the recombination rate, n and p are the electron and hole concentrations and B is the proportional constant.

Further we discuss the recombination dynamics as a function of time. The equilibrium and excess electron and hole concentrations are n_0, p_0, Δn and Δp, respectively. Since electrons and holes are generated and annihilated (by recombination) in pairs, the steady-state electron and hole excess concentrations are equal,

$$\Delta n(t) = \Delta p(t) \tag{2.8}$$

Using the bimolecular rate equation (2.7), the recombination rate is given by:

$$R = B\left[n_0 + \Delta n(t)\right]\left[p_0 + \Delta p(t)\right] \tag{2.9}$$

Quantum wells provide a means of confining the free carriers to a narrow quantum well region by using the two barrier regions cladding the quantum well. The well thickness is L_{QW}, the conduction band and the valence band wells have a carrier concentration of n^{2D}/L_{QW} and p^{2D}/L_{QW}, respectively. Using these values as the 3D carrier concentrations, the recombination rate can be inferred from Eq. (2.9), and is given by:

$$R = B\frac{n^{2D}}{L_{QW}}\frac{p^{2D}}{L_{QW}} \tag{2.10}$$

One of the essential advantages of quantum well LEDs is illustrated by this equation. A decrease of the QW thickness allows to attain high 3D carrier concentrations in the well (carriers per cm^3). The carrier lifetime is then reduced and the radiative efficiency is increased [7]. For small QW thicknesses, the wave function no longer scales with the physical well width. L_{QW} must be replaced by the carrier distribution width, which for sufficiently small well thicknesses is larger than L_{QW}, since the wave function will extend into the barriers.

2.4 Modelling of the emission spectra

The emission spectra of QW LEDs is given by the product of the density of state and the distribution of carriers in the allowed bands. The distribution of carriers is given by the Boltzmann distribution, i.e.

$$f_B(E) = e^{-E/(kT)} \tag{2.11}$$

The density of state in a QW is given by:

$$g(E) \propto \sum_n H(E - E_n) \tag{2.12}$$

where $H(E-E_n)$ is the Heaviside function. It takes the value of zero when E is less than E_n and 1 when E is equal to or greater than E_n.

Figure 2.8 depicts the emission spectrum of a QW LED (red curve). The low energy regime is confined by the 2D density of states. The high energy emission is given by the Boltzmann distribution [15].

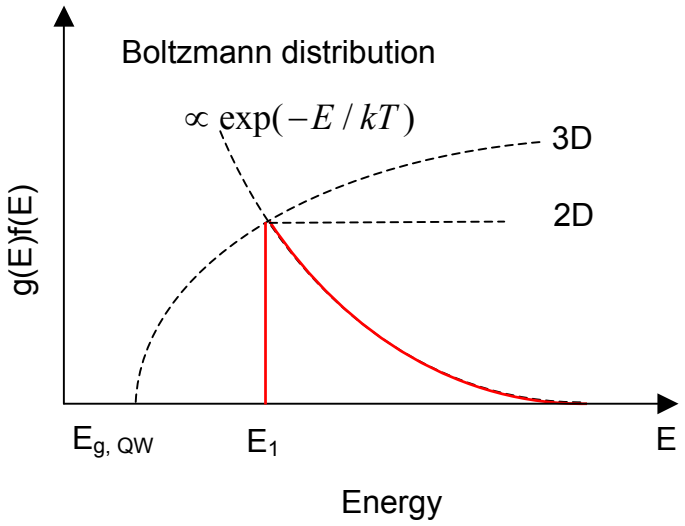

Figure 2.8: The emission spectrum of a QW LED, red curve, is the product of the density of state and the distribution of carriers.

The real emission spectrum of a LED is quite different. Figure 2.9 depicts the emission of a non-encapsulated LED chip with a peak energy of E=1.93eV in logarithmic scale. An exponential slope to the maximum emission is significant. Then the emission decreases exponentially with a different slope. The exponential increase of the measured emission spectra is called Urbach edge. According to [17] the Urbach edge yields an exponential increase of the intensity.

Energy levels in QWs strongly depend on the QW thickness. In the MWQ region of a LED the thickness of the individual QWs may vary due to fluctuations in the production process [18]. Therefore single QWs may emit at a different energy level. Thus the emission broadens. These effects lead to an exponential increase of the emission [19]. Also the exponential decrease of the emission in the high energy regime is effected by QW inhomogeneous broadening. Therefore the carrier temperature could not be calculated directly by Eq. (2.11). Details of temperature measurements are given in chapter 4.4.

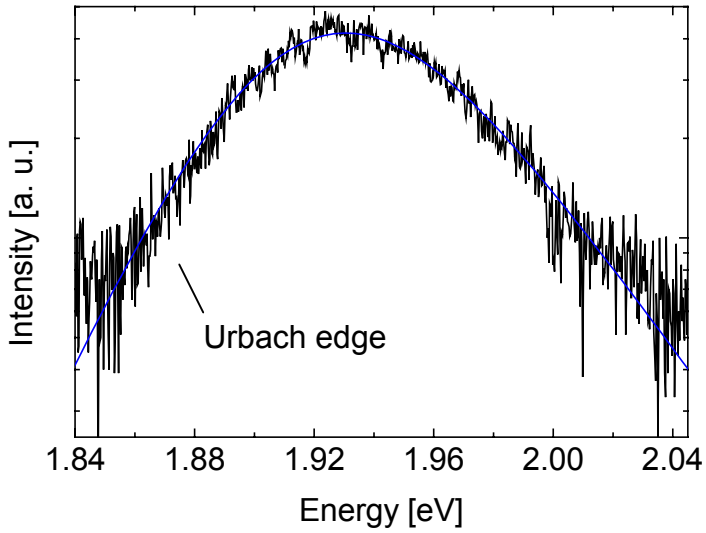

Figure 2.9: Emission spectrum of an AlInGaP LED. The black line indicates the measurement, the blue line the model function.

To analyse the emission with respect to peak energy and exponential decay of the emission a fit function is required. The peak energy and the exponential decay can be calculated by the fit function. The following function describes the emission:

$$g(E) = Ah(E)k^2(E) \tag{2.13}$$

with

$$h(E) = e^{a(E-D)}$$

$$k(E) = \frac{1}{e^{ab(E-d)} + 1}$$

$$d = E_0 - \frac{\ln\left(\frac{1}{2b-1}\right)}{ab}$$

$$A = A_0 \frac{\left(\frac{1}{2b-1}\right)^{\frac{1}{b}}}{\left(\frac{2b}{2b-1}\right)^2}$$

where A_0 is the intensity at the maximum and a is the exponent of the emission increase.

The parameter b influences the exponent of the emission decay. The parameter d must be tuned so that E_0 describes the maximum of the emission. For $E<<E_0$ Eq. (2.13) becomes:

$$g(E) = e^{a(E-d)} \tag{2.14}$$

and for $E>>E_0$

$$g(E) = e^{-(a-2ab)(E-d)} \tag{2.15}$$

with

$$C = a - 2ab \tag{2.15a}$$

The peak energy of the emission E_0, the maximum intensity A_0 and with Eq. (2.15a) the exponent of the emission decay can be calculated. In Fig. 2.9 the model function is depicted in blue, the experimental data in black. The model function matches the LED emission perfectly.

2.5 Light extraction from a LED

Light generated inside a semiconductor cannot escape from the semiconductor, if it is totally reflected internally at the semiconductor-air interface. If the angle of incidence of a light ray is close to normal incidence, light can escape from the device. However, total internal reflection occurs for light rays with oblique and grazing-angle incidence. Total internal reflection reduces the external efficiency significantly, in particular for LEDs consisting of high-refractive-index materials. This is the case for the investigated AlInGaP. The critical angle for total internal reflection is given by:

$$\sin \beta_{crit} = \frac{n_2}{n_1} \tag{2.16}$$

where n are the refraction indexes. For GaP the refraction index is n_{GaP}=3.02 for photons with an energy of E=1.9eV [20]. Thus at the GaP-air interface the critical angle of total reflection

is $\beta_{crit}^{GaP-air} = 19.3°$. The light in the device is generated by spontaneous emission and radiates uniformly in all directions. This is equal to a point-like light source in the active layer of the semiconductor. Only a fraction of light is emitted inside the critical angle $\beta < \beta_{crit}^{GaP-air}$, allowing escape to the ambient region (air). All other photons are reflected at the interface. Once they are reflected in the LED they are captured in the device until they are absorbed by the substrate or reabsorbed. Figure 2.10 depicts this behaviour (side view), for a photon with a arbitrarily chosen angle $\beta_{\exp} > \beta_{crit}$. The active layer is dark red, at the emission point the escape cones with the critical angles β_{crit} are depicted. Light rays inside this escape cone can escape the device. The red arrows are the ray of one arbitrarily chosen photon with an angle $>\beta_{crit}$. As can be seen the photons are captured in the LED and cannot escape. Normally those photons are absorbed in the substrate or reabsorbed in a QW.

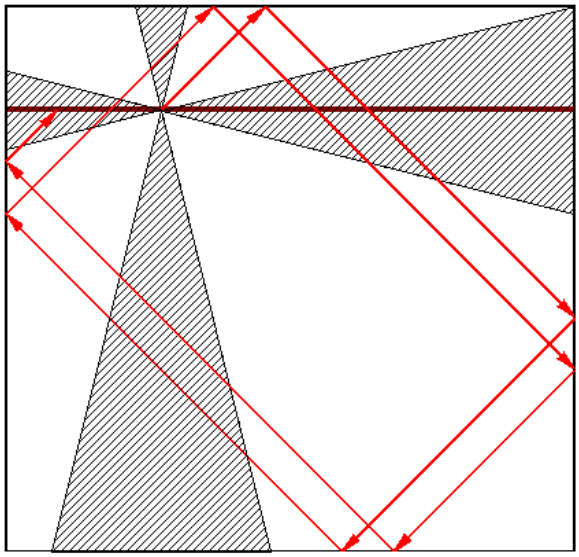

Figure 2.10: A captured photon in a LED structure. The active layer is dark red, the escape cones are hatched. Only photons inside the escape cones can escape the device. A captured photon with an angle $>\beta_{crit}$ is shown as light-red rays.

Additionally, the external efficiency depends on the reflectivity of the interface. Neglecting absorption the reflectivity is given by :

$$R = \left(\frac{n_1 - n_1}{n_1 + n_1} \right)^2 \tag{2.17}$$

Thus the reflectivity at the GaP-air interface is calculated to:

$$R_{GaP-air} = 25.2\% \tag{2.18}$$

With respect to a fully metallised n-side and a partially metallised p-side and without respect to photon recycling the escape efficiency $\eta_{ext}^{GaP-air}$ is calculated to:

$$\eta_{ext}^{GaP-air} = \frac{4.5 \cdot 2\pi r^2 \left(1-\cos\beta_{crit}^{GaP-air}\right)}{4\pi r^2}\left(1-R_{GaP-air}\right) \approx 9.5\% \tag{2.19}$$

Using

$$1-R = \frac{4n}{(n+1)^2} \tag{2.20}$$

and

$$\frac{1}{2}\left(1-\cos\beta_{crit}^{GaP-air}\right) \approx \frac{1}{2}\left(1-\sqrt{1-\sin\beta_{crit}^{GaP-air}}\right) \approx \frac{1}{4n^2} \tag{2.21}$$

The escape efficiency can be written as a function of the refraction index and is given by

$$\eta_{ext}^{GaP-air} = \frac{4.5}{n(n+1)^2} \tag{2.22}$$

for a homogenous photon distribution.

The escape efficiency can be increased by changing the geometry of the LED chips. Examples are given in [7]. Additionally, the device can be embedded in a material with a refraction index between that of GaP and that of air, i.e. resin. Thus the critical angle of reflection is increased and more light can escape the LED [21].

2.6 Non-radiative recombination

In non-radiative recombination processes, the electron energy is converted into vibrational energy of lattice atoms, i.e. phonons. Thus the electron energy is converted into heat. Non-radiative recombination reduces the efficiency of a LED.

Defects in crystal structures are the most common cause for non-radiative recombination. These defects include foreign atoms, native defects and dislocation. In compound semiconductors, native defects include interstitials, vacancies and antisite defects [7]. It is quite common for such defects to form one or several energy levels within the energy gap. These defects are efficient recombination centres, in particular if the energy level is close to the middle of the energy gap which reduces the band-band recombination.

Another non-radiative recombination mechanism is the Auger-recombination. In this process, energy becomes available by an electron hole recombination. The energy is immediately absorbed by another electron which is excited high in the conduction band, or by a hole excited deep in the valence band. The highly excited carriers will lose energy by multiple phonon emission until they are close to the band edge. Figure 2.11 depicts the Auger-recombination.

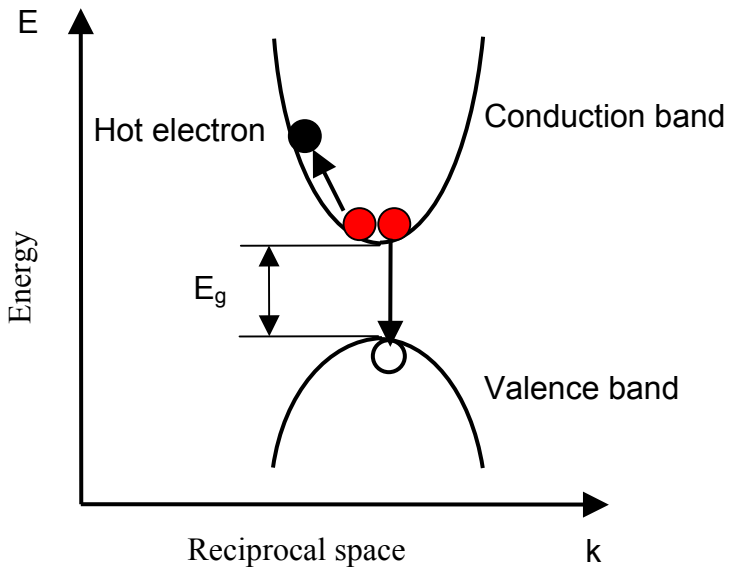

Figure 2.11: Auger-recombination. The energy released by an electron hole recombination is absorbed by another electron.

3 Micro electroluminescence set-up

This chapter describes the construction of an electroluminescence measurement set-up with high spatial resolution. The set-up has been used to accomplish spatially resolved measurements of the emission wavelength and the emission intensity on the lateral LED planes. Measurements perpendicular and parallel to the growth direction are investigated. Additionally, the set-up of the Ulbricht sphere is explained in detail at the end of this chapter.

3.1 Principle of the set-up

Electroluminescence (EL) is the luminescence of a solid caused by an applied electrical current. Luminescence can also be excited by photons (photoluminescence) or by an electron beam (cathode luminescence). EL is the method of choice to investigate the characteristics of completely structured LEDs. A schematic set-up for electroluminescence measurements is shown in Fig. 3.1. The light emission is measured with respect to wavelength (energy) and intensity

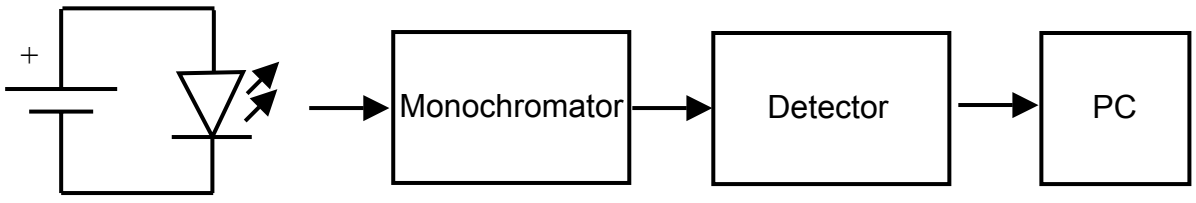

Figure 3.1: Electroluminescence set-up, the emission from the LED chip is coupled into a monochromator. A diode array detects the diffracted light and the data is sent to a PC.

The monochromator 500M from Spex Industries has a focal length of f=50cm and is directly driven by a PC. The grating has a blaze wavelength of λ_{blaze}=750nm and 600 grids per mm.

The detector is a silicon diode array from EG&G, model 1421B. The 1024 diodes are placed on a length of 40mm. A spectral range of 80nm is imaged on the detector array. An optical multi channel analyser OMA 2000 from EG&G reads out the array and sends the data to a PC. The spectral resolution is given by

$$a = \frac{\Delta\lambda}{n} \tag{3.1}$$

where n=1024 is the number of diodes of the array. Thus the resolution is given by:

$$a = \frac{80nm}{1024} \approx 0.08nm \tag{3.2}$$

As control software for the monochromator and detector system WinSpec is used. This software allows the implementation of macros. Therefore new functions can be added to the system.

Investigating local effects in a scale much smaller than the edge length of the device requires a micro electro luminescence set-up (µ-EL). Structural investigations in a range of a few µm are possible with this method.

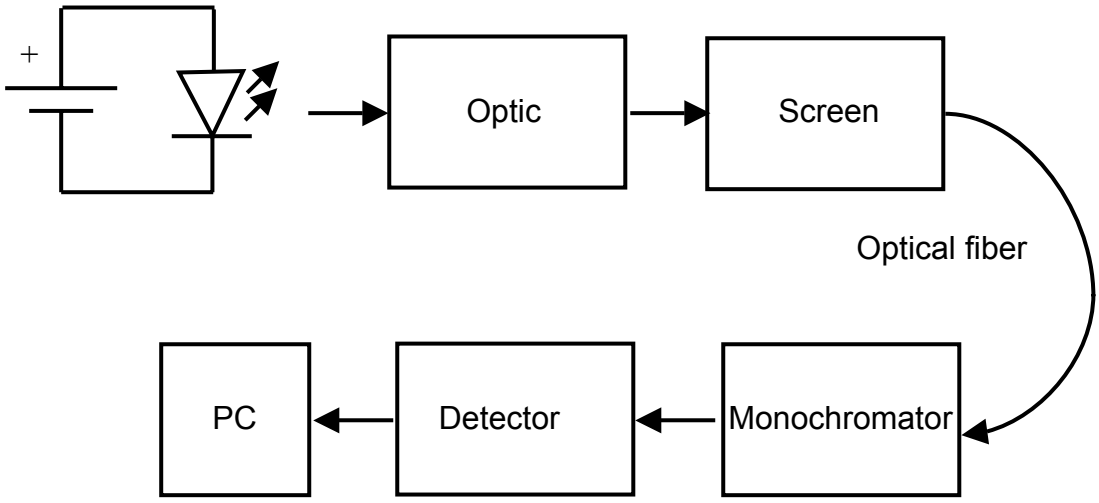

Figure 3.2: Sketch of the micro-electroluminescence set-up. The light from the LED is magnified by a factor of 500 and projected onto a screen. One point of the image with a diameter of 1mm is coupled into an optical fibre and guided to the monochromator. Data is stored in a PC.

To expand the EL-set-up (Fig 3.1) for µ-EL measurements, a further device is inserted into the light path which magnifies the LED Chip by a factor of 500. The image is projected onto a screen. A point from this image with a diameter of 1mm is coupled into an optical fibre and guided to the monochromator. The position of in-coupling can be moved by stepping motors over the hole image range of the LED. Thus every point of the emitting surface can be investigated. The schematic set-up is depicted in Fig. 3.2.

3.2 Optics

To obtain a magnification factor of $m \geq 500$, two convex lenses can be used. The set-up is shown in Fig. 3.3. Lens 1 generates a magnified real intermediate image. Lens 2 magnifies this intermediate image.

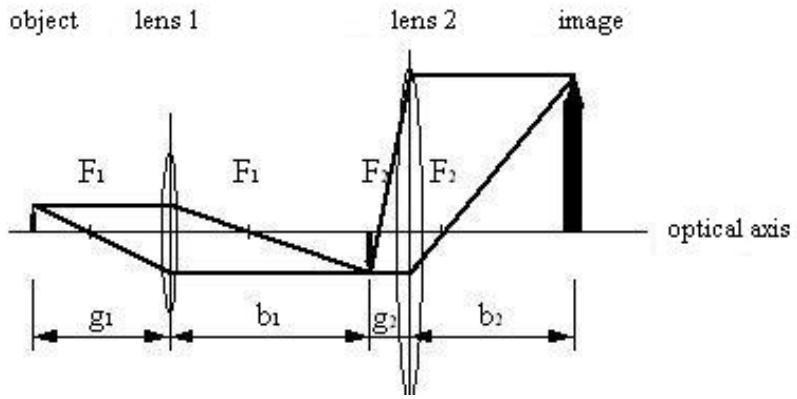

Figure 3.3: Optical set-up. The LED is outside the focal length of lens 1. Lens 1 generates a magnified real intermediate image. Lens 2 magnifies this intermediate image.

Lens 2 can be adjusted with respect to lens 1, thus exact focusing is possible. Instead of simple lenses, objectives from Ernst Leitz Wetzlar GmbH are used. The objective near the LED has a nominal magnification of 10 and a numerical aperture of 0.22. The second objective has a nominal magnification of 20 and a numerical aperture of 0.45.

3.2.1 Step size at the chip surface

The minimum measurement step size at the chip surface depends on the magnification factor of the optics and the diameter of the in-coupling point. As mentioned before, the magnification factor should be $m \geq 500$. It can be estimated experimentally by comparing the image size with the object (LED chip) size. The described set-up achieves a magnification of $m = 610 \pm 15$. The size of the in-coupled light spot is equivalent to the diameter d=1mm of the optical fibre. The minimum step size O_A at the chip surface is given by:

$$O_A = \frac{d}{m} \approx 1.64\ \mu\text{m} \tag{3.3}$$

3.2.2 Space resolution

The space resolution d of an optical device is the minimum distance of two points required to percipience them as two separate points. Is the distance between two points below this limit one observes them as one point. Edge diffraction occurs in every optical system, thus two points can be separated if the main maximum of the first point will be at the first minimum of the second point. So the spatial resolution is given by:

$$d = \frac{\lambda}{2A_N} \tag{3.4}$$

where λ is the wavelength of the light and A_N is the numerical aperture of the optical device. It is defined as:

$$A_N = n \sin\alpha \tag{3.5}$$

where n is the refraction index and α is the half aperture angle of the objective.

The numerical aperture of the µ-EL set-up is A_N=0.28. The emission of the investigated LEDs is $\lambda = (640 \pm 20)$ nm. Thus the spatial resolution of the µ-EL set-up is given by:

$$d = (1.14 \pm 0.04)\ \mu\text{m} \tag{3.6}$$

By comparing Eq. (3.3) with Eq. (3.6) we see that the step size of the set-up and the space resolution are in the same order. Structures which are imaged by the system are also in the resolution limit of the system.

3.3 The positioning system

The optical fibre is driven by two stepping motors. One motor moves the fibre along the x-axis and the other along the z-axis. Both are perpendicular to the optical axis. The minimum step size for both axes is l=1.25µm. The software to control the positioning system has been implemented into the WinSpec software. Thus a synchronisation of luminescence measurement and fibre movement is obtained. Fully automation to measure large areas of the LED chip space resolved is achieved by this set up.
The measured data are directly stored with respect to the coordinates of the emission area, intensity and energy.

3.4 The Ulbricht sphere

An Ulbricht sphere is an optical device for measuring the optical flux from a laser diode, light-emitting diode or bulb. It is a hollow sphere with a diffusely reflecting internal surface, in our case bariumsulphate. The sample is mounted in the centre of the sphere, the detector is attached to the shell of the sphere. A light barrier is used to prevent direct illumination of the detector by the light source. The arrangement causes many diffuse reflections of the emitted light before it reaches the detector. So the light flux becomes uniform at the detector and nearly independent of the spatial distribution of the light emitted by the light source. Basically the detected optical power depends solely on the total emitted intensity. Figure 3.4 depicts a schematic drawing of our Ulbricht sphere.
The spectral response of the selenium detector is shown in Ref. [22].

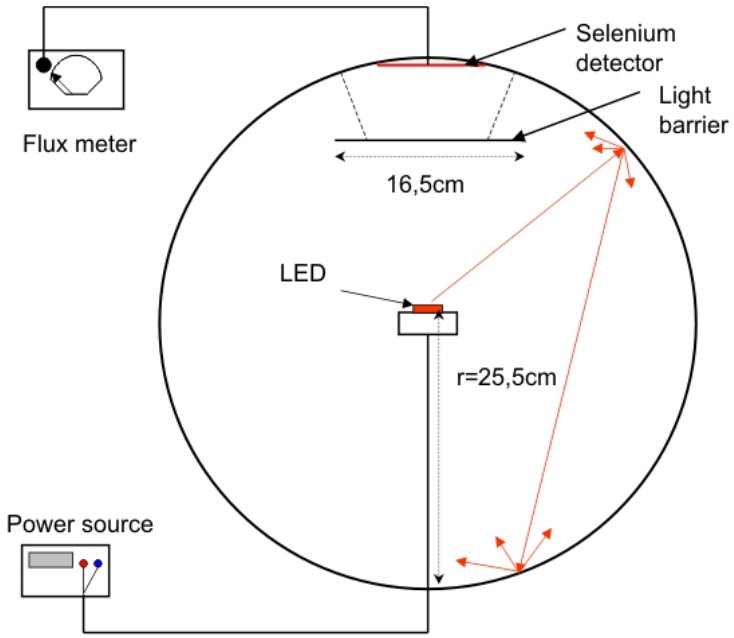

Figure 3.4: Schematic set-up of an Ulbricht sphere. The coating has a high reflectivity and the reflection is diffuse. Thus the light flux is uniform in the sphere.

Ideally the coating on the inner side of the sphere has a very high reflectivity over the required wavelength range, and the reflection is diffuse. Good optical efficiency is obtained, if the sphere is much larger than the light source and the detector.

4 Micro electroluminescence - results and discussion

This chapter discusses the results obtained with the µ-EL set-up described in chapter 3. The samples are described in detail, and the emission of the lateral planes and surfaces of the LED is analysed.

4.1 Description of the samples

The investigated samples are commercially available AlInGaP-MQW LEDs type HWFR-B410 by Lumileds Lighting. The device structure is depicted in Fig. 4.1, the quadratic surface has an edge length of l=232µm. The lateral length is h=280µm. The p-type contact is a circular metal layer with a diameter of d=100µm. The contact material is aluminium followed by a gold – zinc layer which guarantees a perfect ohmic contact to the highly p-type doped GaP window layer. In chapter 2.5 the advantages of window layers are described. Below the GaP window layer is the p-type AlInGaP-UCL (upper confinement layer). The optically active multi quantum well region and the n-type AlInGaP –LCL (lower confinement layer) are aligned. A n-type GaP substrate with a gold contact completes the LED [14]. The metallised areas of the LED are identified as the surfaces of the LED. In the following all the other surfaces are called edge planes and they are denoted “EP” in Fig. 4.1. The orientation in space is also depicted in Fig. 4.1, the z-axis is the direction of the layer deposition.
The emission wavelength of the LED chip at T=20°C and at I=5mA is $\lambda = (630 \pm 5)\,\mathrm{nm}$ which is equivalent to an emission energy of $E \approx 1.96\,\mathrm{eV}$.

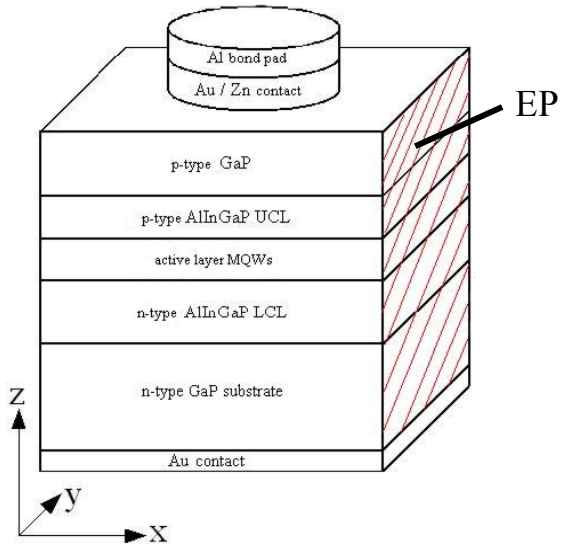

Figure 4.1: Layer structure of the LED chips. "EP" denotes the edge planes (red hatched).

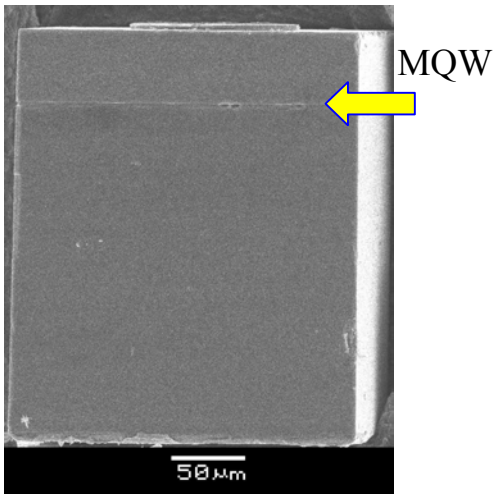

Figure 4.2: SEM image of the LED chip (side view). The optically active MQW region is inside the groove and marked with an arrow.

A scanning electron microscopy (SEM) image of the LED chip is depicted in Fig. 4.2. A groove 50µm below the circular p-type contact is indicated by an arrow. All epitaxial layers, the UCL, LCL and the MQW region are in this grove. This epitaxial structure has originally been grown on GaAs. The GaAs substrate is removed and is replaced by GaP which is transparent to red light.

More details of the production process and the material composition are not known. Also the width of the QWs and barriers are not known, but can be estimated to be 5nm.

4.1.1 The HWFR-B 410 LED: basic properties

In this chapter the basic electrical and optical properties of the HWFR-B 410 LEDs used for our investigations are described. Figure 4.3 depicts the *I-V* characteristics of the LED chip measured in a range between –2.5V and 2.5V.

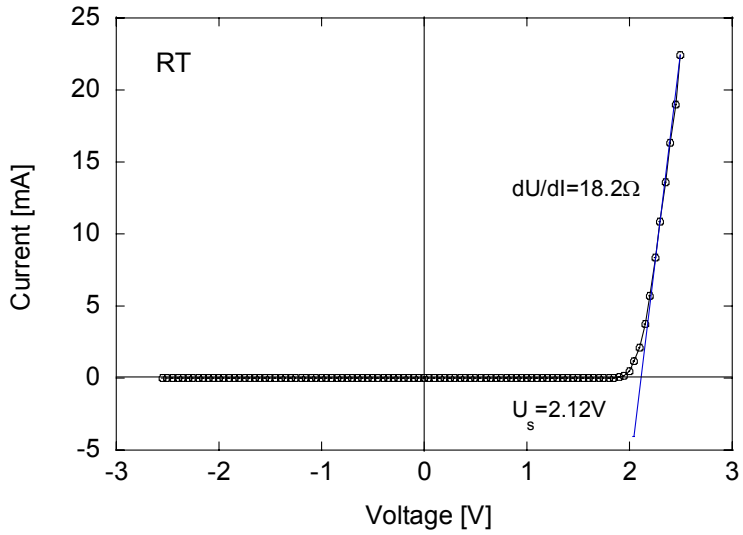

Figure 4.3: Current-voltage characteristic of the HWFR-B410 LED at room temperature.

The threshold voltage is determined *to* V_{th}=2.12V and the differential resistance in forward direction is R_{Diff}=18.2Ω.

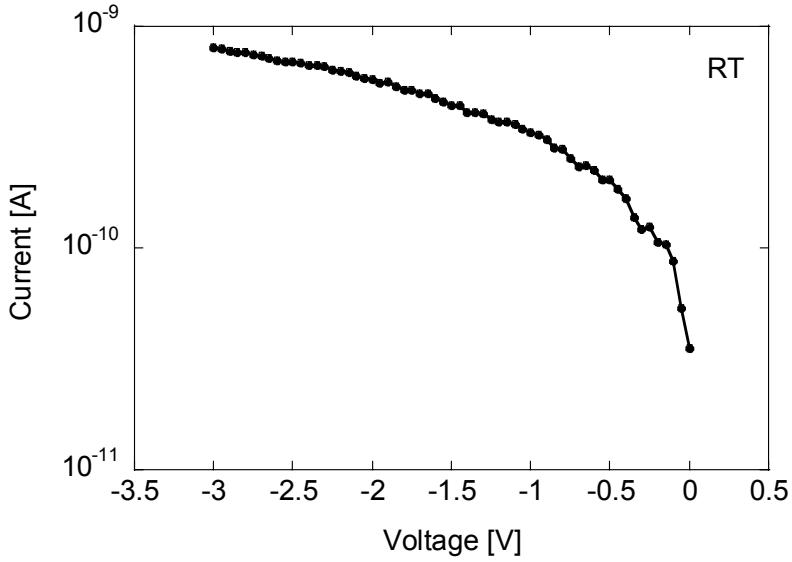

Figure 4.4: Reverse current versus reverse voltage of the HWFR-B410 LED.

To investigate the proper reverse current a picoamperemeter Keithley 6485 is used. The results are shown in Fig. 4.4. The reverse current increases from $I = 3.5 \cdot 10^{-11}$ A at about 0V to $I = 7.8 \cdot 10^{-10}$ A at V=-3V.

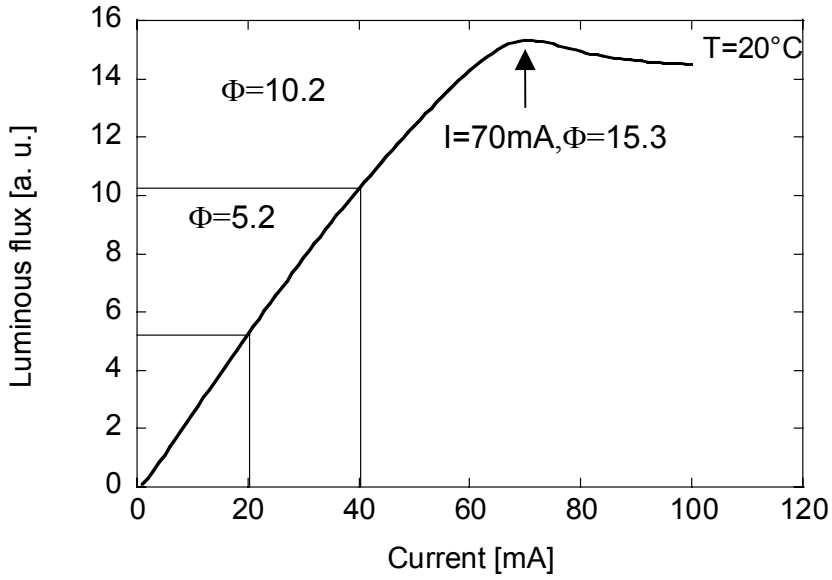

Figure 4.5: Luminous flux Φ versus forward current. The maximum luminous flux at T=20°C is measured at a forward current of I=70mA.

Figure 4.5 depicts the total luminous flux Φ, which was measured in the Ulbicht sphere, versus forward current. The luminous flux increases linearly up to *I=40mA*, then the luminous flux starts to saturate. At an ambient temperature of *T*=20°C and at *I=70mA* the maximum luminous flux is reached. The maximum current recommended by the manufacturer is *I*=20mA.

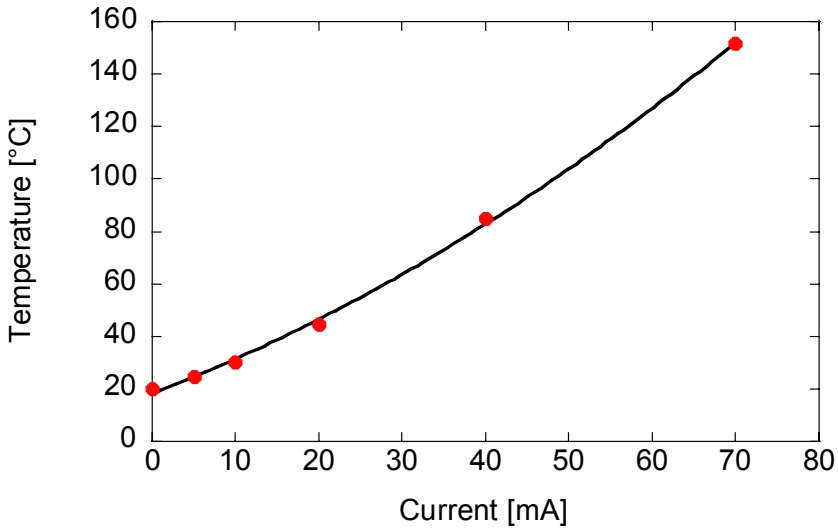

Figure 4.6: Junction temperature versus forward current.

Figure 4.6 shows the junction temperature versus forward current up to *I*=70mA. This result is obtained in a two-step process. The LED was heated in a cryostat applying a constant forward

current of I=1mA. The emitted light was coupled into a monochromator and the peak wavelength shift versus temperature was measured. A linear relationship between the peak wavelength decay versus temperature was found. In a second experiment the peak wavelength shift versus increasing forward current of the same sample was measured. Thus a relationship between the LED temperature and the forward current is created by combining both results.
The junction temperature for $I \leq 1\,\mathrm{mA}$ is approximately room temperature. The dependence between the temperature and the dissipated power P_d, converted to heat is:

$$T \propto P_d \tag{4.1}$$

According to [15] P_d is given by:

$$P_d = (1-\eta) I_f V_f + \eta I_f^2 R_s \tag{4.1.a}$$

where η is the external quantum efficiency, V_f is the forward voltage, I_f is the forward current and R_s is the serial resistance. The changes in V_f caused by current is much smaller than V_f ($\Delta V_f << V_f$), and η *and* R_s are constant. Thus Eq. (4.1) and Eq. (4.1.a) indicate that the junction temperature depends linearly and quadratically on the forward current.
The experimental data have been fitted by

$$T_j(I) = 291.4 + 1.2 \cdot I \ + 0.01 \cdot I^2 \tag{4.2}$$

For a forward current of I=70mA the junction temperature is determined to T=152°C.
Heating the LED by forward current we observe a red shift of the emission due to the decreasing energy gap with increasing temperature. The blue shift of the emission which is caused by band filling with carriers is superposed by the red shift. According to [7] the blue shift is negligible in the AlInGaP system.

4.2 Sample preparation

For mechanical stability, electrical and thermal conductivity reasons the samples are glued with their n-side onto a copper board. The glue, XCA 80210 from Emerson & Cuming, hardens within 2 min at T=100°C. In chapter 4.6.1 we show that this hardening process has no effect on the performance of the LED. The p-side of the LEDs are contacted by a tip probe. For practical reasons five LEDs are deposited in a row on the above mentioned copper board and labelled E01 to E05. The board with the five LEDs is installed in the µ-EL set-up.

4.3 Experimental details of micro-electroluminescence measurements

It has been shown in Chapter 3.1 that the detector of the µ-EL set-up is a diode array which can detect a specified spectral range during one measurement. Therefore the monochromator has been adjusted to a centre wavelength of λ=640nm. By means of the grating with 600 grids per mm light with a wavelength of λ=640nm is projected onto the centre of the detector array and a full range of 80nm is projected to the diode array. This means a spectrum from λ_1=600nm to λ_2=680nm can be measured instantly without moving the grating in the monochromator. This range covers the full area of interest during the investigations and a fast measurement is guaranteed.

The calibration of the monochromator has been done with two lasers with wavelengths of λ_1=632.8nm and λ_2=639.3nm, respectively. The spectra of the calibration measurements is shown in Fig. 4.7. The emission of laser 1 has been measured to $\lambda_1^{'} = (632.84 \pm 0.08)\,\text{nm}$. The emission of laser 2 has been measured to $\lambda_2^{'} = (639.32 \pm 0.08)\,\text{nm}$. The differences $\Delta\lambda_1$=0.04nm and $\Delta\lambda_2$=0.02nm are within the resolution limit (see Eq. (3.2)), of the monochromator-detector system.

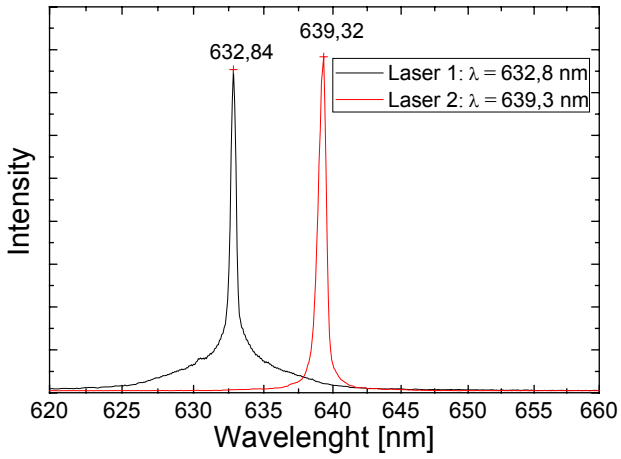

Figure 4.7: Calibration of the monochromator with two laser lines at λ_1=632.8nm and λ_2=639.3nm.

Before the surfaces or edge planes of the LED chip can be investigated the magnified image must be focused on the screen. Focusing the image is easy if one of the surfaces of the chip is investigated. One can directly use the image edges of the device as reference. Focusing to the active layer is more difficult. First one has to focus to the top (p-contact) surface and then moving the focal point 50µm (distance from the top surface to the active layer) inside the chip by adjusting the second lens. A detailed description is given in appendix A. To find out the magnification the dimensions of the mapped image can be measured and compared with the dimensions of the LED chip. After measuring the background count rate at I_{meas}=0mA, adjusting the monochromator slit and integration time, the measuring routine can be started.

4.4 Temperature analysis

The carrier temperature in the device can be calculated by analysing the exponential decay of the emission. This exponential decay *c* of the emission can be extracted from Eq. (2.15a). The Fermi distribution of the electrons in the conduction band describes this exponential decay and is given by:

$$F(E) = \frac{1}{\exp\left(\frac{E - E_F}{k_B T}\right)} \tag{4.3}$$

If we equate the exponential decay c with the Fermi function one obtains:

$$c(E-d)=\frac{1}{k_B T}(E-E_G) \tag{4.4}$$

with $d \approx E_G$ we can derive a relationship between the exponential decay of the emission and the carrier temperature.

$$T_e = \frac{1}{k_B c} \tag{4.5}$$

4.5 Experimental details

4.5.1 Glue hardening

First the influence of the glue-hardening process must be investigated. The glue hardens within 2 minutes at T=100°C. To investigate a change in the LED performance under these conditions, LEDs are thermally treated at T=200°C and for different lengths of time. Before starting the experiment the *I-V* characteristic is measured. The next measurements are performed after 2 min at T=200°C, after 3 min at T=200°C up to 5min at T=200°C. Each time the LED chip is cooled down and the *I-V* characteristic is measured. The results are shown in Fig. 4.8, the current is depicted in a logarithmic scale.

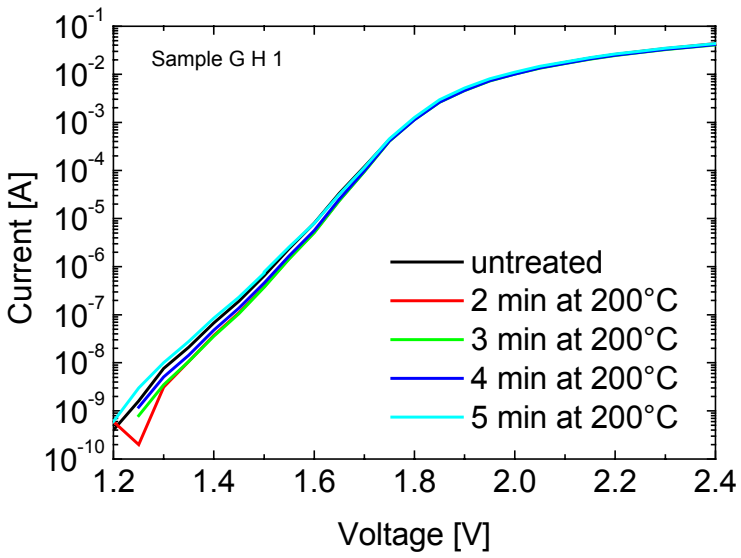

Figure 4.8: Forward current-voltage behaviour after different thermal treatments.

4.5.2 Spectral measurements along the z-axis

Space resolved measurements from the EP and from the top surface have been made. The spectral range for all measurements is $606nm \leq \lambda \leq 674nm$ which is equivalent to $1.84eV \leq E \leq 2.045eV$.

The emission from the EP with respect to z has been investigated. Selected spectra are depicted in Fig. 4.9 and Fig. 4.10. The measurements are made with sample E04 at x=131.8µm and at I_{meas}=10mA. The emission from the n-side is depicted in Fig. 4.9 and from the p-side in Fig. 4.10. The top surface emission is shown in both figures as black curve. Due to the fact that the location of the active layer is not exactly known, the emission with the highest intensity is chosen as reference and set to z=0. Positive z-values are directing toward the p-region. In the low energy region the increase of the intensity is exponential. The emission also decreases exponentially in the high energy region. The energies E_1 and E_2 are the two emission maxima, and their intensities depend on z. For large distances from z=0 the intensity of the total emission decreases whereas E_2 remains constant and the intensity of E_1 decreases. Also, the emission for large distances is equivalent to the top surface emission.

Additionally the influence of the drive current on the emission spectrum is investigated. Space resolved measurements of sample E04 along the z-axis at different drive currents and constant x are investigated. The forward current is varied from I=1mA to I=20mA in steps of 1mA. The characteristic of the emission is similar to the characteristic described in the previous paragraph. Thus only the emission at z=-1µm and at z=-7µm (in the GaP substrate) are shown. Figure 4.11 depicts the emission at z=-1µm (just below the active layer). By increasing the forward current I_{meas} the intensity increases. The intensity maximum at E_1 dominates the emission. E_1 also decreases with increasing forward current.

Figure 4.12 depicts the emission at z=-7µm, in the GaP substrate. The emission E_2 dominates the spectral behaviour and E_2 decreases with increasing forward current.

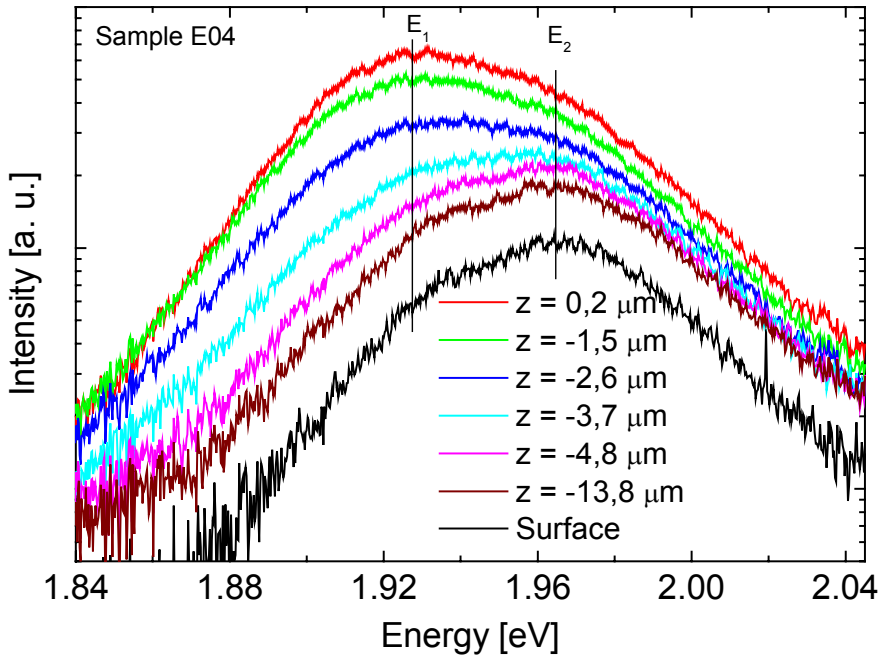

Figure 4.9: Electroluminescence along the z-axis in the n-type region. The black curve is the emission from the top surface. The active layer is at z=0, negative z points toward the n-contact.

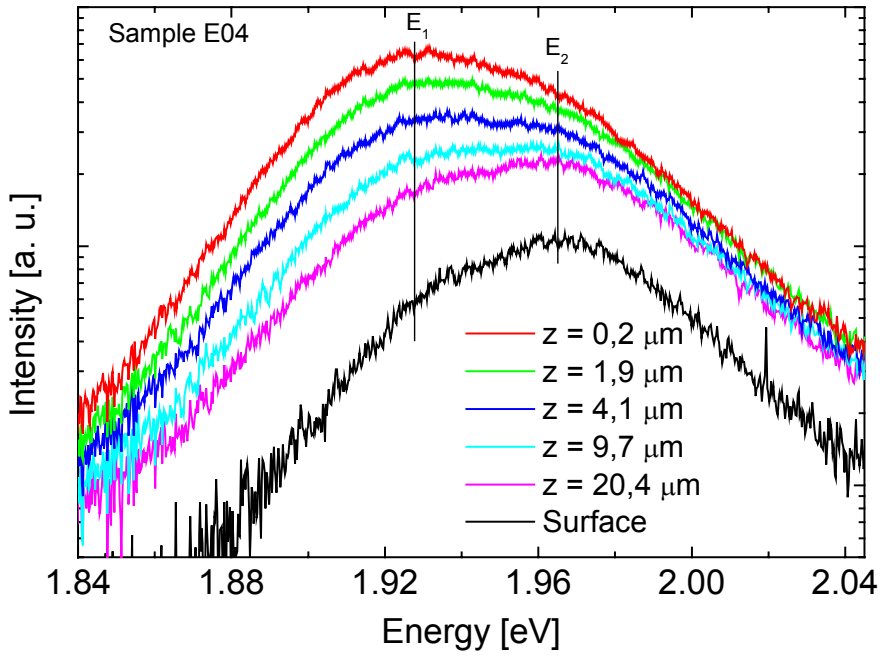

Figure 4.10: Electroluminescence along the z-axis in the p-type region. The black curve is the emission from the top surface. The active layer is at z=0, positive z points toward the p-contact.

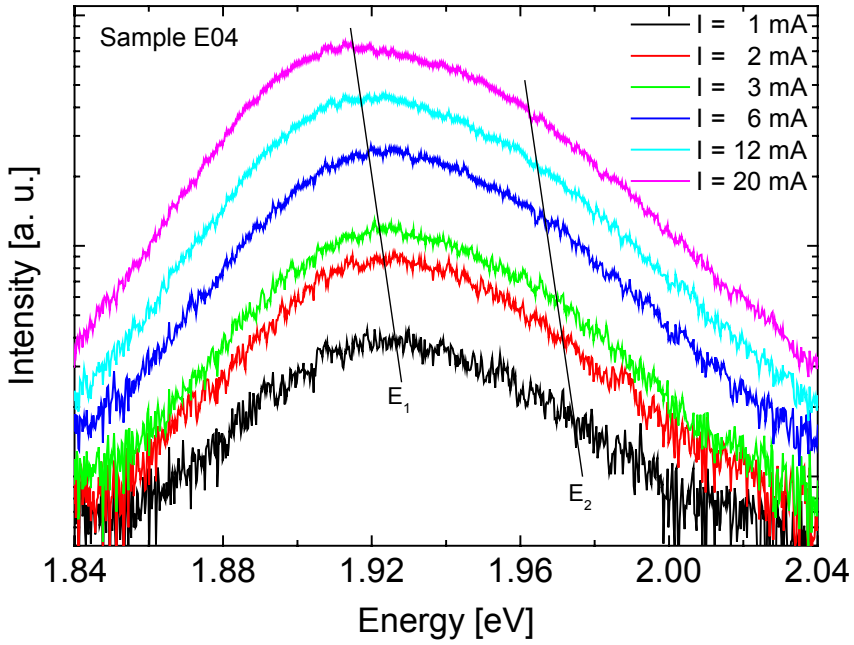

Figure 4.11: Emission at different drive currents at z=-1µm, just below the active layer.

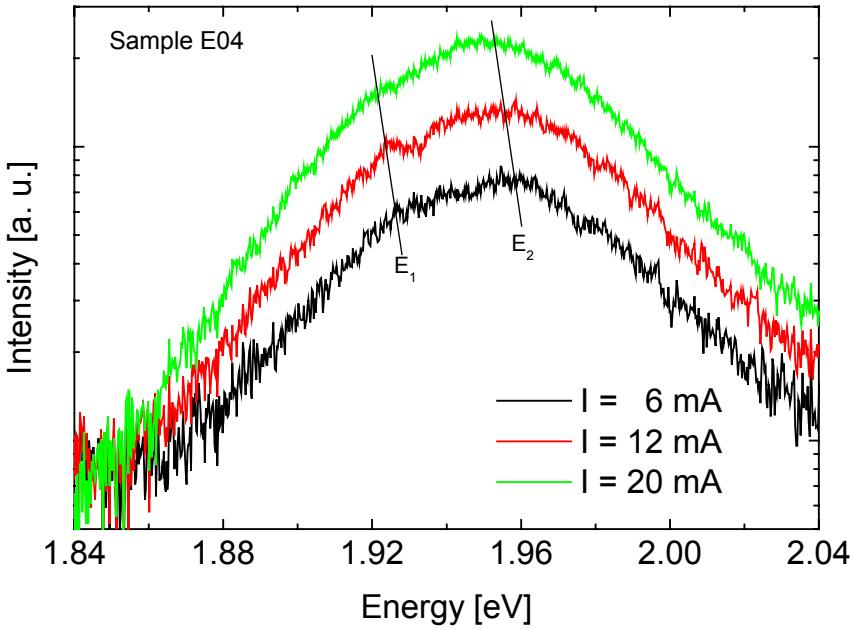

Figure 4.12: Emission in the GaP substrate at z=-7µm at different drive currents.

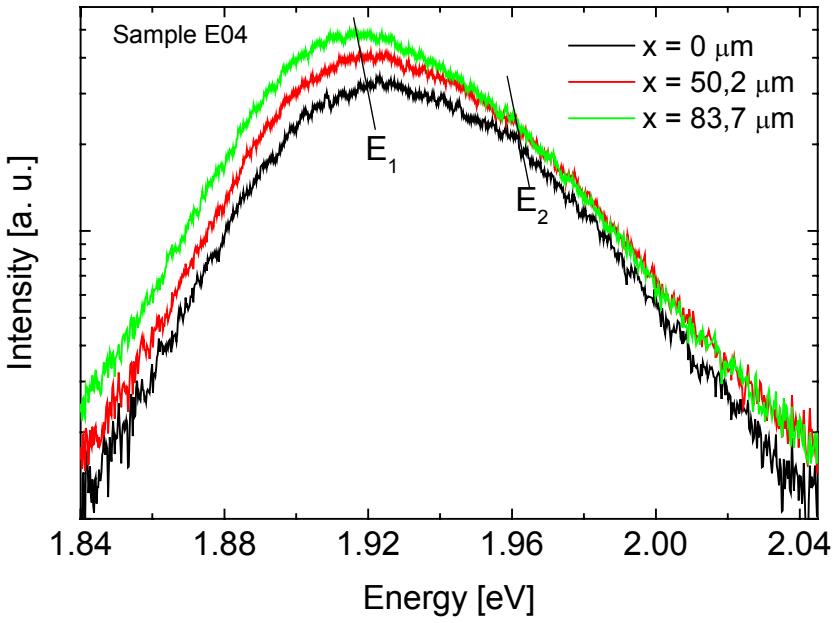

Figure 4.13: Emission at z=-1µm, below the active layer and at different x-values.

Figure 4.13 depicts the dependence of the emission spectra for different x-values. The forward current is I_{meas}=10mA and z=-1µm, x=0 is the edge of the LED chip. The intensity decreases at the edge of the LED and E_1 increases.

4.6 Discussion of the results

4.6.1 Glue hardening

This paragraph discusses the influence of glue hardening on the LED performance. Figure 4.8 shows the *I-V* characteristics after different thermal loads as described in chapter 4.5.1. For voltages V >1.2V an exponential increase is observed up to V=1.8V. Then the serial resistance dominates the characteristic and the device acts like an ohmic contact. No significant change in the *I-V* characteristics can be observed during this experiment.

Between V=1.2V and V=1.8V the serial resistance is slightly different, but no correlation with the degradation time can be observed. The reason for this behaviour is a variation in the contact resistance. Before every measurement the sample must be contacted by a tip probe.

Different pressures of the tip causes different contact resistances. Therefore, we conclude, that the performance of the LED is not affected by the gluing process.

4.6.2 Micro EL along the z-axis

Figure 4.9 shows that the emission spectrum is a superposition of two lines with maxima at E_1 and E_2. To fit the emission spectra Eq. (2.13) has to be applied for each line. Thus the fit function is modified to:

$$g(E) = \frac{A_1}{N}\frac{\exp(a(E-E_1+e))}{[\exp(ab(E-E_1+e))+1]^2} + \frac{A_2}{N}\frac{\exp(a(E-E_2+e))}{[\exp(ab(E-E_2))+1]^2} \tag{4.6}$$

where

$$N = \frac{\left(\frac{1}{2b-1}\right)^{\frac{1}{b}}}{\left(\frac{2b}{2b-1}\right)^2} \quad \text{and} \quad e = \frac{\ln\left(\frac{1}{2b-1}\right)}{ab}$$

A_1 is the intensity at E_1 and A_2 is the intensity at E_2.

Due to the strong correlation of the parameters in Eq. (4.6) both terms use the same a and b parameters. The values of the energies E_1 and E_2 are extracted from an emission spectrum with pronounced energy peaks and set to constant values. Thus one obtains the intensities A_1 and A_2 in dependence of the z-position. Figure 4.14 depicts the intensity A_1 of the maximum E_1 and the intensity A_2 of maximum E_2 as a function z.

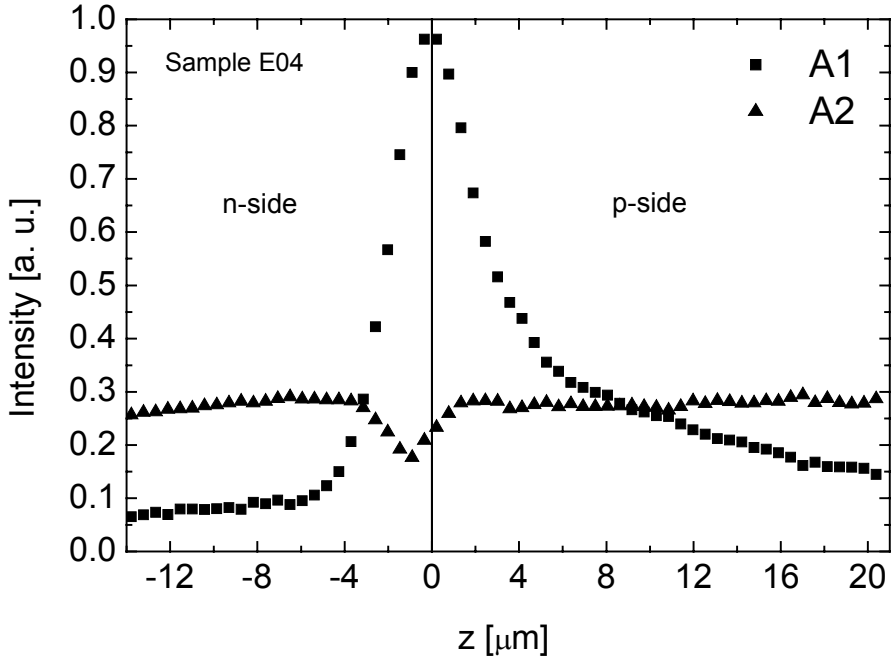

Figure 4.14: Intensity A_1 of maximum E_1 and intensity A_2 of maximum E_2 as function of distance z from the active layer.

The origin of the z-axis is the position of the active layer which corresponds to the intensity maximum A_1. Positive values of z point to the p-contact. The intensity is plotted over a space interval $-14\mu m \le z \le +21\mu m$. For z<-5µm the intensity A_1 increases slightly ($5 \cdot 10^{-3}\,\mu m^{-1}$) with increasing z. For z>-5µm the intensity A_1 strongly increases up to z=0. Then the intensity decreases strongly up to z=4µm. After this point the slope flattens.

The behaviour of intensity A_2 at E_2 is quite different. It is nearly constant throughout the whole range of the measurement. From z=-4µm to z=-1µm the intensity decreases linearly and then increases linearly at z=2µm to the same level of intensity.

4.6.3 Modelling A_1 and A_2 versus z

The area under the emission spectrum of an LED is understood as the emitted energy per solid angle. Since with increasing intensity the shape of the emission spectrum does not change, the peak intensity and the area under the spectrum are proportional. Therefore one can investigate the behaviour of the peak energy along the z-axis instead of the integral of the emission spectrum. The active layer (AL) inside the LED chip is a volume V with the length x_a, the

width y_a and the depth z_a. The coordinates *x, y, z* are similar to the coordinate system introduced in chapter 4.1. Due to the flatness of the active layer, z_a is much smaller than x_a and y_a, thus x_a and $y_a >> z_a$. Because of the light generation by spontaneous recombination, every part volume of the active layer emits the same energy per solid angle. The detector focuses on the active layer with a surface of πr^2 . Thus the detector is measuring the volume $\pi r^2 z_a(1+\tan\beta_{NA})$ which has the geometry of a truncated cone. Angle β_{NA} is the angle of the observation cone with respect to the z-axis. Light rays with an angle larger then β_{NA} are not detected. The numerical aperture *A* of the set-up is defining β_{NA}, $(A = n_{air} \sin\alpha_{NA})$.

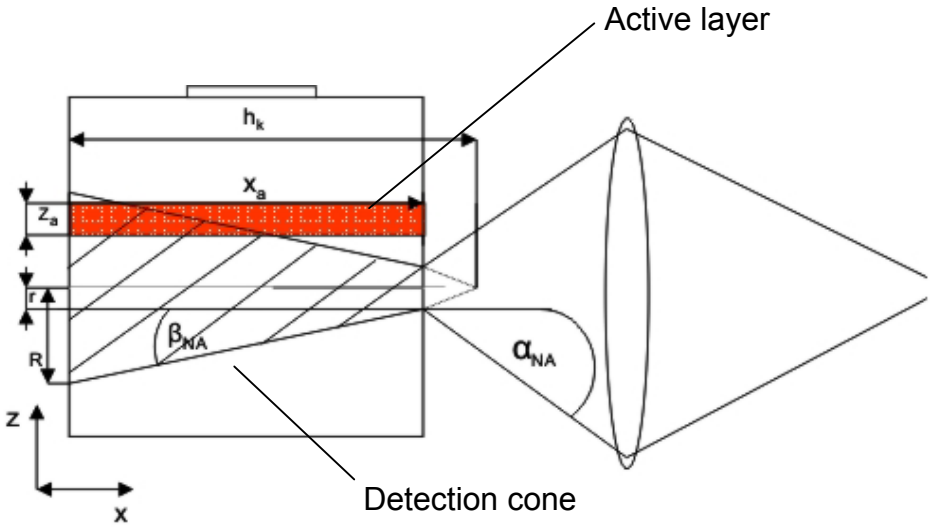

Figure 4.15: Observation cone inside the LED chip. The cone (hatched) divides the active layer (red).

The light is refracted at the semiconductor-air interface and β_{NA} is given by the law of Snellius:

$$A = n_{air} \sin\alpha_{NA} = n_{GaP} \sin\beta_{NA} \qquad (4.7)$$

where n_{air} is the refraction index of air and n_{GaP} is the refraction index of the semiconductor material. The light intensity which is measured by the detector is proportional to the intersection of the active layer and the observation cone. During the measurement the observation cone is moved through the active volume (where the light is generated) along the z-axis. Therefore the detected light is generated in a volume which has the geometry of conic sections, (see Fig. 4.15). The observation cone is the hatched area inside the LED chip. The active layer inside the LED chip is red cross hatched. By moving the cone (in z direction) over the active layer the intersection increases or decreases and more or less light is detected.

The intersection can be approximated by triangles and then the intensity as a function of z is given by:

$$I_x(z) \propto \sqrt{R^2 - z^2} - \frac{z^2}{R} \ln \frac{|z|}{R + \sqrt{R^2 - z^2}} \tag{4.8}$$

where R is the radius of the cone base area. The derivation of Eq. (4.8) is shown in appendix B. Thus the behaviour of A_1 near the active layer is described by Eq (4.8). We conclude that the emission E_1 is homogeneously generated in the active layer of the LED chip. The intensity A_1 is a function of the intersection between the active layer and the detection cone inside the LED chip. Therefore the intensity A_1 is a function of the z-position of the in-coupling fibre.
However, surface roughness and scattering effects affect out-coupling of light at large distances from the active layer. Thus the intensity cannot be described by Eq (4.8) for large distances.

The intensity A_2 at E_2 remains constant over the measurement range. The small decrease of intensity around the active layer is neglected at this point and discussed later. The reason for the emission around E_2 must be different to the emission around E_1 due to their fundamental differences. The light of A_2 can be generated in the active layer, but must then escape with a precipitous angle to the surface normal. Then the light is uniformly distributed in the whole chip. Surface roughness and scattering allow some light to escape causing a homogenous light distribution at the surface as a consequence. Self absorption at the active layer can cause such a precipitous angle with respect to the surface normal, but this effect seems to be too weak.
Alternatively the light could have been generated in the GaP substrate and the GaP window layer. This would directly lead to homogenous light distribution. Due to the larger bandgap of GaP in comparison to the AlInGaP alloy, the emission of E_2 is at higher energies. This is shown in Fig. 4.10.
In both cases the reduction of A_2 near the active layer is explained by the self absorption in the active layer. The bandgap in the active layer is smaller than in the GaP substrate and the window layer. Therefore the self absorption is larger in the active layer. The probability of self absorption increases with the distance the photons cover in the active region. Thus the value of A_2 decreases over the active layer.
Both models cannot explain the energy value of E_2. There cannot be two transitions energies in the active layer. Also E_2 is too small to be caused by impurities in GaP. The bandgap of

GaP is $E_G^{GaP} = 2.2\,\text{eV}$ [8] and E_2<1.97eV. Therefore the lattice impurity must have an activation energy of E_A>230meV. Also they must be homogeneously distributed and the concentration of these impurities must be rather high. Doping materials are in concentrations which are sufficient to generate light with this intensity. However, the activation energy of the doping materials is rather low, Mg has an activation energy in GaP of E_A=53.5meV [24]. The emission E_2 could be generated in the confinement layers (CFs). The energy gap could be in the range of E_2. But a homogenous light distribution cannot be explained by a light generation in the CFs.

4.6.4 Current dependence of the peak energies

In chapter 4.5 it is shown that the energies E_1 and E_2 shift to lower energies by increasing the forward current. Figure 4.16 depicts the shift of E_1 (AL) versus the drive current in a range of 1mA<I_{meas}<20mA. The characteristic is linear, plotted as black curve in the diagram and can be fitted by:

$$\frac{dE_1}{dI} = -0.38\frac{eV}{A} \tag{4.9}$$

This red shift is a temperature effect. Every real diode has a serial resistance R_s where a part of the applied electrical power is converted to heat. By increasing the electrical power the produced heat also increases and the temperature at the device rises. The lattice constant of the semiconductor increases by heating up. The bandgap energy E_G decreases by increasing lattice constant and the emission shifts to lower energies. Therefore AlInGaP LEDs shift to the red with increasing forward current. This characteristic can be quite different in other semiconductor materials. For example see [7] for blue emitting GaN LEDs.

Also the increased electron-phonon interaction leads to a band-gap shift to lower energies. The band-gap shift due to electron-phonon interaction in AlInGaP is not known. But in [23] the band-gap shift in GaAs/AlAs superlattices is measured to $dE/dT = -198\,\mu\text{eVK}^{-1}$.

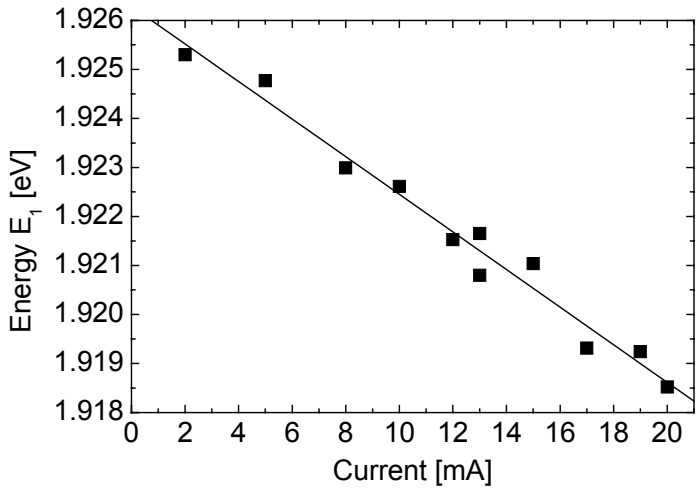

Figure 4.16: Peak energy E_1 versus forward current at z=-1µm.

The carrier temperature inside the LED chip can be calculated by the exponential decay of the emission (see chapter 4.4). A temperature calibration can be made by assuming the carrier temperature to be at room temperature at I=2mA. Increasing forward current causes an increasing carrier temperature and leads to a decrease of the E_1 peak energy. Figure 4.17 depicts the decrease of peak energy versus carrier temperature. The temperature range is $20°C \le T \le 60°C$ and a linear behaviour is observed which can be described by:

$$\frac{dE_1}{dT} = -0.16\frac{meV}{K} \tag{4.10}$$

Combining Eq (4.9) and Eq (4.10) one obtains the relation between carrier temperature and forward current. The result is shown in Fig. 4.18. A linear characteristic is obtained which can be described by:

$$\frac{dE_1}{dI} = 1.6\frac{K}{mA} \tag{4.11}$$

A temperature dependence of E_2 could not be observed because of the low intensity of this emission.

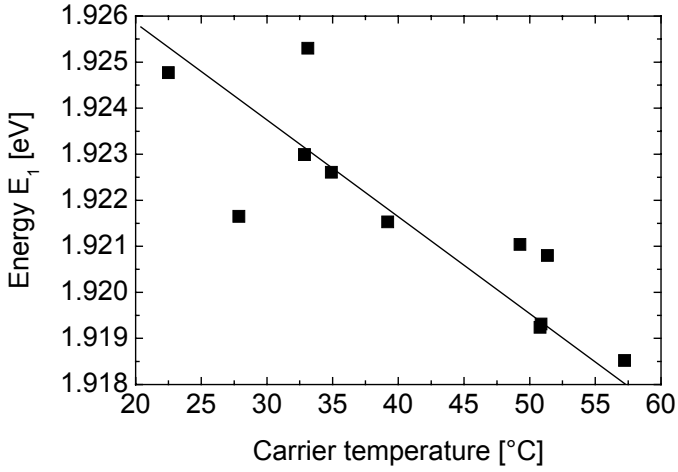

Figure 4.17: Peak energy of the emission versus carrier temperature.

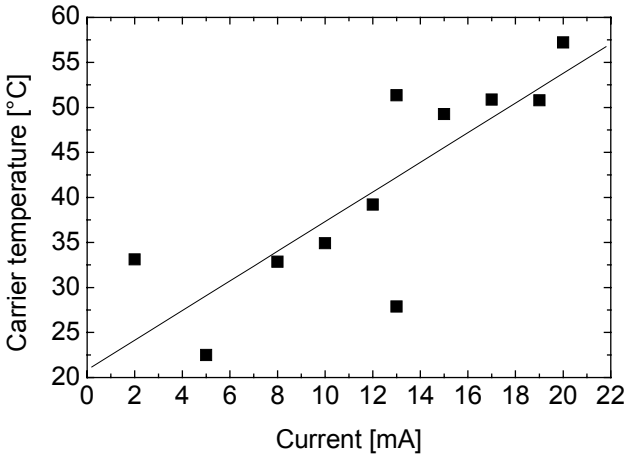

Figure 4.18: Increase of the carrier temperature as function of the LED forward current.

4.6.5 Measurements along the x-axis

The emission shift as a function of the x-coordinate was also measured to investigate the current homogeneity as a function of x. In chapter 4.5 we have demonstrated that the emission shifts towards lower energies by moving the point of measurement towards the centre of the LED. Figure 4.19 depicts the change of E_1 from the edge of the LED chip (x=0µm) to the centre of the LED chip (x=90µm). We assume an inhomogeneous current distribution inside the LED chip due to the circular p-side contact. The p-side contact covers only a part of the LED surface and the n-side contact covers the hole back side of the LED chip. Due to the

distance between the active layer and the p-contact, the current distribution in the active layer is not homogeneous. In the centre a higher current density is expected. Thus we assume a higher temperature in the centre of the LED than at the edges. This leads to a red shift of the emission as described in chapter 4.6.5

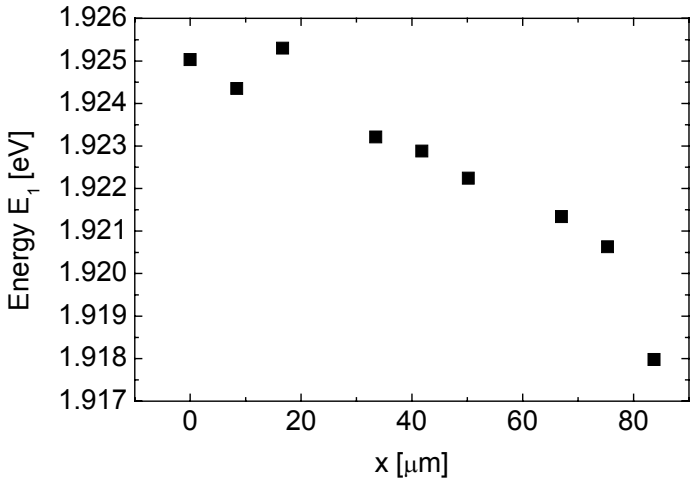

Figure 4.19: Peak energy E_1 as function of the x-coordinate. A red-shift is observed when moving the point of measurement from the centre to the edge of the LED.

The edge plane emission of the LED chip strongly depends on the z- position. Near the active layer the emission is dominated by E_1. The energy E_1 depends on the device temperature and therefore also on the current through the device. The energy of E_1 shifts to lower values by increasing the drive current. Temperature analysis can be done calculating the high energy decay of the emission. The intensity of E_1 is a function of z. At z=0 - at the active layer - the intensity is at maximum. The emission E_1 also depends on the x-coordinate. At x=0 at the edge of the LED the intensity of E_1 is lower and the energy value of E_1 is higher. A higher current density and thus a higher temperature in the centre of the LED causes this characteristic.

Energy E_2 dominates the emission for larger distances from the active layer. Also E_2 is a function of the drive current and shifts to lower energies by increasing drive current. The intensity of E_2 is almost independent of z. Only near z=0 the intensity decays.

5 Effects of LED aging

5.1 Degradation under high forward current

In this chapter we describe the change of the LED properties aged under high forward current. In paragraph 5.2 we focus on the positive aging effects. The characteristics of five different samples treated with two different currents is investigated. Paragraph 5.3 describes the characteristics of two LED chips treated at a forward current of I_{degra}=120mA. The treatment took as long as 704h and the focus of the investigation is on the negative degradation effects.

5.2 Positive aging

During the degradation experiments an increase of luminous flux is observed which is defined as “positive aging”. This positive aging during the first few hours of aging time leads to an increase of luminous efficiency and therefore to a higher light output. In addition, an improved current-voltage characteristic in forward direction below the threshold voltage is observed. Also a decreased leakage current is measured. The samples listed below are investigated and the results are discussed in detail.

Sample 1: Resin encapsulated LED I_{degra}=70mA, #33_C1
Sample 2: Chip only I_{degra}=120mA, LZ-EL 1
Sample 3: Chip only I_{degra}=120mA, LZ-UL 2
Sample 4: PMMA encapsulated LED at I_{degra}=120mA, soldered chip, H G 1
Sample 5: PMMA encapsulated LED at I_{degra}=120mA, glued chip, H G 2

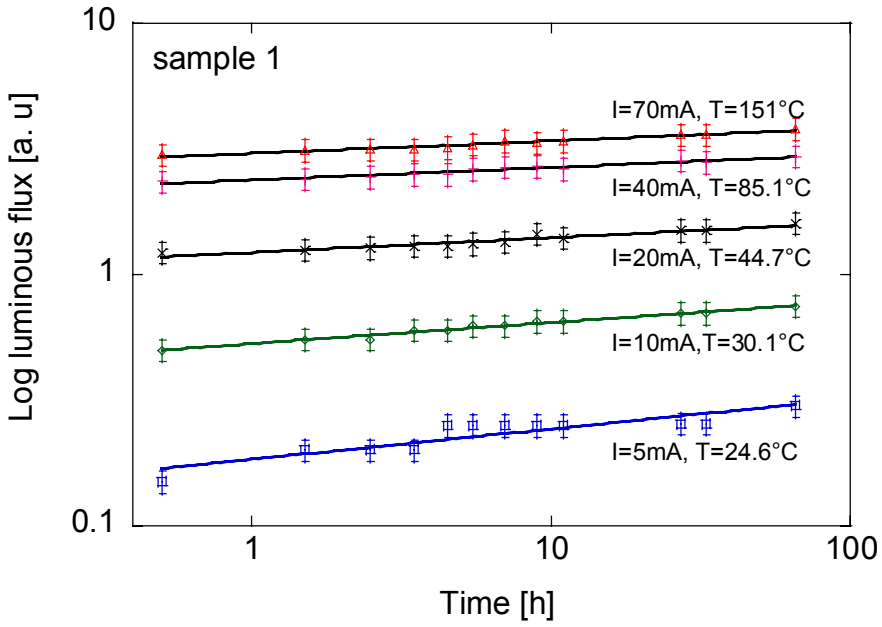

Figure 5.1: Sample 1, luminous flux versus time and different measurement currents. Burn-in behaviour and positive degradation with increasing luminous flux for $I_{meas} \geq 5mA$ *is observed.*

The LED #33_C1 is treated with a forward current of I=70mA which causes a temperature of T=151°C at the junction of the device. From time to time the degradation is interrupted and the device is cooled down to room temperature. After cooling down the device is driven by forward currents of I_{meas}=5mA, 10mA, 20mA, 40mA and 70mA and the total luminous flux is measured in an Ulbricht sphere. After the measurements the degradation is continued at I_{degra}=70mA. The experiment is stopped after t=65h. Figure 5.1 shows the results. The luminous flux versus aging time in a logarithmic scale is plotted. Clearly an exponentially increasing luminous flux is observed for measuring currents $I_{meas} \geq 5mA$. In Fig. 5.2 the normalized luminous flux versus the measurement current is depicted.

For a measurement current of I_{meas}=5mA the light output is increased by a factor of two after an annealing time of t=65h at I_{degra}=70mA. The efficiency improvement decreases by increasing measurement current. At I_{meas}=20mA the enhancement is only 30% and then seems to saturate. At I=40mA the improvement of light output is only 25% which is the same as at I_{meas}=70mA within the experimental error.

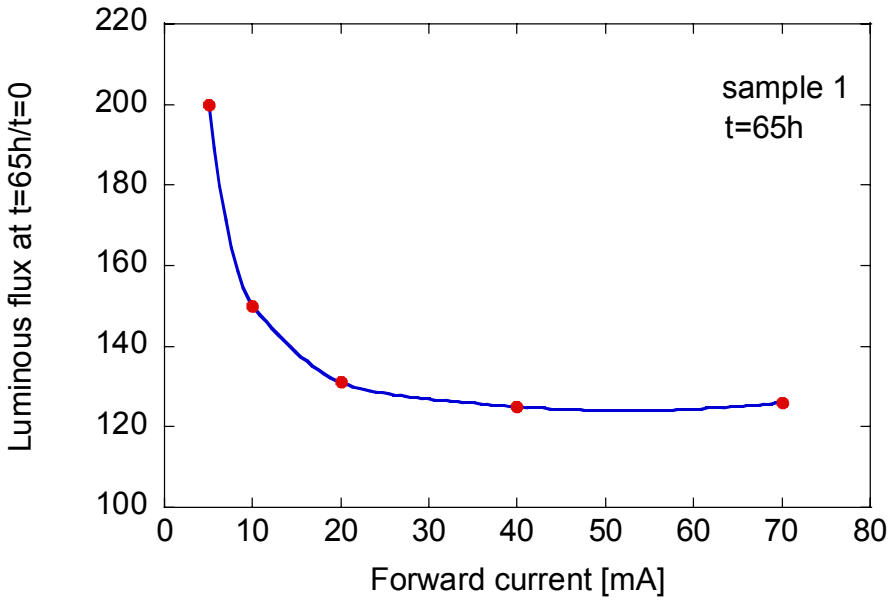

Figure 5.2: Luminous flux versus forward current of sample 1. I_{degra}=70mA,after t=65h.

By increasing the degradation current the annealing process accelerates. To investigate this characteristic and to show the influence of the housing on the LED, two non-encapsulated LED chips are degraded under a forward current of I_{degra}=120mA for several hours. Also the *I-V* characteristic is measured and analysed. Figure 5.3 depicts the measured luminous flux versus aging time. The measurement current is I_{meas}=10mA.

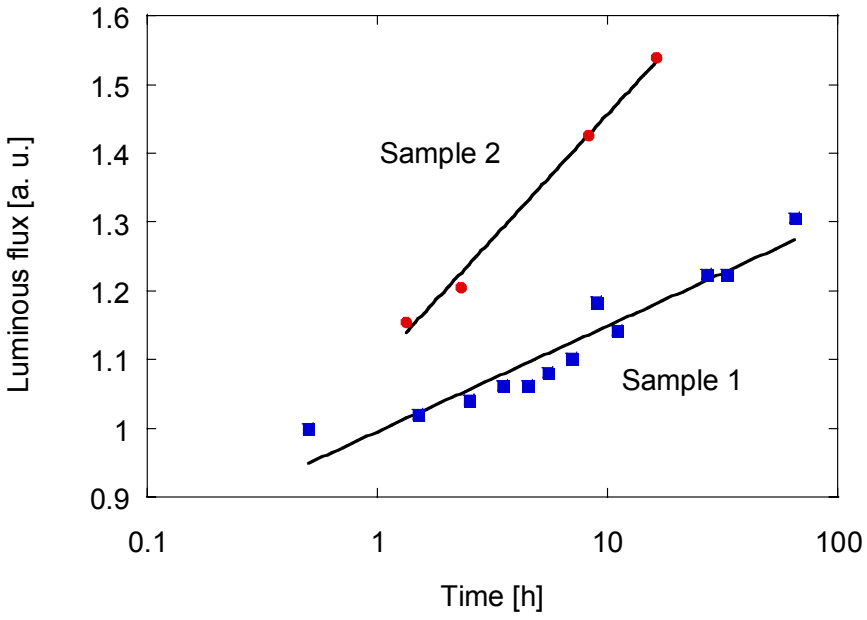

Figure 5.3: Sample 2, normalised luminous flux versus aging time at I_{degra}=120mA. The increase of luminous flux is 54% after t=16h.

An increase of the luminous flux of 54% is observed after an annealing time of t=16h (Fig. 5.3). In comparison to sample 1, the increase of the intensity is accelerated. We find an increase of the luminous flux of 50% for sample 1 at I_{meas}=10mA. This is the same value as for sample 2 within the experimental error.

To prove the annealing effect and the reduction of non-radiative recombination centres during the first hours of degradation, *I-V* curves in forward direction are investigated. Most diodes have unwanted parasitic parallel resistance. This bypass can be caused by defects in the crystal structure where non-radiative recombination occurs. At high voltages these defects are saturated and the current flow is dominated by radiative recombination in the depletion layer. Figure 5.4 depicts schematically the equivalent circuit diagram of a real diode with its parallel and serial parasitic resistances.

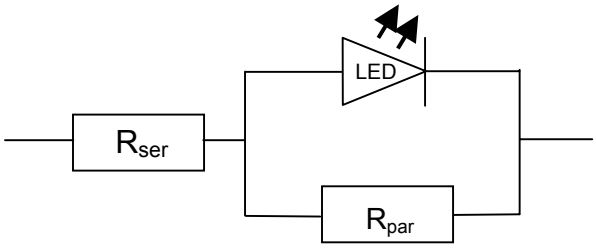

Figure 5.4: Equivalent circuit of a real diode with its serial and parallel resistance.

Therefore the *I-V* characteristic in the low voltage regime must be investigated. Reducing the defects in the crystal structure leads to an increase of the parallel resistance which increases the total resistance. Thus the current flow through the device is decreased [7]. This decrease in current flow is clearly shown in the *I-V* characteristic at sample 2. Figure 5.5 depicts the result of this measurement before annealing (red curve) and after 14hours of annealing time (blue curve) and after 40hours (green curve). The reduction of current flow at V=1.5V is 19% and marked with arrows. This result indicates a clear improvement of the electrical properties of the device by annealing.

The increased light output and the decrease of the parallel shunt resistance leads to the conclusion that the crystal structure is improving during the first hours of the degradation process.

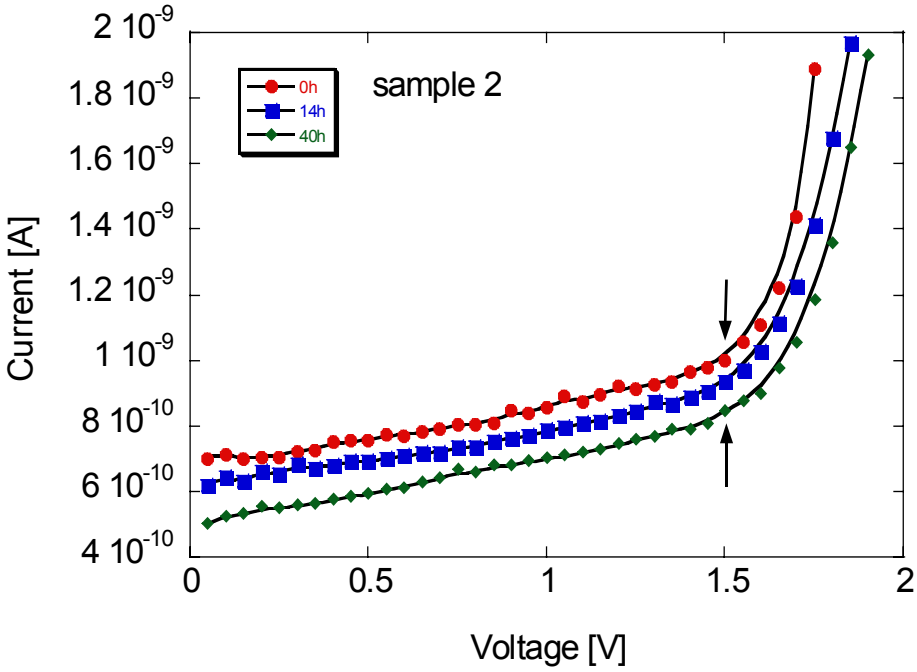

Figure 5.5: I-V characteristics of sample 2 before annealing and after 14h and 40h of annealing. The diode was treated by a forward current of I_{deagra}=120mA. A reduction of the parallel shunt resistance is clearly observable.

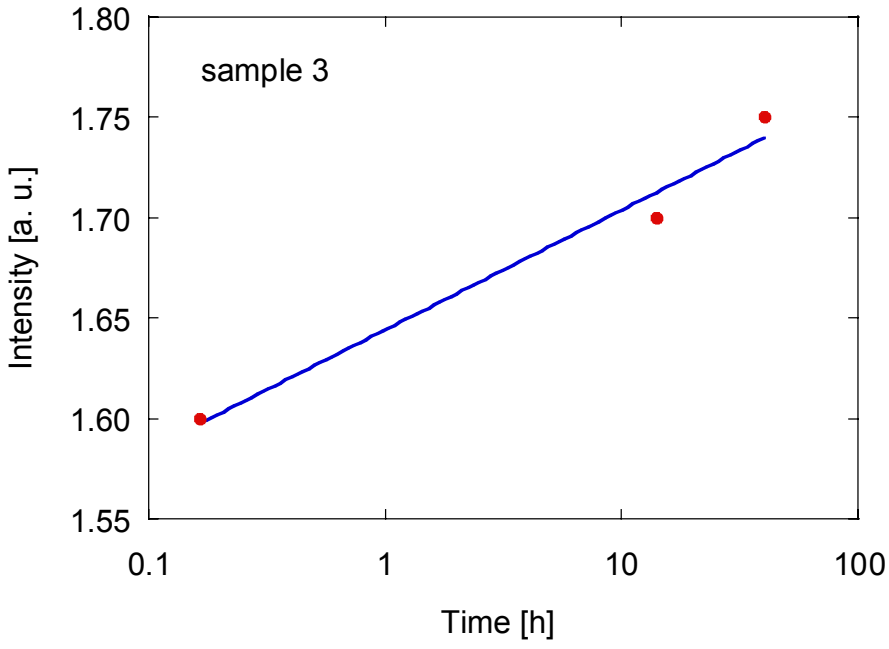

Figure 5.6: Intensity versus degradation time of sample 3 at I_{meas}=40mA.

The burn-in behaviour of sample 3, a non-encapsulated LED Chip, has also been investigated. The result is depicted in Fig. 5.6. In contrast to sample 2 the intensity is only increased by 10% at I_{meas}=40mA. This is the lowest value observed during these investigations. The reason for the large fluctuations in the positive degradation is unknown.

One reason could be a different lattice defect density due to different production parameters. Also the thermal treatment during gluing or soldering influences the annealing process.

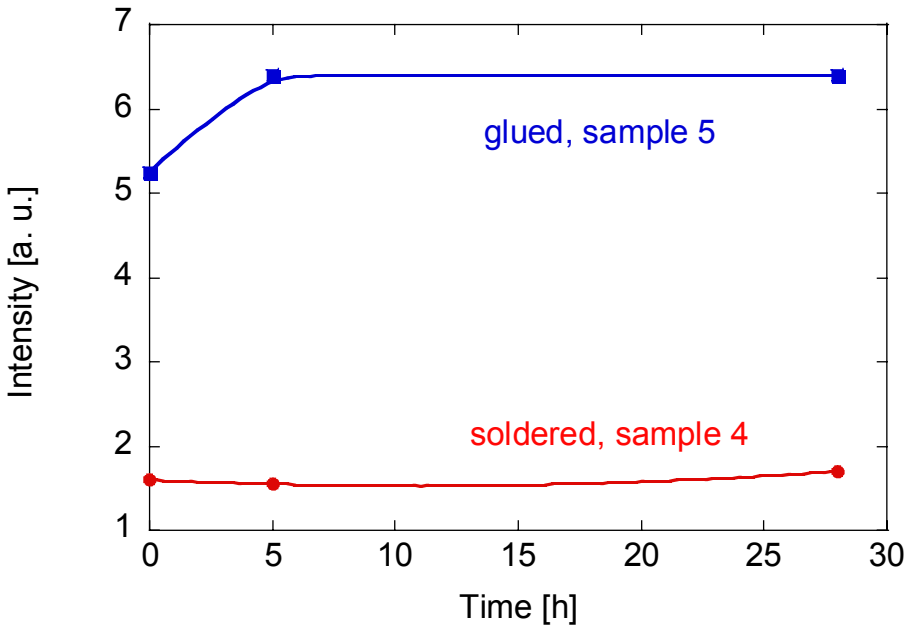

Figure 5.7: Intensity versus degradation time of PMMA encapsulated LEDs. Blue curve for glued/bonded sample 5, red curve for soldered sample 4 at I_{meas}=40mA.

Figure 5.7 depicts the intensity versus degradation time of sample 4 and 5. The blue curve is obtained from a sample which is glued with the n-contact to the frame. The p-contact is bonded. Details of the experimental set-up are described in chapter 6.1.1. The degradation current is I_{degra}=120mA, the measurement current is I_{meas}=40mA. An increase of the luminous flux is clearly observed during the first hours of degradation time. The intensity then saturates, the total increase of light output is about 21%.

The characteristic of the soldered LED is different and given by the red curve in Fig. 5.7. The degradation and measurement parameters are the same as with sample 5. The total luminous flux is a factor 3.3 lower in comparison to the bonded sample. Also no increase of light output during the first 25h of treatment is observed.

We conclude that treating the LED with a high forward current has a positive effect on the light output. This positive aging is based on the improvement of the crystal structure [25], [26] and has been demonstrated with LED chips as well as PMMA encapsulated LEDs. Also an improvement of the electrical characteristic has been demonstrated, the parallel shunt resistance has been reduced.

Soldered LEDs did not show positive aging during our investigations. We believe that the positive aging is effected by the thermal treatment during soldering.

5.3 Long term aging

Two LED chips are treated under a forward current of I_{degra}=120mA. From the first LED the total luminous flux at I_{meas1}=5mA, I_{meas2}=10mA, I_{meas3}=20mA, I_{meas4}=40mA and I_{meas5}=70mA is measured. Also the *I-V* characteristic versus degradation time is measured. This sample is called LZ-UL 2. The second sample is called LZ-EL 2 and the surface emission spectra at similar currents are measured during the degradation. Also the *I-V* characteristic is investigated. Both LEDs are non-encapsulated chips. The p-contact is realised by a tip probe. The tip remains on the contact during the degradation experiment. This avoids variations in the serial resistance. The n-contact is glued to a copper frame by using glue XCA 80210 described in chapter 4.2. This glue grants a perfect electrical and thermal conductivity from the semiconductor to the copper frame. The sample LZ-UL 2 is aged over a period of t=704h and sample LZ-UL 2 over a period of t=230h. First we investigate the *I-V* characteristics of these samples. Figure 5.8 depicts the forward current versus forward voltage characteristics over the degradation time of sample LZ-UL 2. The serial resistance increases clearly over the degradation time.

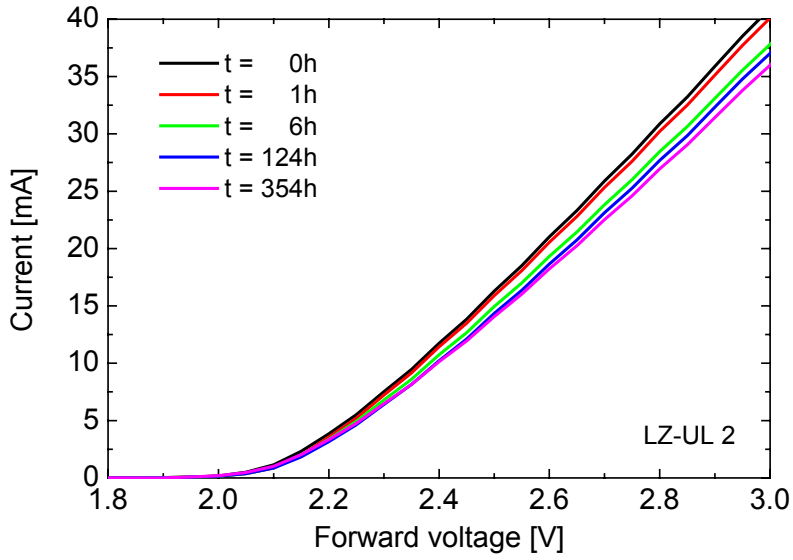

Figure 5.8: Current voltage characteristics of a LED at various degradation times. *The serial resistance increases with the degradation time.*

This characteristic is shown in Fig. 5.9 where the time is plotted in a logarithmic scale. The data are fitted by:

$$R_S(t) = R_0 \ln\left(\frac{t}{t_0}\right) \tag{5.1}$$

The parameters are calculated to R_0=0.27Ω and $t_0 = 1.38 \cdot 10^{-33}$ h

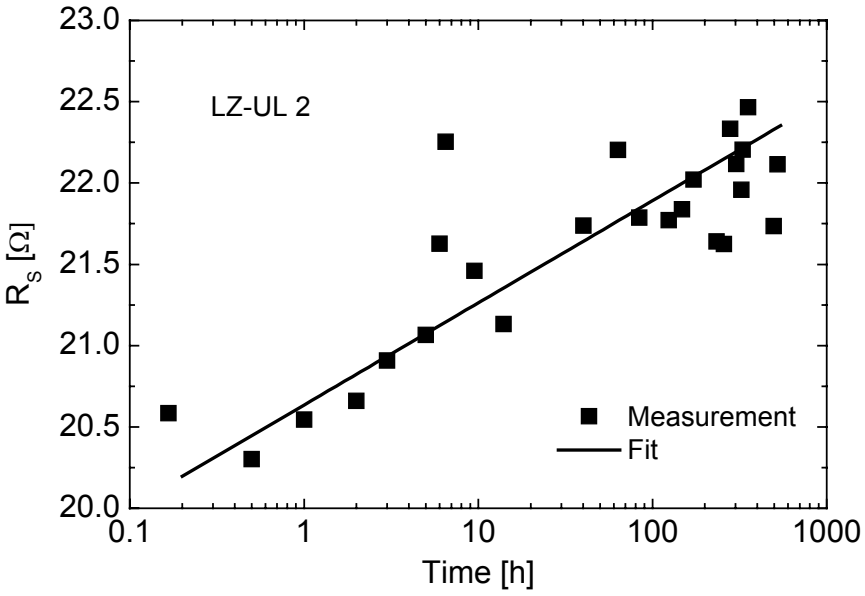

Figure 5.9: Serial resistance of sample LZ-UL 2 versus aging time. The black line is a logarithmic fit of the experimental data.

Also the total luminous flux of sample LZ-UL 2 is measured in an Ulbricht sphere. The measurement currents are I_{meas1}=5mA, I_{meas2}=10mA, I_{meas3}=20mA, I_{meas4}=40mA and I_{meas5}=70mA. The results are depicted in Fig. 5.10. The luminous flux is given in arbitrary units versus the degradation time. During the first few hours an increase of the luminous flux is observed as described in the previous paragraph. After t=120h the luminous flux starts to decrease and remains constant after t=380h. The increase of efficiency at the beginning of the treatment is an effect of thermal annealing. This effect of structural improvement by heating the semiconductor is well known and described for example in [25] and [26]. The effect seems to be exhausted after t=120h and degradation starts to reduce the efficiency. Details and modelling of the degradation will be given in chapter 7.

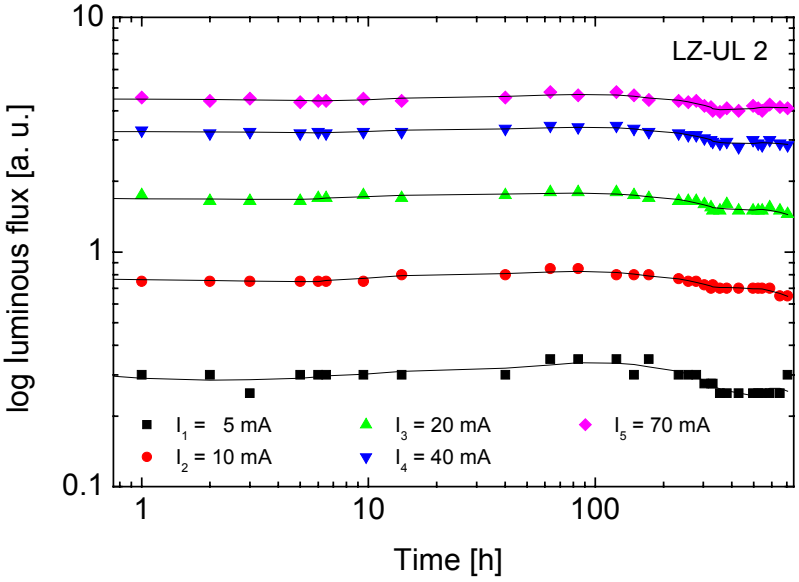

Figure 5.10: Luminous flux versus aging time measured at different currents. After t=120h the luminous flux starts to decrease.

Improvement in efficiency is observed for all measurement currents, but is more significant for low forward currents.

Figure 5.11 depicts the emission spectra of the non-degraded LED at different measurement currents. The intensity is plotted in a logarithmic scale versus the energy. By increasing the forward current the intensity increases and the peak energies E_1 and E_2 decrease. At I_{meas}=70mA the peaks E_1 and E_2 cannot be distinguished any longer. The peaks E_1 and E_2 result in a peak energy E_0. Figure 5.11 shows the emission after t=54h of aging at I_{degra}=120mA. By comparing the I_{meas}=70mA measurements from Fig. 5.11 and Fig. 5.12 one sees that the intensity is increased and the peak emission E_0 is shifted to higher energies. By fitting the emission with Eq. (2.13) the intensity and the energy of E_{max} can be calculated. For low currents E_{max} is equal to E_2. For high currents E_{max} is equal to E_0.

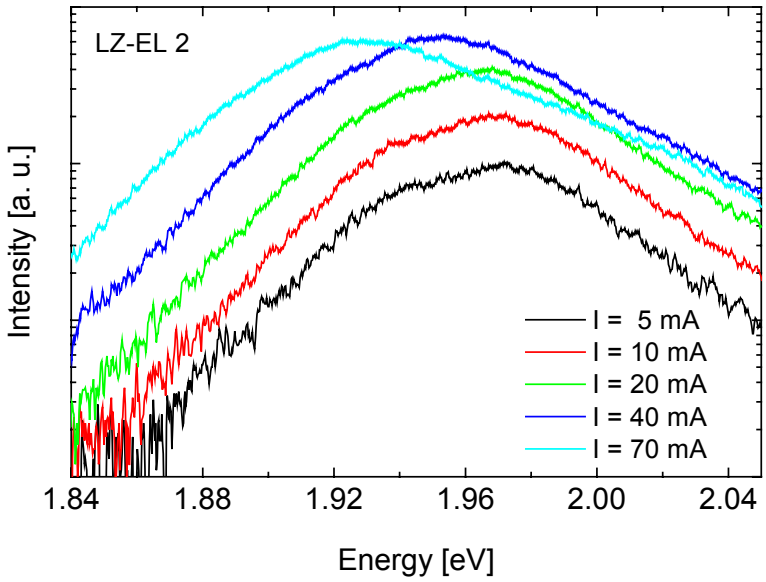

Figure 5.11: Emission spectra before degradation for various forward currents. The intensity increases by increasing the forward current thus shifting the peak to lower energies.

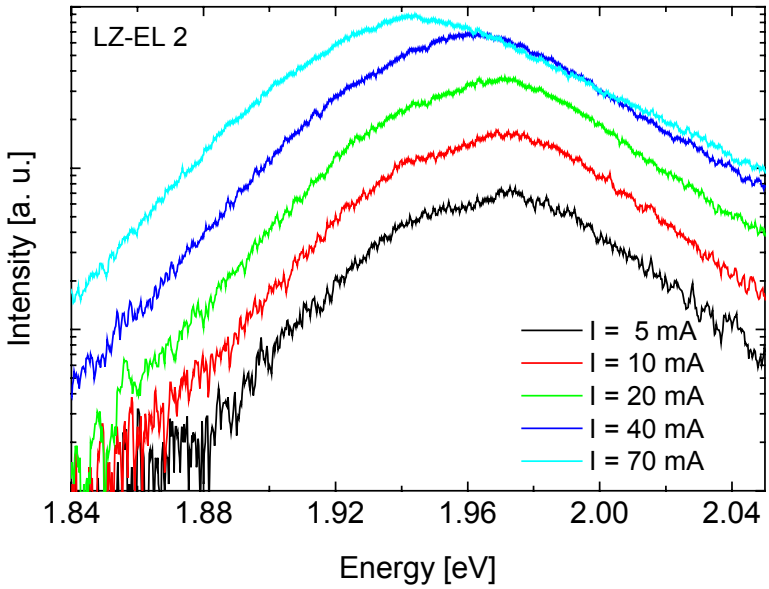

Figure 5.12: Emission after 54h of aging at I_{degra}=120mA.

Figure 5.13 depicts the increase of intensity as well as the increase of the peak energy for different forward currents versus aging time. The intensity is plotted in black, the peak energy in red.

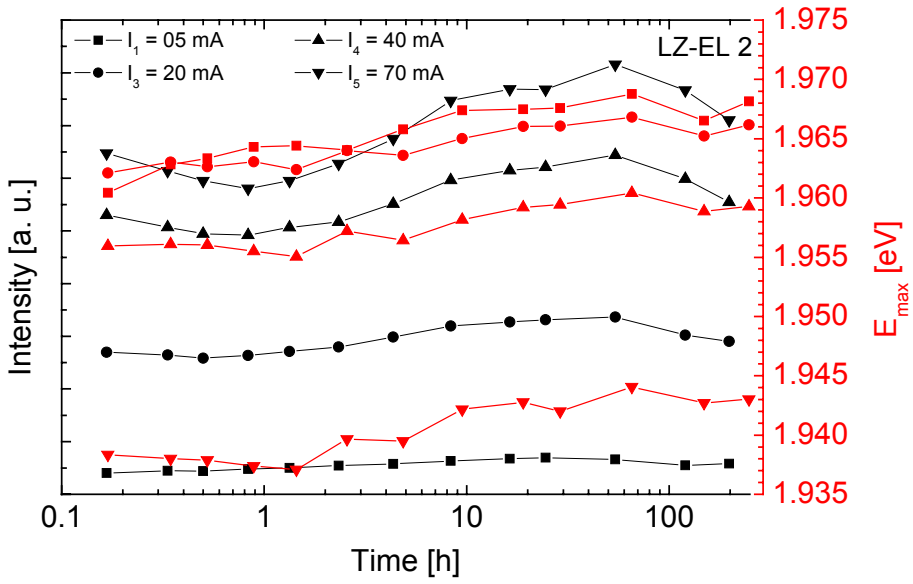

Figure 5.13: Maximum intensity (black dots) and energy (red dots) versus degradation time for different drive currents.

In this chapter we have described the change of the LED chip properties aged under high forward current. An increase of the serial resistance versus the degradation time is observed, which is attributed to degradation of the ohmic contact on top of the p-layer [27].

The luminous flux versus degradation time has been measured in an Ulbricht sphere. During the first hours of degradation an increase of luminous efficiency is observed which is attributed to an improvement of the crystal structure. The atomic motion is increased by higher device temperatures thus a self arrangement improves the lattice purity and reduces the dislocation density. The increase of the peak energy is also an annealing effect. By reducing the defect density the efficiency of the device is increased. Thus the temperature of the LED chip decreases during the annealing period. A decreasing device temperature leads to a blue shift in the emission. The maximal energy shift is measured to ΔE=10meV.

The decrease of luminous intensity can be explained by the generation of non-radiative recombination centres in the active layer.

6 Injection molding of LED clusters

6.1 General set-up and temperature measurements

A standard method to encapsulate LEDs is casting them in resin [28]. The LED chip is mounted in a reflector cup on a lead frame which in general is formed out of the cathode lead. The p-contact is normally bonded with a gold wire to the anode lead. The entire device is encased in epoxy which also serves as a lens. The resin hardens due to a chemical process. This process has some advantages. It is easy to handle and the temperature load during the hardening process is negligible. The development of non-shrinking epoxy resins avoids pressure pile-up at the devices. Limitations are the very high thermal resistance R_{th}>200 K/W, the limited temperature stability of epoxy resin T_{Epoxy}<120°C and therefore a limited input power of P_{In}<0.1W. Also there are limitations in forming the geometry of the housing. With respect to lightweight and miniaturization, especially in the automotive industry, external optical components to tailor the light beam should be avoided. Using external optical devices leads to an adjustment process where the optical device has to be adjusted against the light source. Also every optical unit has an interface which leads to an intensity reduction due to reflection. This means a direct encapsulation process which combines the housing and the optic element in one unit is necessary. Those processes are impossible with resin as an encapsulation material.

By contrast direct encapsulation of LEDs by an injection molding tool is a useful way to control the optical geometry to produce the required radiation pattern, whilst also protecting the semiconductor against environmental influences. To investigate the injection molding encapsulation process, an injection molding tool has been developed. It meets the following requirements: The frame which is described later in this chapter should be easily insertable in the tool. Is has been taken into account that in a future step of automation the frame should be replaced by an endless band of copper. The possibility to pre-encapsulate the LED chips with a small sphere at low pressure before creating the optic must be provided. To meet these requirements a split mold seems to be the best approach. The cavity insert is removable to

pre-encapsulate the LED chips in a first step for protection reasons. In a second step the optic is formed at high pressure with a different mold insert. All surfaces in the cavity of the tool are polished to obtain perfect optical surfaces. Figure 6.1 is a drawing of the set-up of the injection molding tool. Marked in red is the runner which is divided by four and leads to the individual LED chips. This is the approach to encapsulate each chip under low pressure with a small sphere. Further down it is shown that this pre-encapsulation process has no effect on the failure rate. Therefore it has only been performed in the early steps of the investigation. Figure 6.2 depicts the tool with the cavity which forms the parabolic shaped optics. The sprue is realised by a single channel located at one site allowing to fill the cavity at high pressure. High pressure, one should say high backpressure, is necessary to avoid shrinking of the module. Shrinking would lead to a deformation of the polymer and a less effective optic.

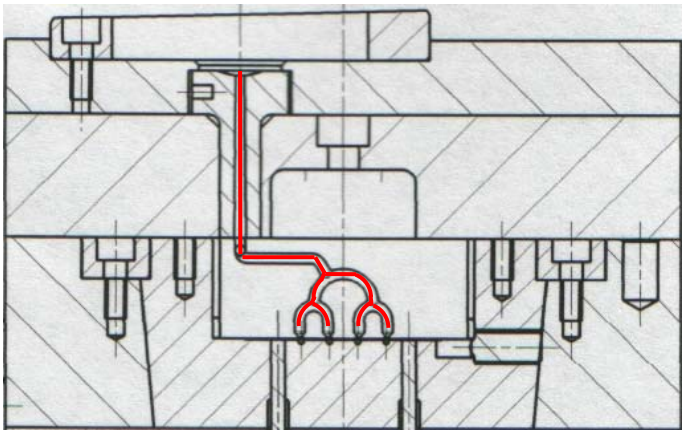

Figure 6.1: Drawing of the tool, set-up for "bubble in" the LED chips at low pressure. Source: Hella

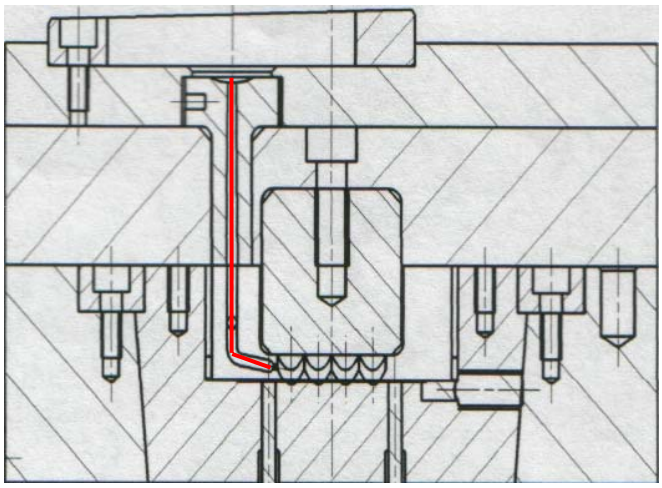

Figure 6.2: Drawing of the tool, set-up for optic production at high pressure. Source: Hella

For indirect encapsulation both steps (bubble in and optic creation) must be carried out. For direct encapsulation only the second step (Fig.6.2), is necessary. Our experiments have clearly shown that the two-step process has no advantages compared to direct encapsulation. Therefore after the first experiments, all investigated samples are encapsulated using the one-step method. Figure 6.3 is a view directly into the cavity of the tool. The slide bars form the parabolic optics, the frame is loaded from the top and a polished stamp close the cavity. During the closing process the slide bars shut under a certain angle and fix the copper frame. It acts as a gasket for the liquid polymer in this situation. This means there is a mold parting surface just between the two slide bars. The slide bars and the stamp is water-tempered to guarantee stable conditions.

Figure 6.3: Top view into the cavity of the injection molding tool. The slide bars are wide open to load the cavity with the frame. The investigations were performed on an Arburg A380 injection molding machine.

6.1.1 The Module (molded part)

The module consists of two parts. A copper web was chosen as a basis, it has been metalised with nickel and gold. The nickel layer acts as diffusion barrier and has a thickness of d=10 µm. Copper has a rather high diffusivity in semiconductor materials, therefore the nickel layer is necessary. To improve the ohmic contact between the web and the LED, a gold layer with a thickness of d=100nm has been deposited on the nickel layer. Both layers have been deposited in a galvanic bath. The LED chips are directly glued onto the gold.
Figure 6.4 shows the geometry of the web chosen for die/wire bonding. Four LEDs are placed on every frame.

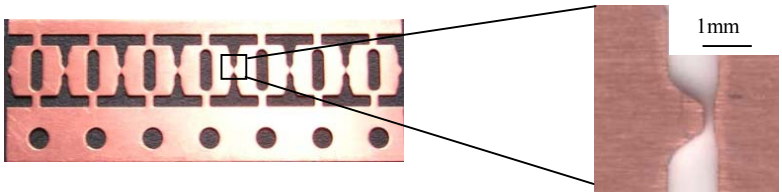

Figure 6.4: Copper web for die/wire bonding. Asymmetry of the electrode guarantees that the LED chips are in the focal point of the parabolic optic.

The LED chips are glued with their anode on the “nose”. This asymmetric set-up is necessary to place the LED chips in the focal point of the parabolic optic.
Figure 6.5 shows the geometry of the web chosen for die/die bonding.

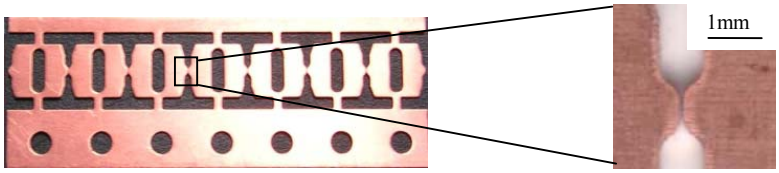

Figure 6.5: Copper web used for die/die bonding. Two symmetric noses with a gap of d=100µm. The chip is placed with its active layer over the gap.

For die/die bonding both sides of the chip are metalised. Then the chip is turned by 90° and placed over the gap of the symmetric noses. The active layer has to be over the gap to avoid a short circuit of the device.

Detailed description of the two different kinds of bonds which have been tested:
(a) Die/wire bonding (Fig. 6.6): The LED chip is glued with its anode to the frame (die bond) and the cathode is bonded with a gold wire, diameter d=25µm, to the frame (wire bond).

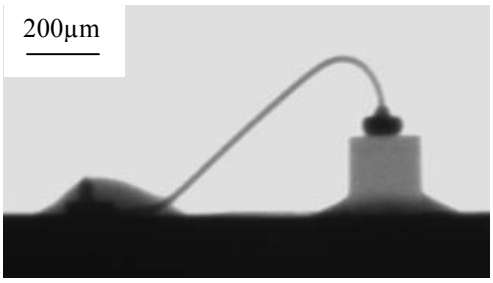

Figure 6.6: Frame with die/wire bonded AS AlInGaP LED chip (X-ray image).

(b) Die/die bonding (Fig. 6.7): Both sides of the chip (anode and cathode) are metallised. The chip is turned by 90° in comparison to (a). Both sides of the chip are soldered in an oven.
In Fig. 6.7 a vertical cut through the die/die bonded transparent substrate (TS) chip shows the principle of die/die bonding. Clearly visible is the LED chip and the two soldering points. The chip is well positioned and has good contact to the soldering material.

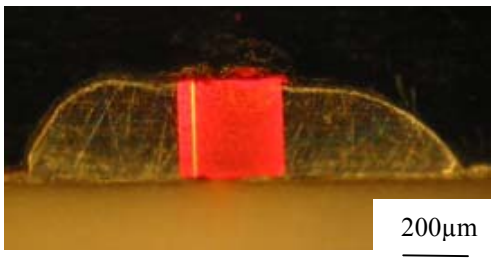

Figure 6.7: Die/die bonded TS LED chip.

The yellow strip is the active layer which is located near the p-contact (left side). Typically for TS chips is the red-shining substrate. With this bonding method no light could escape through the contact region.

6.1.2 Optics:

The system consists of four contiguous, parabolic shaped total reflection optics. The focal length is f=1,1mm. Figure 6.8 shows the principle of total reflection in one parabolic optic.

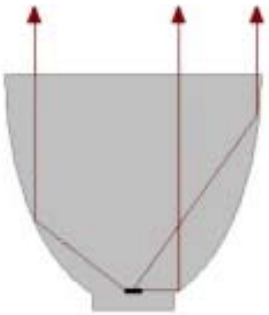

Figure 6.8: Total reflection optic (principle).

The light beam is tailored to a narrow beam with a spread angle of α=10°. Detailed radiation patterns are given in chapter 6.3. The material is PMMA 7N which is amorphous. The refraction index is n=1.49, the glass transition temperature is T=106°C [29]. This material is commonly used for optical parts such as lenses, but also for car tail-lights. Therefore it is a proven material for this application.

In Fig. 6.9 the complete module in two different viewing angles is illustrated.

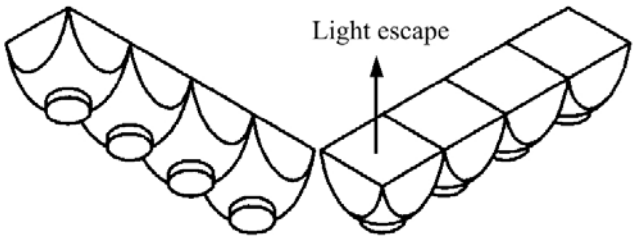

Figure 6.9: LED module in two different viewing angles.

Figure 6.10 shows the final LED module consisting of the frame and the four parabola-shaped optics with the semiconductor light sources inside. The length of the device is *l*=32mm, the height *h*=9mm, and the depth *d*=8mm.

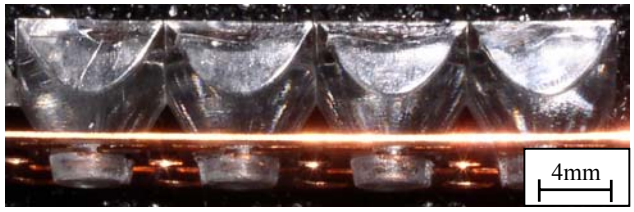

Figure 6.10: Optic module.

6.1.3 Temperature measurements

To investigate the thermal load of the semiconductor during the encapsulation process the temperature of the polymer melt must be measured at the LED location. Therefore a temperature sensor which can replace the LED is necessary. Standard temperature sensors for injection molding are not suitable for this application. They are bulky and compared to the cavity need a rather big feed through which could not be realized in the tool. They have a relatively high heat capacity and therefore a time constant which exceeds the time constant of semiconductor temperature sensors. Semiconductor temperature sensors are widely used for different applications and temperature ranges. This could be an alternative due to the small sensor size, the small heat capacity and the easy availability. In the following we show that the LED chip itself could be used as a temperature sensor and that it fulfills all the requirements. The LED itself can be used as a temperature sensor due to the fact that the forward voltage of a pn-junction is a function of temperature at a constant current. According to [7], the temperature depending voltage can be expressed by:

$$V(T) = \frac{kT}{e} \ln \frac{I}{I_S} + \frac{E_g(T)}{e} \tag{6.1}$$

where $V(T)$ is the forward voltage, k the Boltzmann constant, T the temperature, e the elementary charge, I the operation current, I_s the saturation current and $E_g(T)$ the energy gap.

The temperature dependence of the Fermi level is described by the first term on the right-hand side. This level moves towards the middle of the gap with increasing temperature. The energy gap $E_g(T)$ is the distance between the conduction band and the valence band. Hence, increasing temperature results in a smaller gap and therefore leads to a lower forward voltage. According to [30], the energy gap can be expressed by Eq. (6.2). The parameters α and β depend on the particular semiconductor material.

$$E_g(T) = E_{g,0} - \frac{\alpha T^2}{T + \beta} \tag{6.2}$$

where $E_{g,0}$ is the energy gap at 0K and α and β are the Varshni parameters [28]
Figure 6.11 illustrates the energy gap E_G of GaP calculated with Eq. (6.2).

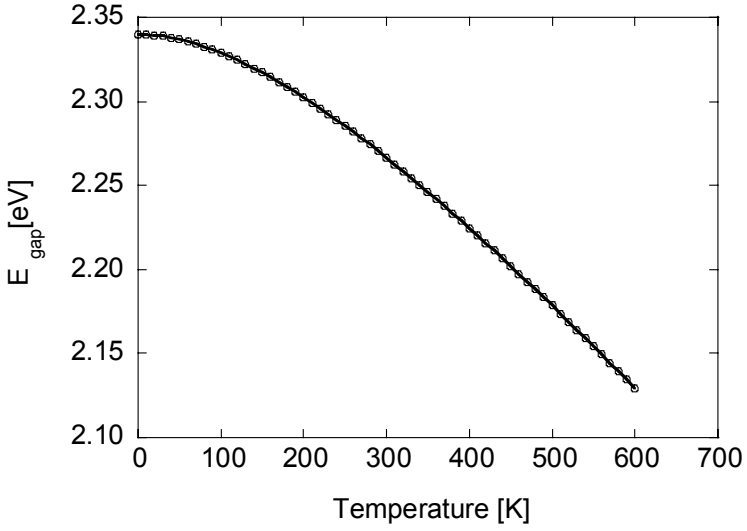

Figure 6.11: Band gap versus temperature of GaP.

Polymer melts are typically processed in a range between 400K to 650K.

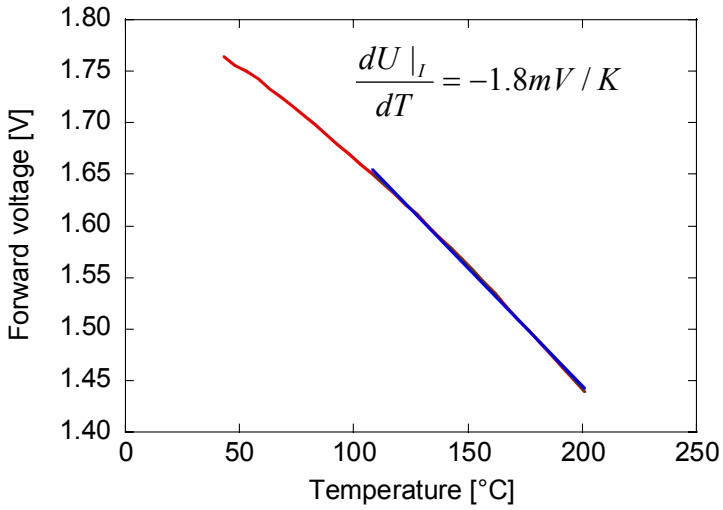

Figure 6.12: Forward voltage versus temperature at I=1mA for AlInGaP LEDs.

Figure 6.12 shows the forward voltage versus temperature characteristic of the AlInGaP LEDs used in the current investigations, the drive current is I=1mA. The slope of the linear fit in Fig.6.12 is dV/dT=-1.8 mV/K.

To ensure the accuracy of the measurement, the influence of thermal load on the calibration curve has been investigated. For this reason, five samples (Temp. 1-5) have been annealed in an oil bath at 205°C for different durations (1 to 5 minutes). The subsequent measurements of the temperature sensitivity depicted in Fig. 6.13, do not show much difference between the samples which emphasizes the suitability of LED chips for temperature measurements.

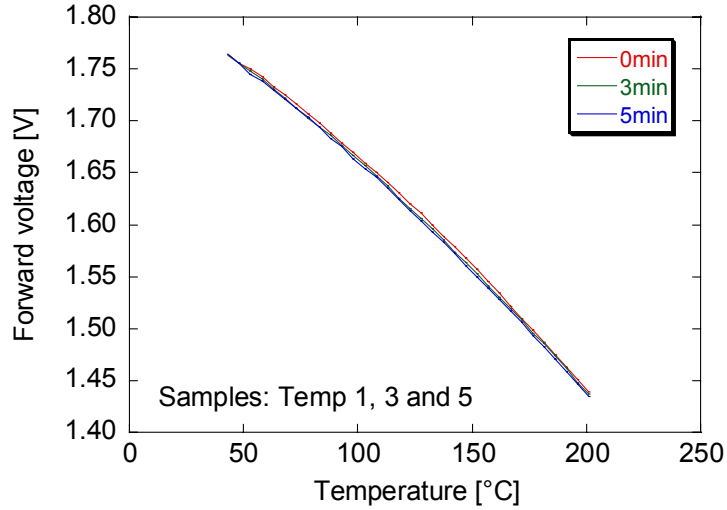

Figure 6.13: Forward voltage versus temperature of three different LEDs degraded at 0min, 3min and 5min at T=205°C.

To summarize, the LED chip temperature sensor is based on the voltage variation inside a semiconductor caused by the temperature change during direct encapsulation. Due to the low heat capacity of the device, the melt temperature is almost unaffected and a fast response is achieved. This method enables the user to determine the thermal load of directly encapsulated electrical devices and thereby to estimate the thermal degradation of semiconductors. Furthermore, it could also be possible to measure the temperature distribution within the molded part using multiple probes.

Figure 6.14 illustrates that the "LED temperature sensor" is placed into the second chamber. To ensure the electrical supply of the diode, a plug connection has been mounted into the first cavity on the right side. Beside the mentioned LED chips conventional PT 100 resistors were used to investigate the temperature variation in the tool.

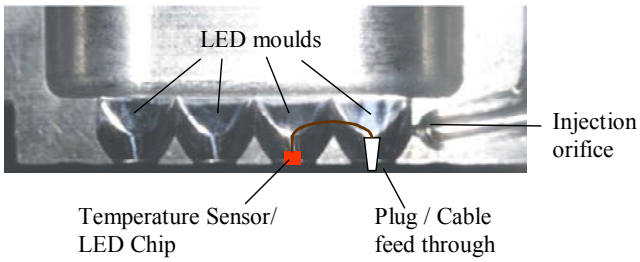

Figure 6.14: LED and cable feed through arrangement in the cavity of the injection molding tool.

Experimental Results:

Using the set-up described above, in-situ temperature measurements during the injection molding process have been performed.
The probes were supplied with constant current and the voltage variation caused by the temperature changes during the injection and cooling process has been recorded. By means of the calibration shown in Fig 6.12, the fluctuation of voltage is transformed into a temperature curve.
In Fig. 6.15 a typical temperature measurement of the LED chip during the PMMA encapsulation process is shown.

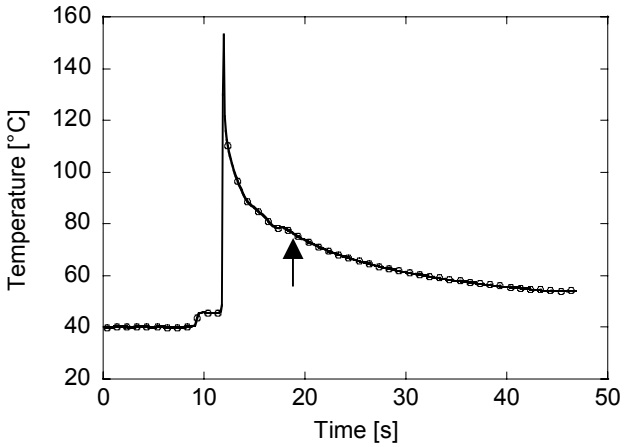

Figure 6.15: Temperature versus time of the LED chip in the cavity of the injection molding tool during the encapsulation process. The arrow marks the temperature increase at the glass transition.

The water-cooled injection molding tool is kept at T=50°C. This results in a starting temperature of T=40°C as the probe is mounted in the open, moving half of the mold. At t=9.1s the tool is closed and the temperature in the cavity increases due to the tool temperature. At t=11.8s the polymer melt reaches the probe and the temperature rises to a peak of 153°C. Then the temperature decreases, the melt solidifies and the sample is ejected at t=47s. All PMMA samples containing the LED probe show a small peak (arrow) at a temperature of about T=80°C. PMMA has a strong decay of its heat capacity during the cooling process at the glass transition temperature. Thus, intrinsic energy is transformed into heat during the glass transition process. This characteristic leads to a temperature increase which has been observed during our investigations. Assuming a decrease in the heat capacity of $\Delta C_p = 0.2 J / g \cdot K$, the temperature increases by ΔT=42°C. Due to the inhomogenous glass transition in the module we observe a constant temperature instead of a temperature increase. The results of the PT 100 and the LED probe are compared in Fig. 6.16. The different starting temperatures are a result of their mounting position: While the LED is glued onto the copper frame, the PT 100 was mounted by a small rod to the cavity of the molding tool. The diagram shows a considerable time delay for the PT 100 compared to the LED probe.

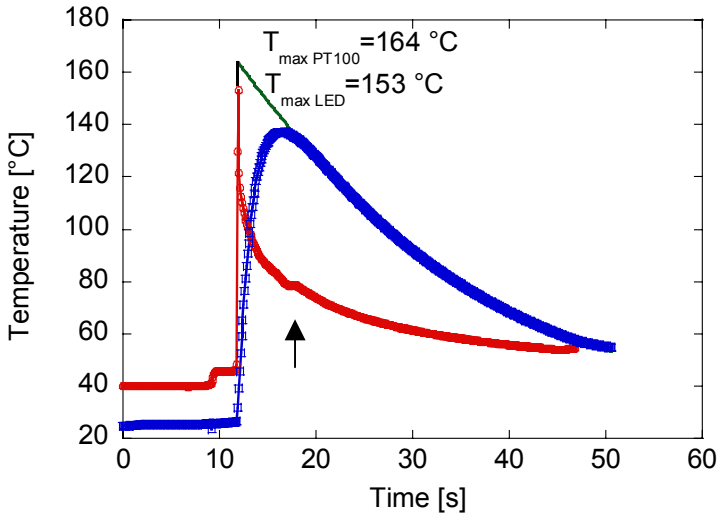

Figure 6.16: Time delay of the PT100 temperature sensor in comparison to the LED chip sensor.

This can be explained by the low specific heat capacity of the LED chip, which is only c_v=0,31J/gK. Nevertheless, the maximum temperature can also be estimated by using the PT100: Extrapolating the slope of the curve with a linear function and determining the point of intersection with a vertical line at t=11.5s results in a temperature of T=164°C, while the maximum temperature measured by the LED is T=153°C.

6.1.4 Simulation of the temperature distribution in the injection molding tool

To verify the temperature measurements presented above, a simulation of the temperature distribution based on the finite element method (FEM) has been carried out. Therefore the geometry of the molded part is implemented in the Moldex 3D software, as well as all other parameters from the Arburg 380 injection molding machine. Figure 6.17 depicts the temperature distribution in the module just after filling the cavity of the injection molding tool. The temperature scale in false colour ranges from T=32°C (blue) to T=250°C (red). The core of the module reaches T=250°C except the upper left corner, where the maximum temperature is approximately T=200°C. This is an indication, that the thermal load of the LED chips could by reduced by modifying the position of the injection orifice. The surfaces of the module are immediately cooled down to the temperature of the injection molding tool due to its large heat capacity. It is interesting that the LED chip in the right optic is treated with a higher thermal load as the other three. The temperature gradient from the shell to the core is higher in this region. Therefore hotter liquid polymer reaches the LED chip. The LED

chip which behaves (as described above) as a temperature sensor is marked with a black square. A virtual sensor is placed in the simulation as close as possible to the real position of the temperature sensor.

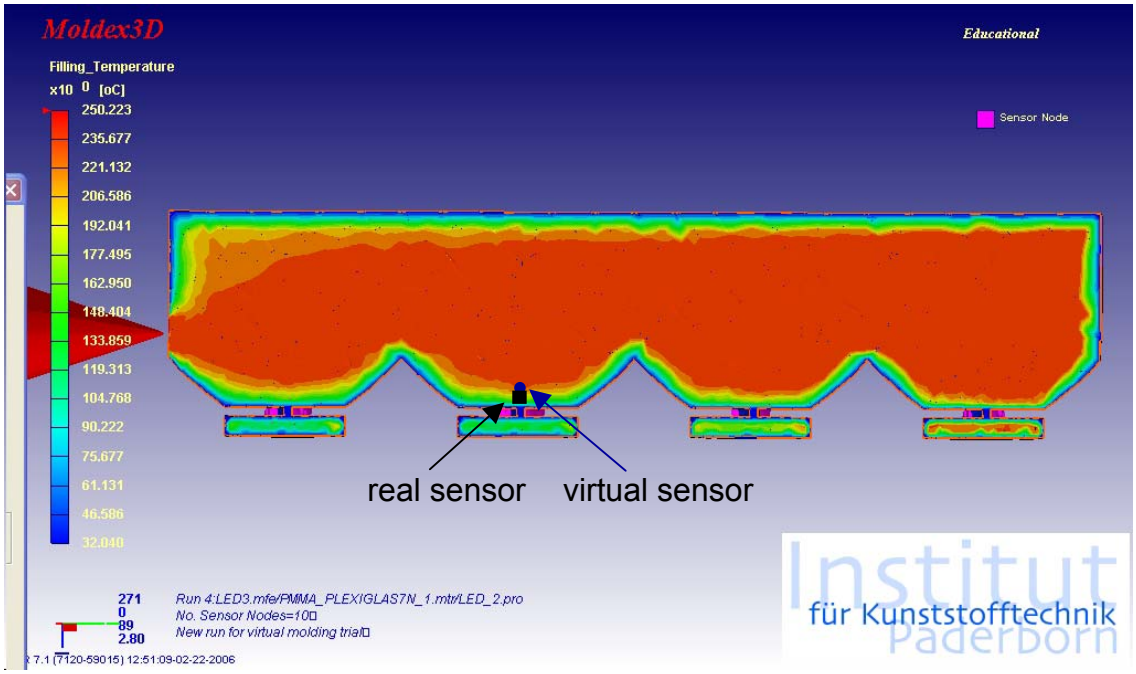

Figure 6.17: Temperature distribution in the LED module just after filling the cavity of the tool with liquid PMMA.

Only at the position of the knots of the finite element net such sensors could be positioned. Therefore the virtual sensor, which is marked with a blue circle, is directly above the real sensor position. From the simulation the temperature of the LED chip can be determined to T=150-175°C. This result is in perfect agreement with our measurement depicted in Fig. 6.16. To estimate the duration of the thermal load, a time-dependent temperature measurement at the point of the virtual sensor is simulated. The result is shown in Fig. 6.18. The temperature starts at T=50°C which is the cooling temperature of the molding tool. At t=0s the liquid polymer reaches the sensor and the temperature rises immediately to T=240°C. The temperature decreases fast and after t=2s it is below T=100°C. After t=9s the temperature has dropped to T= 60°C and at this point the module is removed from the tool. The higher peak temperature of the simulation is due to the fact described above that the virtual temperature sensor is not at exactly the same position as the real one. The shift of the virtual sensor to the inner core leads to an increased temperature.

Summarizing the experimental and theoretical results, the thermal load is defined by a peak temperature of about T=170°C and a subsequent fast decrease of the temperature. Ten seconds

after the peak, the temperature has dropped to T=75°C (experiment) or below T=60°C (simulation). The thermal load is in the range of a standard gluing process used to glue the LED chip to the board. In Ref. [14] the maximal thermal load for the LED chip is given by a maximal temperature of $T = 235°C \pm 5°C$ and a duration of $t = 2.5s \pm 0.5s$. Our result shows that the thermal load during the encapsulation process is within these limits.
Thus, in comparison to a soldering process the thermal load during this encapsulation process is negligible.

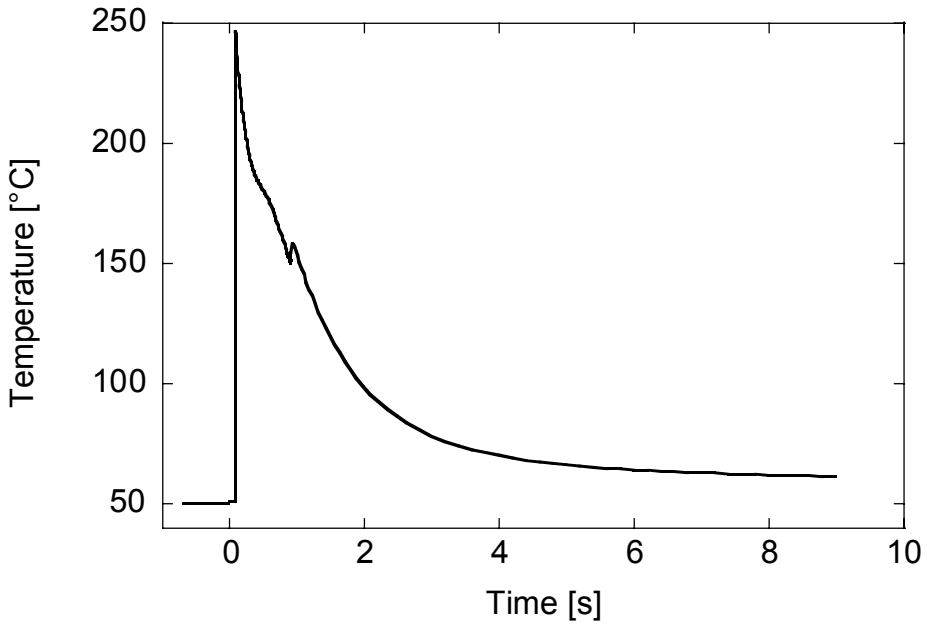

Figure 6.18: Simulated temperature versus time at the virtual temperature sensor which is near the real LED device.

Also, the temperature simulation shows a small temperature increase at t=0.8s which is attributed to the glass transition.

6.2 Influence of injection molding on the LED performance

In this chapter the influence of the injection molding process on the LED chips is investigated. Before encapsulation the *I-V* characteristics and the luminous flux at different drive currents are measured. Additionally the emission spectra at I_1=5mA, I_2=10mA, I_3=20mA and I_4=40mA are recorded. After the encapsulation process the samples are measured again and the results are compared. The polarization of the emitted light is also measured after the encapsulation process in order to find polarization effects caused by strained PMMA. The electroluminescence set-up described in chapter 4 is used as a detector. A polarization filter is adapted into the light path and the polarisation angle is measured in relation to the axis of symmetry of the module. Figure 6.19 depicts the set-up schematically.

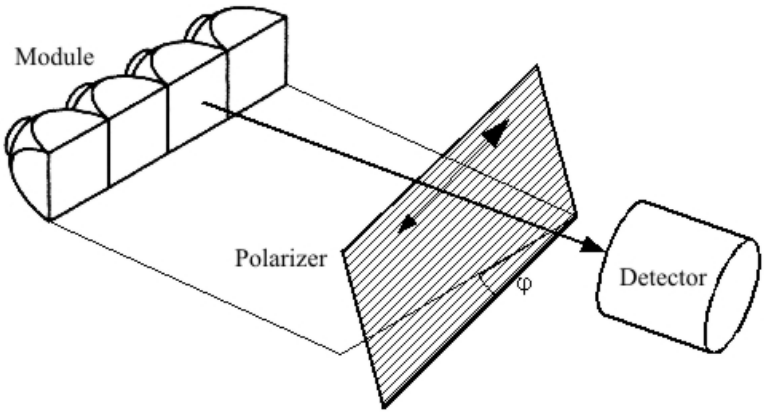

Figure 6.19: Experimental set-up to investigate the polarisation of the emitted light after the encapsulation process.

6.2.1 Results and discussion

The current-voltage characteristic of a typical sample is depicted in Fig. 6.20. The current is plotted in an linear scale. At low voltages an exponential increase of the current with increasing voltage is observed. At *V*=1.9V the device starts to behave like an ohmic contact. Up to *V*=1.9V no difference before and after encapsulation is observed. After the encapsulation process the current is increased in the regime of larger forward voltages. This is clearly depicted in Fig. 6.20 A. For *V*>2.1V the characteristic is linear and a decreased serial resistant after the encapsulation process is observe. The serial resistant after encapsulation

decreases by R=8.5Ω in comparison to the chip. The decrease of the serial resistance is caused by a higher device temperature during operation, after encapsulation. Before encapsulation, air flows around the chip and it is cooled by convection. After encapsulation cooling by convection is impeded. Using the temperature calibration in Fig. 6.12 we find an increase of the junction temperature of the encapsulated chip of about 15°C.

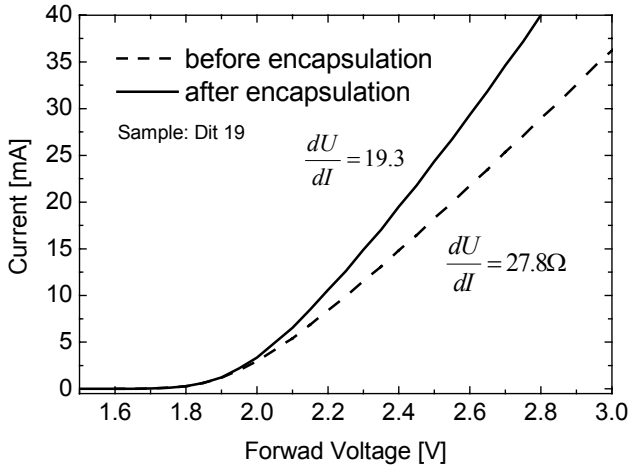

Figure 6.20: Current-voltage characteristics before (dashed line) and after (full line) the encapsulation process.

Additionally, the luminous flux for different drive currents has been measured in an Ulbricht sphere. Results are shown in Fig. 6.21. The luminous flux is plotted versus the drive current in a range from 0mA<I<45mA.

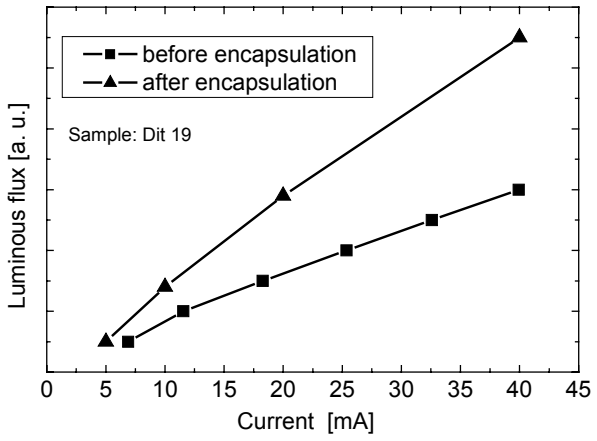

Figure 6.21: Luminous flux as function of the drive current. Squares before encapsulation, triangles after the injection molding process.

The total luminous flux at I_{meas}=45mA is 1.8 times higher compared to the non-encapsulated chip. As shown in chapter 2.5 the external quantum efficiency can be increased by encapsulation. If the refractive index of the encapsulation material is between that of air and the semiconductor material (GaP), the angle of total reflection increases and losses at the surfaces can decrease. The PMMA used in these investigations has an index of refraction of n_{PMMA}=1.49. Using Eq. (2.17) the reflectivity at the surface is calculated to:

$$R_{GaP-PMMA} \approx 11.5\%$$

$$R_{GaP-Air} \approx 3.9\%$$

The transmission from the semiconductor through the PMMA to air is then:

$$T_{GaP-PMMA-Air} = (1 - R_{GaP-PMMA})(1 - R_{PMMA-Air}) \approx 85.1\%$$

The absorption in the material is neglected.
Thus the external quantum efficiency $\eta_{ext}^{GaP-PMMA-Air}$ of the system is 10.7%

To calculate the theoretical improvement of the external quantum efficiency, the ratio of external quantum efficiency from GaP to air to the external quantum efficiency from GaP-PMMA-air must be calculated:

$$\frac{\Phi_{after}}{\Phi_{before}} = \frac{\eta_{ext}^{GaP-PMMA-Air}}{\eta_{ext}^{GaP-Air}} = \frac{T_{GaP-PMMA-Air}}{T_{GaP-Air}} \approx 1.14 \qquad (6.3)$$

Experimentally this factor has been determined to 1.8. In the calculation above the geometry of the PMMA optic is neglected. Therefore a lower theoretical value can be expected. Before encapsulation the angle of total reflection at the surface GaP-air is $\beta_G^{GaP-Air} = 19.3°$. After encapsulation the total reflection is:

$$\beta_G^{GaP-PMMA} = 29.6°$$

$$\beta_G^{PMMA-Air} = 41.8°$$

If the geometry is not changed, the angle of total reflection for the system GaP-PMMA-air will remain the same as for the GaP-air system. But in our investigations the geometry does

not remain constant. Therefore the experimentally obtained value is greater than the theoretical one.

Figure 6.22 depicts the emission spectra before and after the encapsulation process for two different drive currents. The intensities are normalized for easy comparability. Also included is the FWHM for I_{meas}=40mA. As explained in chapter 4.6.6 the peak energy of the emission shifts to the red spectral range by increasing the forward current. A peak energy shift due to the encapsulation process could not be observed, but the FWHM increases from ΔE=58 meV before to ΔE=67 meV after the encapsulation process.

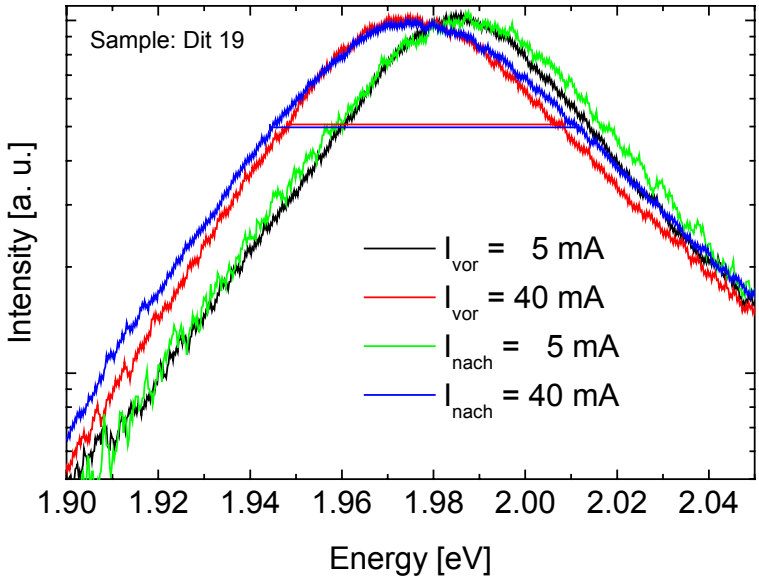

Figure 6.22: Emission spectra of a typical LED before and after the encapsulation process at different drive currents. The FWHM increases after the encapsulation process.

Figure 6.23 B depicts the FWHM as a function of the forward current. The FWHM of the LED emission increases with higher forward current. Additionally the FWHM at a constant current is larger after the encapsulation process. This is also a temperature-related behaviour. Because of the absence of convection the encapsulated LED chip has a higher temperature. As described in [7] the FWHM of the emission spectra broadens with increasing temperature. This is due to a temperature-related distribution of carriers in the conduction and valence band.

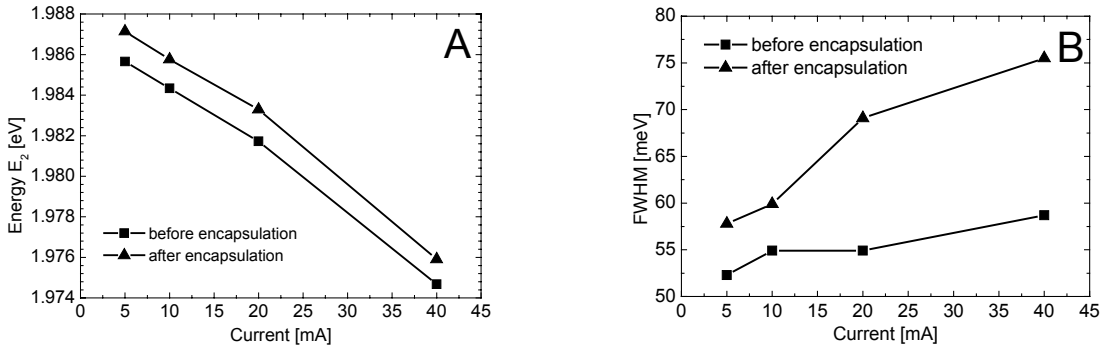

Figure 6.23: A) depicts the decrease of the emission energy E_2 versus the drive current. B) shows the peak broadening after the encapsulation process.

Figure 6.23 A depicts the decrease of the emission energy E_2 versus the drive current. As expected, the emission energy decreases with higher forward current because of the device heating. Not fully understood is the on average ΔE=1.425meV higher emission energy after the encapsulation process. In chapter 3 it is shown that the maximum difference from the emission along the z-axis to the emission from the top surface is ΔE=37meV. The parabolic optic directs the edge-emitted light parallel to the surface emitted light (chapter 6.1.2). Therefore the change of ΔE=1.425meV in the peak emission could be caused be a different light composition. Composition in this case means the ratio from "edge" light to "surface" light launched into the monochromator is influenced by the optic.

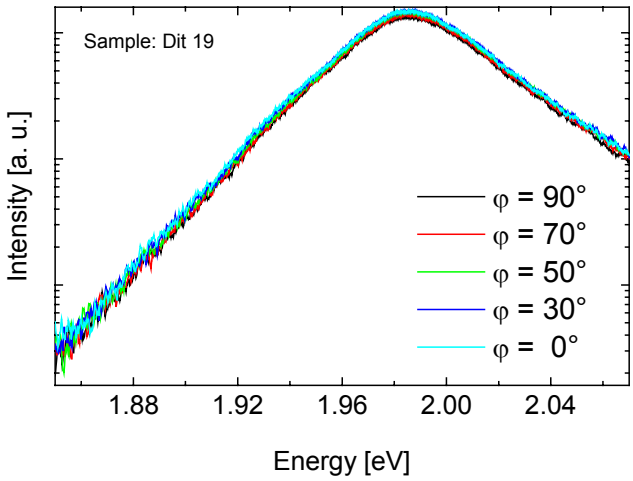

Figure 6.24: Spectra at different polarization angles relative to the axis of symmetry of the module.

After encapsulation the polarisation angle φ of the emission is measured. The maximum intensity of the emission spectra depicted in Fig. 6.24 is plotted versus the polarisation angle φ of the polarisation filter. Figure 6.25 shows the results. The data are fitted by Eq. (6.4)

$$I(\varphi) = A_0 \cos(\varphi - \varphi_0) + I_0 \tag{6.4}$$

The intensity $I(\varphi)$ only varies about ΔA_0=0.16%. A slight polarisation with an orientation of φ_0=18.9° is observable.

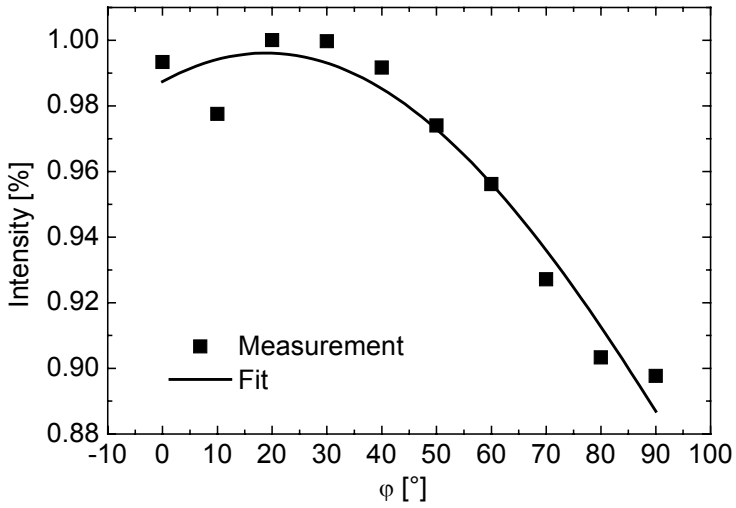

Figure 6.25: Light intensity of an encapsulated LED versus angle φ of the polarisation filter.

According to [31] strained PMMA has a strong polarisation effect to light. Thus we believe that the slight polarisation effect depicted in Fig. 6.25 is an indication for a strained PMMA encapsulation.

6.3 Radiation pattern of the PMMA optic

To demonstrate the focusing effect of the parabolic PMMA optic the radiation pattern of the chip and of the complete module is measured with a far field goniometer. Figure 6.26 shows the radiation pattern of the non-encapsulated LED chip as supplied by the manufacturer. The light source is mounted in the centre of the coordinate system. The active layer is perpendicular to the 90° direction, the n-contact is not transparent and points to the 270° direction. Therefore no light emission could be observed at angles between 180° and 360°. The goniometer measures the light intensity per solid angle and creates a vector where the direction of the vector corresponds to the direction of the light emission. The length of the vector corresponds to the intensity. As we clearly see, the main part of the light is emitted at angles between 0° and 180°. The light intensity emitted in the 90° direction, is about half the maximum intensity, noticeable are the two bulky edges which correspond to the edges of the square-shaped semiconductor. This means that in a 3D view there are four of these bulky edges which correspond to the four edges of the LED chip. The total luminous flux at an electrical current of I=20mA is Φ=0.83lm. The emission spectrum is typically for edge-emitting diodes.

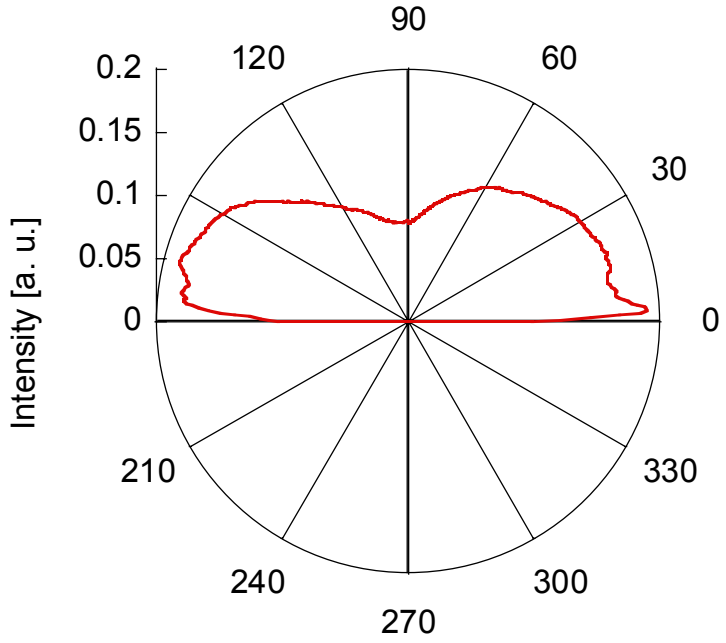

Figure 6.26: Radiation pattern of a LED chip without encapsulation.

Figure 6.27 shows the radiation pattern of the LED with the parabolic-shaped total reflection optic. The emission is focused straight forward in a narrow beam with a beam spread of α=10°. Due to the focusing effect of the parabolic optic, the intensity in the 180° direction clearly increased. A total luminous flux of Φ=1.11lm has been determined.

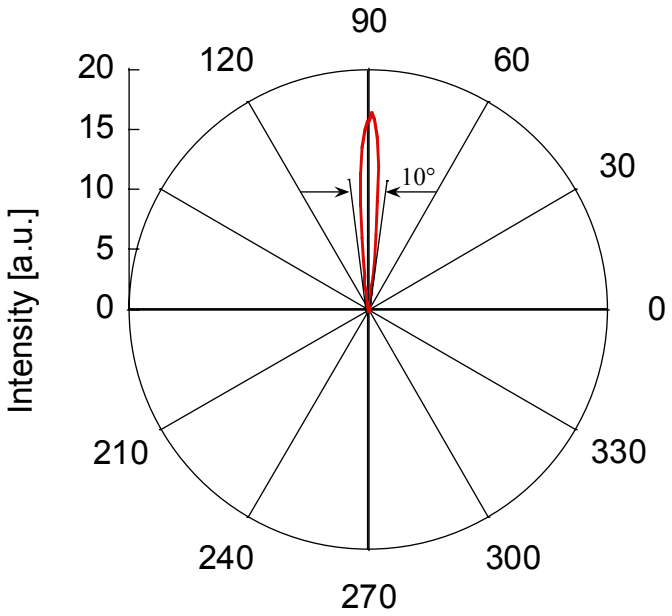

Figure 6.27: Radiation pattern of a LED encapsulated in the parabolic optic.

7 Diffusion model for LED degradation

In this chapter we analyze the aging characteristics of PMMA encapsulated LEDs. The reduction of the electroluminescence efficiency η_t during aging time t by keeping the junction at temperature T_j is measured. The junction temperature is caused by a forward current I_{degra}. The reduction of the efficiency is attributed to the formation of non-radiative recombination centres in the active layer. We show that this non-radiative recombination centres are Mg atoms which diffuse from the p-type layer into the active layer.

We assume that the Mg diffusion can only occur when the repelling p-n junction potential is reduced by the forward voltage. In the case of device heating by forward current this is taken for granted.

7.1 The dependence of electroluminescence on trap concentration

In this paragraph we calculate a relationship between the concentration of non-radiative trapping centres $N_{n,d}$ (in the active layer of the LED) and the electroluminescence efficiency $r(t)$.

An increase of the non-radiative trap concentration during degradation decreases the lifetime of the electrons. This reduces the probability that a given electron will recombine radiatively. It has been shown in [32] that the external electroluminescent efficiency η of a non-degraded device can be expressed as:

$$\eta = \eta_B \eta_{inj} R f(I_e) \eta_{oc} \qquad (7.1)$$

where η_B is the internal quantum efficiency, η_{inj} is the current injection efficiency defined as the ratio of the electron and hole diffusion current density (I_e+I_h) to the total current density I_t, R is the ratio of I_e to (I_e+I_h), $f(I_e)$ accounts for the decay in quantum efficiency due to

saturation of the radiative recombination mechanism, and η_{oc} is the external optical out-coupling efficiency of the device to the environment. Hence η can be written as:

$$\eta = \eta_B f(I_e)(I_e / I_t)\eta_{oc}. \tag{7.2}$$

According to the kinetics of photoluminescence [33], [34] η_B is related to the minority-carrier lifetime τ_e and to the lifetime for electrons captured by nonradiative traps τ_n:

$$\eta_B = \frac{\alpha\tau_n}{\tau_n + \beta} = \frac{\alpha\tau_e}{\beta} \tag{7.3}$$

which leads to

$$\frac{1}{\tau_e} = \frac{1}{\tau_n} + \frac{1}{\beta} \tag{7.4}$$

In Eq. (7.3) and Eq. (7.4) α and β are capture rates which are unaffected by degradation. In an undegraded diode $\tau_e = \tau_e^0$. After a period of degradation *t*, the density of nonradiative traps, $N_{n,d}$, increases. Thus the electron decay rate is given by [35]:

$$\frac{1}{\tau_e(t)} = \frac{1}{\tau_e^0} + v_{th}\sigma_{nr}N_{n,d}(t) \tag{7.5}$$

where v_{th} is the thermal velocity of electrons and σ_{th} is the capture cross section of the non-radiative traps.

Another factor which contributes to η is the saturation function $f(t_e)$ which accounts for the decay in quantum efficiency due to saturation of the radiative recombination process. The theory of electroluminescence provides the following approximation for this function [31]:

$$f(t_e) = \left\{\ln\left[1 + \frac{n_0}{n_t}\exp\left(\frac{qV}{kT}\right)\right]\right\}\left[\frac{n_0}{n_t}\exp\left(\frac{qV}{kT}\right)\right]^{-1} \tag{7.6}$$

where V is the forward bias voltage applied to the junction, n_0 is the electron concentration in a p-type crystal in absence of a bias voltage, n_t is the excess electron density required for the radiative recombination.

For an abrupt p-n junction I_e is [32]

$$I_e = \frac{qD_e n_0}{L_e}\exp\left(\frac{qV}{kT}\right) \tag{7.7}$$

where D_e is the electron diffusivity and $L_e=(D_e\tau_e)^{1/2}$ is the electron diffusion length. Substituting Eqs. (7.3), (7.6) and (7.7) into Eq. (7.2), we obtain

$$\eta(t) = B[\tau_e(t)]^{1/2}\ln\left[1+\frac{n_0}{n_t}\exp\left(\frac{qV}{kT}\right)\right]\eta_{oc} \tag{7.8}$$

where $$B = \frac{\alpha q(D_e n_t)^{1/2}}{\beta I_t}$$

whereas the electroluminescent efficiency of the undegraded device is given by

$$\eta_0 = B(\tau_e^0)^{1/2}\ln\left[1+\frac{n_0}{n_t}\exp\left(\frac{qV^0}{kT}\right)\right]\eta_{oc} \tag{7.9}$$

assuming that η_{oc} does not degrade and affect the measurement.

Using Eq. (7.8) and Eq. (7.9) and defining $r(t)=\eta(t)/\eta_0$ we get

$$r(t) = \left(\frac{\tau_e}{\tau_e^0}\right)^{\frac{1}{2}}\cdot Q \tag{7.10}$$

where

$$Q = \left\{\ln\left[1+\frac{n_0}{n_t}\exp\left(\frac{qV}{kT}\right)\right]\right\}\left\{\ln\left[1+\frac{n_0}{n_t}\exp\left(\frac{qV^0}{kt}\right)\right]\right\}^{-1} \tag{7.11}$$

We assume that the voltage at the p-n junction is not affected by degradation [33]:

$$V \approx V^0$$

Thus we assume that Q=1.

The relative intensity *r(t)* is then given by:

$$r(t) = \left(\frac{\tau_e}{\tau_e^0} \right)^{\frac{1}{2}} \tag{7.12}$$

A combination of Eq. (7.5) and Eq (7.12) gives an expression for $N_{n,d}(t)$:

$$N_{n,d}(t) = \frac{1}{C} \left(\frac{1}{r^2(t)} - 1 \right) \tag{7.13}$$

where $C = \tau_e^0 v_{th} \sigma_{nr}$.

For simplicity reasons C is assumed to be not affected by degradation. Thus C is absorbed in the amplitude of the diffusion equation which is derived later.

Equation (7.13) provides a relationship between the concentration of non-radiative trapping centres which are generated during degradation and the relative intensity *r(t)*. Since LED degradation is a function of aging time *t*, one must obtain an expression for the increase in $N_{n,d}$ in terms of a reasonable time-dependent process. Diffusion processes are assumed to be responsible for the observed time dependence of degradation. The connection between diffusion and degradation of solid-state devices has been described earlier. In [36] it is suggested that the degradation of GaAs tunneling diodes may be explained by the unimpeded interstitial diffusion of the p-type dopant zinc (Zn) into the junction. Similar investigations have been performed with Cu-contaminated GaP red LEDs [42].

7.2 Identifying magnesium as the p-doping material

In this paragraph we show that the p-type doping material is magnesium. Therefore, depth-resolved time of flight (ToF) SIMS measurements are performed. The experimental set-up is described in appendix C.

To guarantee a planar abrasion, the p-type contact of the LED has been removed by HCL. The surface of the LED chip has been sputtered with cesium ions at an angle of 25° to the surface normal. The Cs^+ ions where accelerated by *V*=3KV, the ion current was *I* = 20nA and

the sputtered surface was A=125x125 µm^2. The secondary ions have been extracted with V=25KV. Figure 7.1 shows the results obtained under these conditions.

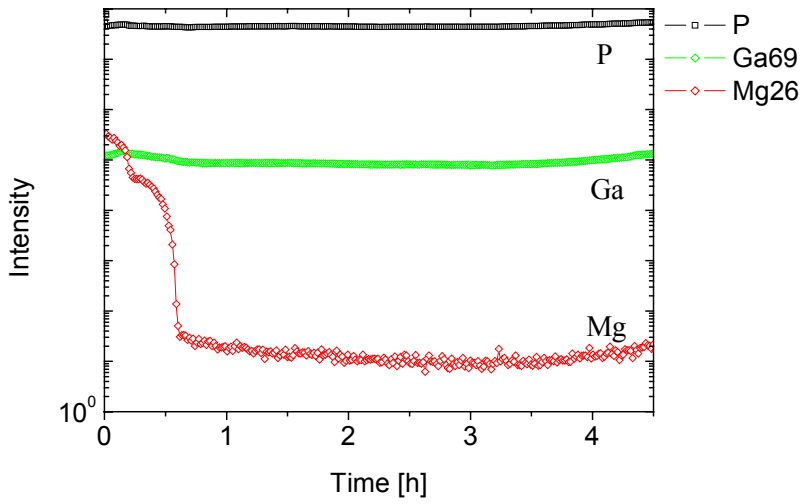

Figure 7.1: Intensity versus sputter time for phosphor, magnesium and gallium.

The intensity versus the sputter time which is equivalent to the sputter depth is plotted for the elements and isotopes P, Ga69, Mg26. For Phosphor a constant count rate during the sputter time is observed. The same characteristic is observed for Ga. Gallium and phosphor are the main substances of the LEDs. Due to the fact that above and under the active layer a GaP window is placed, the constant and high signal in mass spectra is perspicuous. The characteristic of the Mg count rate is quite different. Near the surface the Mg content is quite high. The Mg content decreases in the first 30 minutes of sputtering which is equivalent to a sputter depth of d=5.9µm. Mg is diffused into the first microns of the semiconductor for optimizing the ohmic contact on the p-side. Mg behaves as an acceptor in GaP and a high conductivity is reached. This reduces the serial resistance and a device heat-up is avoided. After a sputter depth of 5.9µm Mg is still observed. This proves that Mg is used as an acceptor in this device. After a sputter time of t=4.5h which is equivalent to a sputter depth of d=53µm the magnesium content starts to increase. At this point the ion beam has reached the boundary of the LED. The ion beam starts to sputter the glue.

The ion beam hits the sample at an angle of α=25° to the surface normal. So the maximum sputter depth is given by:

$$d_{\max} = L_e \cdot \tan\alpha \qquad (7.14)$$

where d_{max} is the maximum of depth, L_e is the edge length of the crater, and α is the angle between the surface normal and the ion beam.

With Eq. (7.14) d_{max} is calculated to 58µm which corresponds to our observed maximum depth of 53µm. During the sputtering process mass-spectra of the magnesium isotopes Mg24, Mg25 and Mg26 have been measured. Figure 7.2 shows the mass-spectra of Mg24, Mg25 and Mg26.

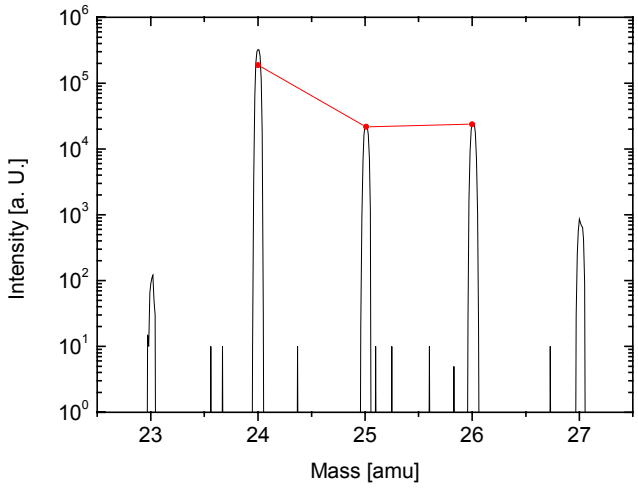

Figure 7.2: Mass-spectra of Mg24, Mg25 and Mg26. Red line describes the intensity ratio of the Mg isotopes in nature.

The red line describes the intensity ratio of the Mg isotopes in nature. For Mg25 we measured exactly the expected intensity, for Mg24 the measured intensity is larger. This can be explained as mass interference with C_2.

The depth resolution strongly depends on the sputtering depth. Near the surface, layers with a thickness of d=5nm can be resolved. Due to the increasing surface roughness with increasing sputter depth the resolution decreases. SEM measurements have shown that the depletion zone of the device is in a depth of d=50µm.

Due to the decreased resolution in a depth of d=50µm it is impossible to detect the magnesium diffusion from the p-type layer into the depletion zone. It has been shown that magnesium is the p-type doping material of the AlInGaP LEDs.

7.3 Magnesium diffusion into the active layer

In [11] Mg atoms diffusing into the active layer are identified as efficient non-radiative recombination centres which reduce the internal quantum efficiency. We will now combine the Mg diffusion into the active layer with the increase of non-radiative trapping centres. The diffused quantity of Mg in the active layer, F_{Mg}, at time t can be expressed as the time integral of the Mg flux [35]:

$$F_{Mg}(t) = \int_0^t -D\left(\frac{\partial C_{Mg}}{\partial z}\right)_{z=w_d} dt' \qquad (7.15)$$

where D is the diffusivity, C_{Mg} is the magnesium concentration, and w_d is the location of the plane where the accumulation occurs. To affect the radiative recombination and decrease the relative intensity, this plane must be in the MQW region.

We assume that the trap density $N_{n,d}$ is proportional to the diffused quantity of Mg atoms F_{Mg}. Thus we take:

$$N_{n,d} = KF_{Mg} \qquad (7.16)$$

where K is a constant of proportionality which also includes the ratio of the junction area to the effective volume of the accumulation.

To evaluate F_{Mg} an analytic expression for $C_{Mg}(z,t')$ is necessary. Before the degradation the Mg content in the p-type layer is C_{Mg}^0 on average. It drops down to zero at and beyond the edge of the active layer. Figure 7.3 shows the concentration gradient in the active layer. The origin of the coordinate system is at the edge of the p-side of the active layer. Then the initial conditions are:

$C_{Mg}(z,0) = C_{Mg}^0$ for z<0

$C_{Mg}(z,0) = 0$ for $0 \le z \le w_d$

The boundary conditions are:

$$C_{Mg}(0,t') = C_{Mg}^{0} \qquad \text{for all } t'$$

$$C_{Mg}(w_d,t') = 0 \qquad \text{for } t' > 0\,.$$

Thus, we assume a Mg concentration of $C_{Mg}(w_d,t') = 0$ at the border of the active layer at the edge of the n-type side [37].

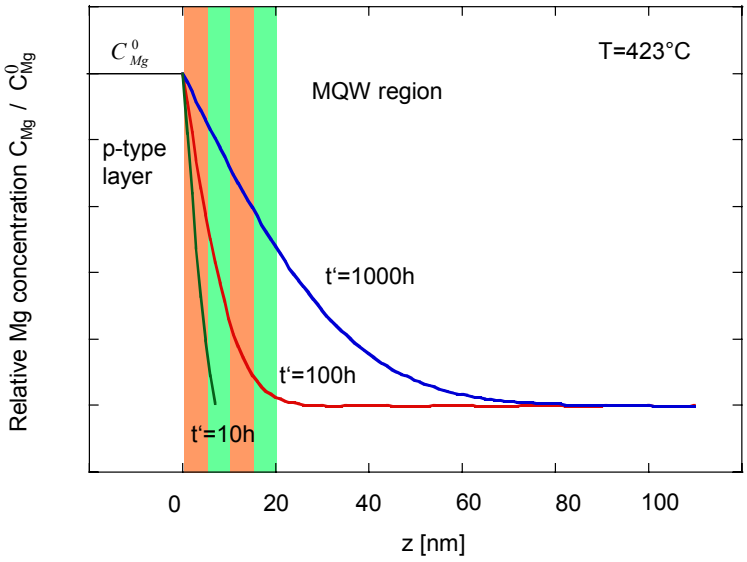

Figure 7.3: Schematic coordinate system for the diffusion of Mg through the active layer during thermal degradation.

The solution of the diffusion equation (Fick's second law) for the initial and boundary conditions can be deduced from Ref. [38, Eq. (4.12)]. The concentration of Mg at z and t is given by the infinite series

$$C_{Mg}(z,t') = C_{Mg}^{0}\left[\frac{(w_d - z)}{w_d} - \frac{2}{\pi}\sum_{m=1}^{\infty}\frac{\sin(m\pi z / w_d)}{m}\cdot\exp\left(-\frac{m^2\pi^2 Dt'}{w_d}\right)\right] \qquad (7.17)$$

The resulting concentration profile is drawn in Fig. 7.3 for the diffusion times t'=10h, t'=100h and t'=1000h. The junction temperature was T=423°C and the diffusivity $D = 1.1\cdot 10^{-13}\,cm^2 s^{-1}$ (see chapter 7.4.1). We assume 10 quantum wells and barriers with a width of w=5nm. Thus the width of the MQW region was assumed to be w_d=100nm. Unretarded diffusion as in Eq. (7.17) can only take place if the device is under a relatively high forward bias voltage. If the device is heated up by a forward current, the retarding effect of the inner E-field is negligible.

Substituting Eq. (7.17) into Eq. (7.15)

$$-D\left(\frac{\partial C_{Mg}}{\partial z}\right)_{z=w_d} = C_{Mg}^0\left[\frac{D}{w_d}+\frac{2D}{w_d}\sum_{m=1}^{\infty}\cos(m\pi)\exp\left(-\frac{m^2\pi^2 Dt'}{w_d}\right)\right]$$

and after integration over time and taking the limits

$$F_{Mg} = C_{Mg}^0 w_d\left\{\frac{t}{4\theta}+\frac{2}{\pi^2}\sum_{m=1}^{\infty}\frac{(-1)^m}{m^2}\left[1-\exp\left(-\frac{m^2\pi^2 t}{4\theta}\right)\right]\right\} \tag{7.18}$$

with the diffusion time:

$$\theta = w_d^2/4D\,. \tag{7.18a}$$

Using Eq.(7.14), Eq. (7.16) and Eq. (7.18) *r(t)* can be expressed as:

$$r(t) = \left[1+\gamma\varphi(t/\theta)\right]^{-1/2} \tag{7.19}$$

where

$$\varphi\left(\frac{t}{\theta}\right) = \frac{t}{4\theta}+\frac{2}{\pi^2}\sum_{m=1}^{\infty}\frac{(-1)^m}{m^2}\left[1-\exp\left(-\frac{m^2\pi^2 t}{4\theta}\right)\right] \tag{7.20}$$

and

$$\gamma = CKC_X^0 w_d = \tau_e^0 v_{th}\sigma_{nr} KC_{Mg}^0 w_d \tag{7.21}$$

γ is expected to be a constant due to the fact that $C = \tau_e^0 v_{th}\sigma_{nr}$ is already assumed as constant. The proportionality factor K is not affected by degradation nor is w_d. The Mg content is assumed to be constant that means not reduced by degradation. Only small variations in C_{Mg}^0 between different samples are expected.

Figure 7.4 depicts the calculated relative intensity *r(t)* versus degradation time. The parameters θ and γ have been chosen to θ= 79.5h and γ= 0.2. After a degradation time of *t=5000h* the intensity is reduced to *r* = 0.5.

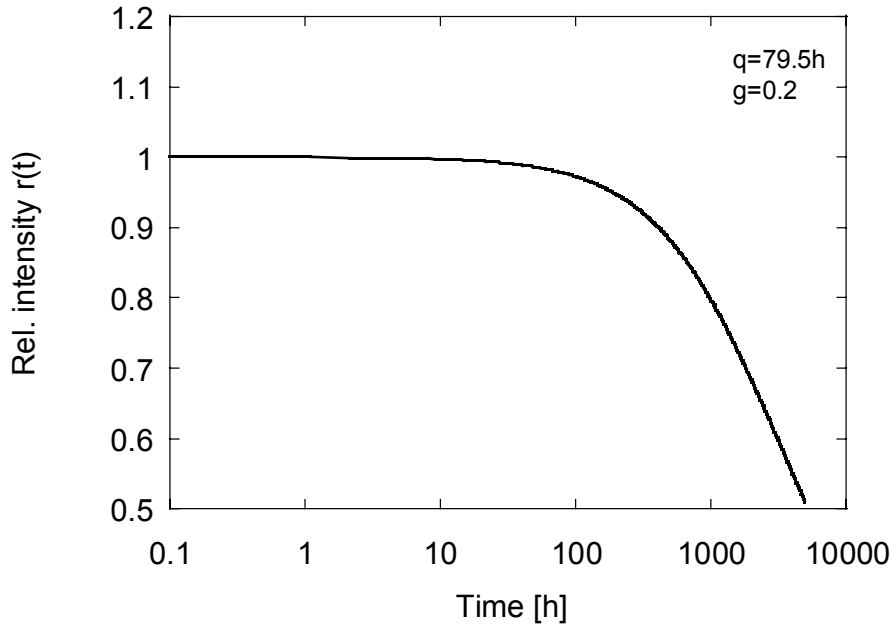

Figure 7.4: The calculated relative intensity r(t) versus degradation time for θ = 79.5h and γ = 0.2.

7.4 Data analysis

Assuming that Mg diffusion is responsible for the degradation, we can extract the diffusivity of Mg by Eq (7.18a). Therefore the experimental data of LED degradation *r(t)* will be fitted by Eq. (7.19). and Eq. (7.20).

The first experiment (sample H G 4) was made under a degradation current of I_{degra}=150mA (T_j=423°C). The luminous flux has been measured at I_{meas}=40mA. Figure 7.5 shows the relative intensity *r(t)* versus the degradation time. The blue dots indicate the experimental data. A fast decrease of intensity is clearly observable. After t=263h the intensity has decreased by 50%. Using Eq. (7.19) and Eq. (7.20) the experimental data have been fitted by a successive approximation of the parameters θ and γ. For practical reasons the infinite series in Eq. (7.20) has been calculated up to m=40. For m>40 no significant change in the result is observable.

The black curve is calculated using the parameters θ=7.5h and γ=0.33. A perfect agreement of experimental and calculated data is obtained. Degradation experiments were also performed

under a forward current of I_{degra}=120mA (T=306°C). The relative intensity has been measured at I_{meas}=40mA and the experimental data are plotted as red dots in Fig. 7.5.

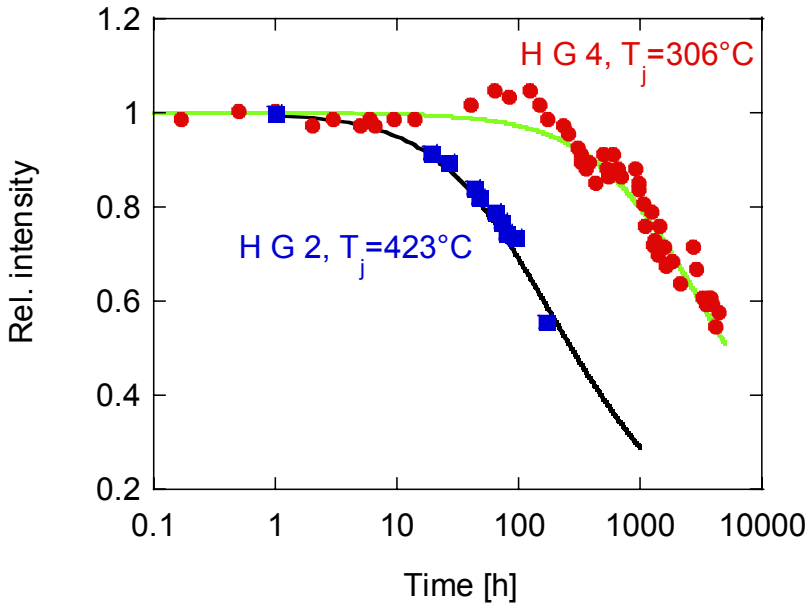

Figure 7.5: Relative intensity versus degradation time. Red dots for I_{degra}=120mA. The green curve is a fit using θ=79.5h and γ=0.2 . Blue dots for I_{degra}=150mA, the black curve is a fit using θ= 7.5h and γ=0.33.

After an aging time of t=360h the intensity decreases to 90% of its starting value and after t=5150h the intensity decreases by 50%. In this case the parameters θ and γ have been set to θ=79.5h and γ=0.2 and the green curve depicts the calculation. The experimental and calculated data are in a perfect agreement with one exception. In the time range between t=25h and t=260h an increase of intensity is observed. This so called "positive aging" is also observed in [39] and has been noticed regularly in our experiments. This increase of intensity cannot be explained by the model presented earlier in this paragraph.

In a further experiment the device has been treated with I_{degra}=40mA (T_j=85°C). The duration of the aging process exceeded t=8000h. Long-term experiments allow to predict an accurate time to failure. This is due to the fact that the stress current is only twice as high as the recommended maximum drive current. Figure 7.6 shows the relative intensity $r(t)$ versus aging time. The red dots indicate the experimental data. During the first 1000 hours the intensity increases approximately by 5%. After t=1350h the intensity has decayed to $r(t)$=1 (100%) and continues to drop to 93% after 8800h of aging time. The curve is calculated using the parameters θ=15000h and γ=0.7. The fit matches the experimentally observed decay at t=1000h, however, for t<1000h an increase of the intensity is observed which is not reproducible by the diffusion model.

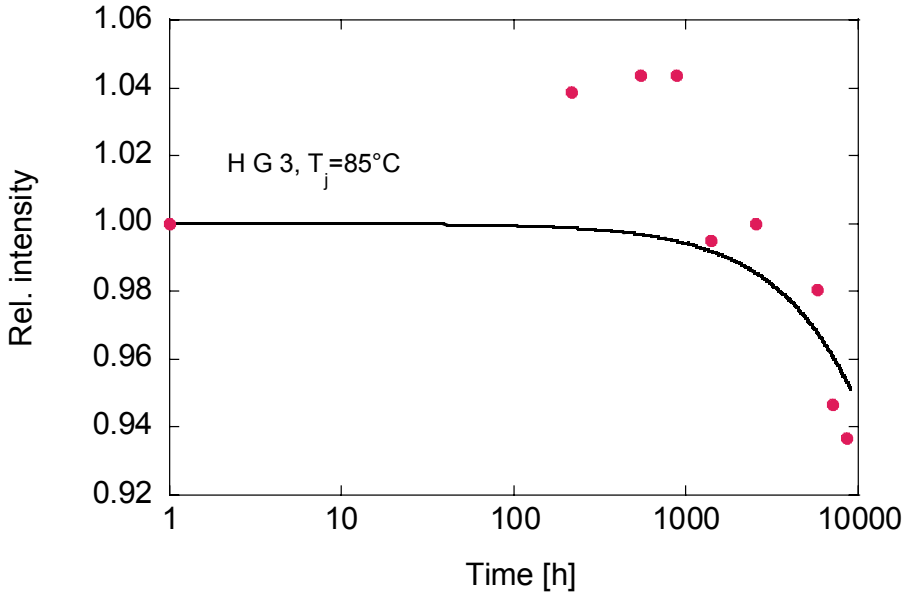

Figure 7.6: Relative intensity versus degradation time at I_{degra}=40mA and I_{meas}=40mA.

The data for the degraded LEDs are listed in Table 1. The following key features are found:

a) θ decreases rapidly with increasing T_j as anticipated and the diffusivity of Mg ($D = w_d^2 / 4\theta$) increases with increasing T_j.

b) The parameter γ is essentially constant, independent of T_j. This is in agreement with the definition of γ in Eq. (7.21). Small changes from diode to diode in the initial Mg doping level $\left(C_{Mg}^0\right)$ and electron lifetime $\left(\tau_e^0\right)$ can affect γ.

Sample	I_{degra}	T_j	θ	γ
H G 3	40mA	85°C	15000h	0.7
H G 2	120mA	306°C	79.5h	0.2
H G 4	150mA	423°C	7.5	0.33

Table 7.1: Values of θ and γ together with degradation data.

7.4.1 The activation and diffusivity of magnesium in AlInGaP

In this paragraph we calculate the diffusion coefficient and the activation energy of Mg in AlInGaP. For the recommended forward current of I=20mA the diffusion time θ will be calculated. As a next step the time to failure for I=20mA will be determined.

The temperature dependence of the diffusion coefficient in solids is usually given by

$$D = D_0 \exp\left(\frac{-\Delta E_a}{kT}\right) \tag{7.23}$$

where ΔE_a is the activation energy and D_0 is the diffusion coefficient at infinite temperatures. This equation is only valid in the case of free diffusion, unaffected by retarding electric fields. Therefore the applicability of Eq. (7.23) to the diffusion values listed in table 7.1 have been tested.

Figure 7.7 shows the Arrhenius plot of $\log(\theta)$ versus $1000/T_j$. Dots are experimental data from diodes degraded at T_j=423°C, T_j=306°C, and T_j=85°C. Clearly, the function relationship is linear, in agreement with Eq. (7.23). A linear fit indicated by the blue line yields $\theta = 0.005 \cdot \exp(5349/T)$.

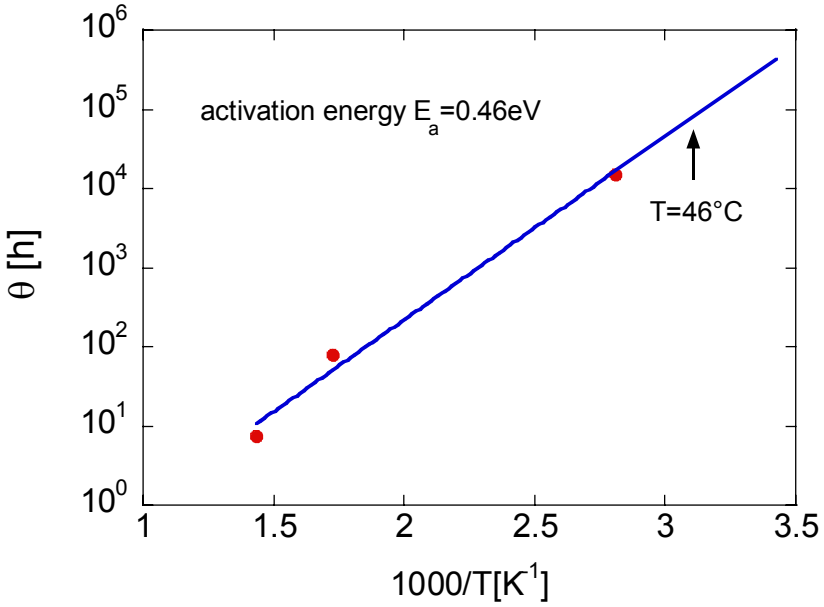

Figure 7.7: Diffusion time $\theta = w_d^2 / 4D$ versus reciprocal junction temperature. The arrow marks T=46°C.

The activation energy is $\Delta E_a = 0.46eV \pm 0.04eV$. In the literature no values for the activation energy of Mg in AlInGaP have been found. But in [35] an activation energy ΔE=0.70eV of an unknown impurity in GaP has been determined. This value is of the same order of magnitude as the activation energy we calculated.

A very well studied material is GaAs. In [40] the activation energy of Mg in GaAs has been found to E_a=1.5eV. This value is three times higher than the value we calculated for the activation of Mg in AlInGaP. One reason for the large difference is the different host crystal.

According to [37] we assume a carrier concentration of $p = 2.14 \cdot 10^{17} cm^{-3}$ of Mg in AlInGaP. Thus the width of the depletion zone has been calculated to W_D=0.11µm. With respect to $\Delta E_a = 0.46eV \pm 0.04eV$ a diffusivity $D_0 = 2 \cdot 10^{-10} cm^2 s^{-1}$ of Mg in AlInGaP at infinite temperatures has been calculated. At a junction temperature T_j=423°C a diffusivity $D = 1.1 \cdot 10^{-13} cm^2 s^{-1}$ has been calculated. The diffusion coefficient for Mg in AlInGaP has not been found in the literature. Therefore we compared our results with the diffusivity of Mg in GaAs. In [40] a diffusivity of $D = 1.2 \cdot 10^{-12} cm^2 s^{-1}$ at T=900°C for Mg in GaAs is determined. A diffusivity of $D = 5.37 \cdot 10^{-15} cm^2 s^{-1}$ at T=785°C for Mg in GaAs is presented in [41].

To obtain a lifetime characteristic at the drive current of I_{degra}=20mA the linear fit was approximated to T_j=46°C. The resulting diffusion time is θ = 90473h. As γ was to be assumed to be a constant, it is set to $\gamma = 0.7$ (table 7.1). With these parameters the relative intensity degradation *r(t)* for a forward current of I_{degra}= 20mA is calculated. Figure 7.8 shows the result.

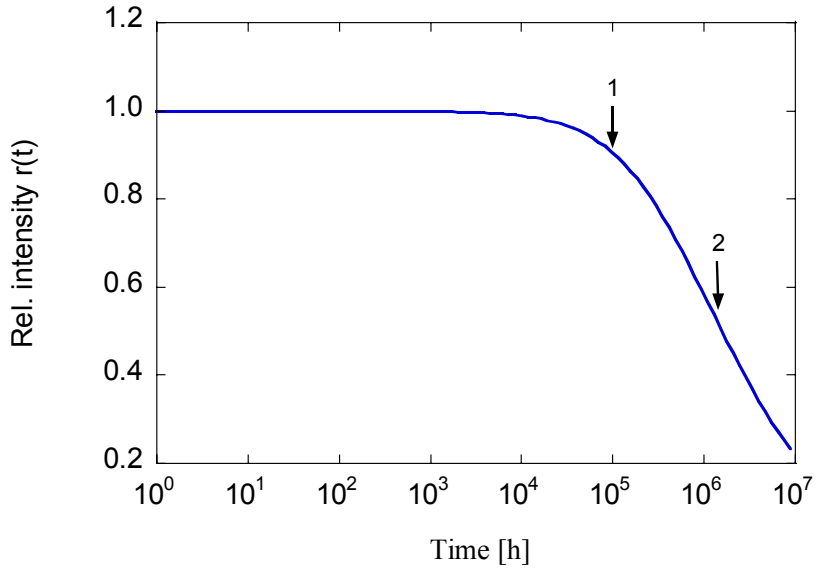

Figure 7.8: Lifetime prediction at a forward current of I_{degra}=20mA. Arrow 1: Time to failure (TTF) at r(t)=0.9 is $10^5 h$. Arrow 2: TTF at r(t)=0.5 is $1.5 \cdot 10^6 h$.

The degradation is clearly weak. For the first 10^4h of degradation time no intensity decrease is expected. After 10^5h of aging time the intensity is reduced to 90% (marked by arrow 1). Therefore, if the time to failure criteria is a loss of 10% of intensity, the diode lifetime will be 10^5h. At *r(t)*=0.5 which is equivalent to a reduction of 50% of luminous intensity the time to failure is $1.5 \cdot 10^6 h$ *(*marked by arrow 2).

In this chapter we have shown that the reduction of intensity can be described by a diffusion of the p-type doping material (Mg) into the MQW region. Using this model we have calculated the reduction of intensity for different junction currents and degradation times. A good match between experimental and theoretical data was achieved.

The activation energy of magnesium in AlInGaP has been determined to $\Delta E_a = 0.46eV \pm 0.04eV$. A diffusivity $D_0 = 2 \cdot 10^{-10} cm^2 s^{-1}$ of magnesium in AlInGaP at infinite temperature was found. The reduction of relative intensity *r(t)* versus degradation time for a drive current of I_{degra}=20mA has been calculated. The lifetime is $1.5 \cdot 10^6 h$ defining a decrease of 50% of relative intensity*(r(t)*=0.5) as failure criteria.

8 Summary

In this thesis we investigate the degradation mechanism of AlInGaP LEDs during encapsulation and operation. A new method to encapsulate AlInGaP LEDs by means of an injection molding tool using polymethylmethacrylat (PMMA) 7N as an encapsulation material is analysed. The combination of semiconductor light source, optics and physical housing in one unit with diminutive dimensions leads to a luminous source with tailored radiation pattern. We demonstrate light beams with a spread angle of 10° obtained by total reflection optics.

Before encapsulation a detailed electrical and optical characterization of the LED chip such as space resolved measurements of the light emission from the edges and top surface are performed. An injection molding tool has been created which allows the encapsulation of four LED chips, each in a parabolic optic with a focal length of f=1.1mm. Encapsulation was done with an Arburg A380 injection molding machine. To investigate the thermal load during the encapsulation process, a new approach for measuring the temperature inside the injection molding tool is presented. It is based on the temperature dependence of the electrical conductivity of a pn-junction. During encapsulation we measure a maximum LED temperature of T=153°C. Due to the low heat capacity of the device, the melt temperature is almost unaffected and a very quick response is achieved. With this method we measure the thermal load of directly encapsulated electrical devices. Furthermore, this method allows to measure the temperature distribution within the molded part using multiple probes. To verify the temperature measurements, a finite element simulation is carried out. The variation of the temperature at the LED chip location is calculated and shows good agreement with the experimental results.

After the encapsulation process the LED properties are investigated and compared with the properties before encapsulation. We find a reduction of the serial resistance as well as an enhanced luminous efficiency. The peak emission wavelength remains constant, but the full width at half maximum (FWHM) of the emission increases by ΔE=9meV. A slight polarisation of the emitted light indicates a polarisation effect of the PMMA.

Accelerated degradation experiments using forward currents of I_1=40mA, I_2=120mA and I_3=150mA for estimating the lifetime of the PMMA encapsulated LEDs are performed.
The measured lifetime under I_2 is t_2=5150h, and under I_3 is t_3=263h using a reduction in the luminous flux of 50% as failure criteria. A diffusion model is presented to explain the decay of luminous flux versus degradation time and degradation current. We support the idea that the reduction of quantum efficiency is caused by diffusion of the p-type dopant into the active layer where it acts as a non-radiative recombination centre. This is supported by other investigations [11]. SIMS measurements show that the p-type doping material is magnesium. Using the diffusion model we determine the lifetime under the recommended drive current of I=20mA. The resulting lifetime is $t = 1.5 \cdot 10^6 h$ using a reduction of 50% in the luminous flux as failure criteria.

Our results reveal that a direct encapsulation of LEDs by means of an injection molding tool is possible. The effects of thermal degradation of the LED are negligible and the LED lifetime is sufficient for most applications. Especially for application in tail lights for passenger cars where a lifetime of t=6000h is required, this method opens a wide new field of space economy and design potential. Ultra thin tail lights which fulfill the legal requirements for passenger cars are possible by this encapsulation technique.

Appendix A: focusing the active layer of a LED chip

In order to obtain the EL from the active region of the LED, the following method is used. First one has to focus on the top (p-contact) surface and then move the focal point 50µm (distance from top surface to the active layer) inside the chip by adjusting the second lens. Figure A.1 depicts the calibration curve for moving the focal point from the surface of the LED chip into the semiconductor material.

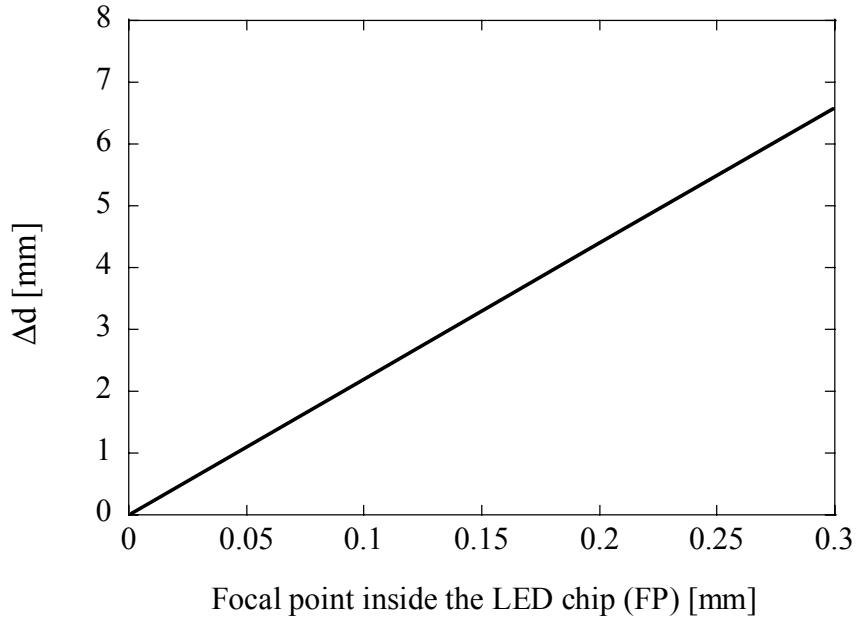

Figure A.1: Calibration curve to focus inside the LED chip. FP is the distance between the surface of the LED chip and the focal point inside the LED, Δd is the distance difference between lens 1 and lens 2.

The x-coordinate of Fig. A.1 describes the distance from the LED chip surface to the point which should be focused by the optics. The y-coordinate is the difference in distance of the two lenses. For example the point of interest is *FP*=0.1mm beyond the chip surface. Thus the distance of lens 1 to lens 2 must be decreased by *Δd*=2.202mm. The relationship is given in Eq. (1).

$$\Delta d[mm] = FP[mm] \cdot 22.02 \qquad (1)$$

Appendix B: capture volume

The intersection plane of the observation cone and the active layer (red) is a hyperbolic bordered area. This border is depicted in Fig. B.1 as blue line.

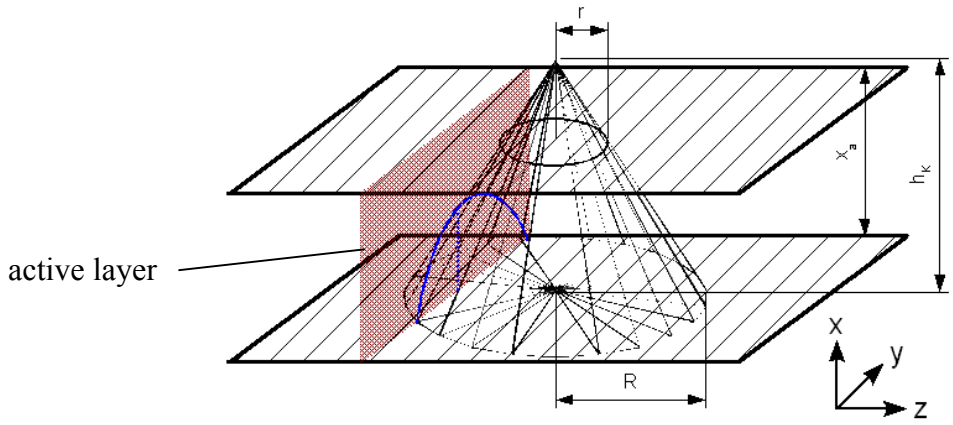

Figure B.1: Observation cone in the LED chip.

The edge planes of the LED chip have the distance x_a, the height of the cone is h_k, the radius of the base area is R. The radius of the top surface area of the cone is r. The spread angle of the cone is given by β. Thus the hyperbola is given by:

$$y = \frac{b}{a}\sqrt{x^2 - a^2} \tag{1}$$

with:

$$a = \frac{h_k}{R}|z| \qquad \text{and} \qquad b = |z| \tag{2}$$

The surface of the hyperbolic bordered area is then given by :

$$A = \frac{b}{a}\int_a^{h_k}\sqrt{x^2 - a^2}\,dx \tag{3}$$

$$= \frac{h_k}{2}\left(\sqrt{R^2 - z^2} + \frac{x^2}{R}\ln\frac{|x|}{R + \sqrt{R^2 - z^2}}\right) \tag{4}$$

Due to the small value of z_a (thickness of the active layer), the volume is given by:

$$V = z_a \cdot A \tag{5}$$

Thus the detection volume is:

$$V = \frac{h_k z_a}{2}\left(\sqrt{R^2 - z^2} + \frac{x^2}{R}\ln\frac{|x|}{R + \sqrt{R^2 - z^2}}\right) \tag{6}$$

with

$h_k = x_a + \dfrac{r}{\tan\alpha}$ and $R = h_k \tan\beta = r + x_a \tan\beta$

Appendix C: SIMS measurement set-up

Depth resolved ToF – SIMS measurements on the AlInGaP LEDs are performed. Goal of these measurements is to identify the p-type doping material and to investigate if a doping material diffusion in the depletion region can be measured with this method. Due to the small dimensions of the samples and the need for a planar surface with an edge length of 5mm the sample is embedded into GaAs. This is illustrated in Fig. C.1. The green rectangles are the GaAs, the red square is the LED. The p-contact of the LED is removed by HCL to get a planar abrasion.

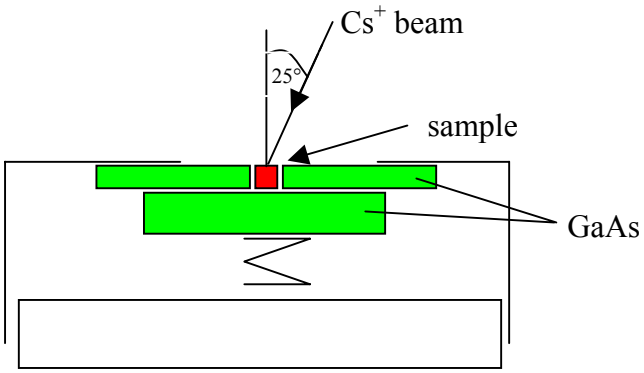

Figure C.1: Sample arrangement in the SIMS unit. Red square marks the LED chip.

The surface is sputtered with Cesium ions under an angle of α=25° to the surface normal. These ions are accelerated by U=3kV, the ion current is I = 20nA and the sputtered surface is A=125x125 μm^2.

Bibliography

[1] DenBaars, S.P. Katona, T. Cantu, P. Hanlon, A. Keller, S. Schmidt, M. Margalith, T. Pattisson, M. Moe, C. Speck, J. Nakamura, GaN based high brightness LEDs and UV, IEEE Electron Devices Meeting, 16.1.1 (2003)

[2] D. A. Steigerwald, J. C. Bhat, D. Collins, R. M. Fletcher, M. O. Holcomb, M. J. Ludowise, P. S. Martin, S. L. Rudaz, IEEE J. Quantum Electron. **8**, 310 (2002)

[3] Hella, Technische Information Licht-Scheinwerfer (2003)

[4] G. Moos, private communication

[5] P. Modak, D. Delbeke, I. Moerman, R. Baets, P. Van Daele, P. Demeester, ICMOVPE-X, workbook of the tenth int. conf. on metalorganic vapour phase epitaxy, June 5-9, Sapporo, Japan, 319 (2000)

[6] M. Zoorob, G. Flinn, LEDs Magazine, August, 21 (2006)

[7] E. F. Schubert, *Light-emitting Diodes 2nd edition*, (Cambridge University Press, Cambridge, 2006)

[8] M. L. Cohen; T. K. Bergstresser, Phys. Rev. **141**, 789 (1966)

[9] I. Vurgaftman, J. R. Meyer, L. R. Ram-Mohan, Appl. Phys. Rev. **89,** 5815 (2001)

[10] J. Singh, *Semiconductor Optoelectronics*, (Mc Graw Hill, New York, 1997)

[11] K. Streubel, N. Linder, R. Wirth, A. Jäger, IEEE J. Quantum Electron. **8**, 321 (2002) and Workshop Erlangen (2005)

[12] N. W. Ashcroft, N. D. Mermin, *Solid state physics* (Thomson Learning Inc., Stamford 1976)

[13] F. Schwabl, *Quantenmechanik*, (Springer-Verlag Berlin Heidelberg New York, 2002)

[14] Lumileds Lighting, U.S. LLC, Technical datasheet DS31, (2004)

[15] Y. Xi, T. Gessmann, J. Xi, J. K. Kim, J. M. Shan, E. F. Schubert, A. J. Fischer, M. H. Crawford, K. H. A. Bogart, A. Allermann, J. J. Appl. Phys. **44**, 7260 (2005)

[16]D. Schwedt, *Räumlich und spektral hochaufgelöste Sepktroskopie der Resonanzfluoreszenz an Exzitonen in ungeordneten Halbleiterfilmen*, (Dissertation, Universität Roststock, 2005)

[17] P. K. Basu, *Theory of optical processes in semiconductors*, (Clarendon Press, Oxford, 1997)

[18] U. Jahn, J. Menniger, R. Hey, B. Jenichen, H. T. Grahn, E. Runge, Mat. Science and Engineering: B, **42**, 133 (1996)

[19] M. A. Herman, D. Bimberg, J. Christen, J. Appl. Phys. **70**, R1 (1991)

[20] S. Adachi, J. Appl. Phys. **66**, 6030 (1989)

[21] A. Zukauskas, M. S. Shur, R. Gaska, *Indroduction to solid-state Lighting,* (Wiley-Interscience Publication, Vilnius, 2001)

[22] Fa. Hartmann & Braun, Gebrauchsanweisung, Beleuchtungsmesser EBLX 3, Frankfurt (1971)

[23] D. Lüerßen, R. Bleher and H. Kalt, Phys. Rev. B **61** 812 (2000)

[24] P. J. Dean, E. G. Schönherr, R. B. Zetterstrom, J. Appl. Phys., **41,** 3475 (1970)

[25] C. F. Zhu, W.-K. Fong, B.-H. Leung, C.-C. Cheng, C. Surya, IEEE Trans. Electron. Devices, **48**, 1225 (2001).

[26] S. Nakamura, G. Fasol, *The blue laserdiode, GaN based light emitters and lasers*, (Springer, Berlin, 1997)

[27] G. Meneghesso, S. Levada, R. Pierobon, F. Ramazzo, E. Zanoni, A. Cavallini, A. Castaldini, G. Scamarcio, S. Du, I. Eliashevich, Proc. of IEEE Int. Electron Device Meeting, 103, San Francisco, California, December 8-11 (2002)

[28] E. F. Schubert, Basics of LED encapsulants, (Troy, New York, 2002)

[29] Kenndaten für die Verarbeitung thermoplastischer Kunststoffe Teil 1, VDMA, (Carl Hanser Verlag München, 1979)

[30] Y. P. Varshni, Physica, **34**, 149 (1967)

[31] M. Lasch, F. Rudolph, L. Schreiner, H. Schulze, J. Appl. Polymer Science, **11,** 369 (2005)

[32] J. M. Ralston, J. Appl. Phys. **44**, 2635 (1973)

[33] W. Rosenzweig, W. H. Hackett, Jr., J. S. Jayson, J. Appl. Phys. **40**, 4477 (1969)

[34] J. S. Jayson, R. N. Bhargava, R. W. Dixon, J. Appl. Phys. **41**, 4972 (1970)

[35] A. S. Jordan, J. M. Ralston, J. Appl. Phys. **47**, 4518 (1976)

[36] R. L. Longini, Solid State Electron **5**, 127 (1962)

[37] P. N. Grillot, S. A. Stockman, J. W. Huang, J. Appl. Phys. **91**, 4891 (2002)

[38] J. Crank, *The Mathematics of Diffusion* (Oxford U. P., London, 1956)

[39] O. Pursiainen, N. Linder, A. Jaeger, R. Oberschmid and K. Streubel, Appl. Phys. Lett., **79**, 2895 (2001)

[40] N. Nordell, P. Ojala, W. H. van Berloa, and G.Landgren, J. Appl. Phys. **67,** 778 (1990)

[41] V. A. Labunov, O. I. Velichko, S. K. Fedoruk, J. Of Eng. Phys. and Thermophys. **67**, 1067 (1994)

[42] A. A. Bergh, IEEE 8th Annual Proceedings on Reliability Physics, Las Vegas, 48 (1970)

List of samples

Note: All samples are Lumileds HWFR-B410 LEDs.

Degradation experiments:

Sample 1: Resin encapsulated LED I_{degra}=70mA, #33_C1

Sample 2: Chip only I_{degra}=120mA, name LZ-EL 1

Sample 3: Chip only I_{degra}=120mA, name LZ-UL 2

Sample 4: PMMA encapsulated LEDs at I_{degra}=120mA soldered chip, H G 1

Sample 5: PMMA encapsulated LEDs at I_{degra}=120mA glued chip, H G 2

Micro EL

G H 1, non-encapsulated LED chip

E04, non-encapsulated LED chip

SIMS Measuremnts

SIMS 2, non-encapsulated LED chip

Diffusion model:

H G 2, degradation current I=120mA

H G 3, degradation current I=40mA

H G 4, degradation current I=150mA

Temperature measurements

Temp 1 – Temp 5, non-encapsulated LED chips

Influence of injection moulding on LED performance

Dit 19, PMMA encapsulated LED

Publication List

S. Preuß, K. Lischka

Injection-Moulding Encapsulation of LEDs Improves Car Tail Lights

Europhotonics Magazine, February/March (2007)

S. Preuß, D. Potthoff, Th. Preuß, K. Lischka

LED encapsulation- a new approach of rear light design

Proceedings of **SPIE** 61980I, Strasbourg (2006)

H. Potente, Th. Preuß, **S. Preuß**

A New Approach for Temperature Measurement inside an Injection Molding Tool,

Antec, Paper 103176 Charlotte NC, (2006)

Acknowledgements

I would like to thank Prof. Dr. K. Lischka who gave me the opportunity to work in his group and for the valuable discussions during this thesis.
For their support and their useful advices I would like to thank apl. Prof. Dr. D. J. As and Dr. D. Schikora.
I would like to thank the referee apl. Prof. Dr. S. Greulich-Weber.
I am indebted to my students M. Rempe, D. Potthoff, M. Paluga and C. Mietze.
I have to express my thanks to my PhD fellows S. Potthast, Ch. Arens, J. Schörmann, M. Panvilova, E. Tschumak and our Postdocs Dr. N. Rousseau, Dr. M. Peron Franco de Godoy and Dr. A. Pawlis.
I am also grateful for the support of I. Zimmermann, S. Igges and B. Volmer.
The L-Lab members have to be mentioned here. Thank you for your encouragement.
I want to thank S. Strauss for the 3 years of LED investigations and the goniometer measurements.
I have to mention O. Stahlsmeyer and Dr. J. Ante, thanks for the rides on the “Flickenteppich” and the explorations deep down.
I would also like to thank the coffee producers of Costa Rica for keeping me alive.
Furthermore, I have to thank Dortje Rieken for her love, endless patience (the desk in the living room!) and encouragement.
Last but not least I would like to thank my parents for their love and financial support.

This work was financially supported by the Hella KGaA Hueck & Co.